

EFFECTS OF DUST SCATTERING HALOS ON  
TIMING PROPERTIES OF GALACTIC BLACK  
HOLE TRANSIENTS

by

OZAN TOYRAN

Submitted to the Graduate School of Engineering and Natural Sciences  
in partial fulfillment of the requirements for the degree of  
Master of Science

Sabanci University

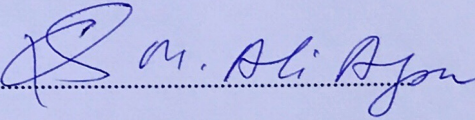
July 2019

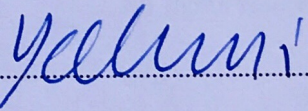
EFFECTS OF DUST SCATTERING HALOS ON TIMING PROPERTIES OF  
GALACTIC BLACK HOLE TRANSIENTS

APPROVED BY:

Prof. Dr. Emrah Kalemci:.....

(Thesis Supervisor)

Prof. Dr. Mehmet Ali Alpar:.....

Prof. Dr. Kazım Yavuz Ekşi:.....

DATE OF APPROVAL: 17/07/2013

© OZAN TOYRAN 2019  
All rights reserved.

# ACKNOWLEDGEMENTS

I would like to start with expressing my gratitude to my advisor Prof. Emrah Kalemci for the guidance and support he has shown to me. His knowledge and discipline inspired me to aim higher and to be a better researcher. I am most thankful to him for putting his faith in me.

I also would like to express my appreciation to Prof. Mehmet Ali Alpar for the education and personal tutoring he provided for his students by setting an example of him. His lectures and sage advice let me find my goal in my physics career and thought me how to follow it.

Another person who had an impact on me is Prof. İnanç Adagideli. His Quantum Mechanics lectures and the discussions he brought up during these lectures broadened my vision and curiosity. For that, I am most thankful to him.

I must express my gratitude to Prof. Tolga Güver, Prof. Ersin Göğüş, Prof. Ünal Ertan and Prof. Kalvir Dhuga as well. Their guidance has been very beneficial for my research and education in astrophysics.

I must also express my appreciation and gratitude to Lynne Valencic, Tomaso Belloni, Diego Altamirano, Mariano Mendez, Dipankar Bhattacharya, Manoneeta Chakraborty, Ranjeev Misra, Keith Arnaud, Carlos Gabriel and Matteo Guainazzi. Their assistance, guidance and friendship they showed to me during the limited time we had, had been priceless.

I acknowledge the support and funding from the Scientific and Technological Research Council of Turkey (TUBITAK, Project Number:115F488)

Finally, I would like to thank my wife Zeynep for her never ending support, my parents Keziban and Fedai for their selfless efforts in my being and education and lastly to my friends who made my time delightful during this journey.

# ABSTRACT

## EFFECTS OF DUST SCATTERING HALOS ON TIMING PROPERTIES OF GALACTIC BLACK HOLE TRANSIENTS

Ozan Toyran

Physics, M.Sc. Thesis, 2019

Supervisor: Prof. Emrah Kalemci

Keywords: Black holes, X-rays, Timing Analysis, Spectral Analysis, ISM

Sources with high column density of absorption have also been known to have high column density of dust along the line of sight. The process of small angle scattering of X-rays by the dust grains in the molecular clouds can produce delays on the order of days. Moreover, the scattering cross-section scales as  $\sim E^{-2}$  where  $E$  is the energy of the X-ray photon, which means the low energy photons are heavily scattered. The differential delays caused by the scattering process may cause loss of coherence and a decrease in the rms amplitude of variability, therefore may impact the studies that use the correlations between the rms amplitude of variability and energy. We observed the Galactic black hole 1E 1740.7–2742 which has very high column density ( $N_H \sim 10^{23}$ ) for  $\sim 20$  ks with *XMM-Newton* and RXTE simultaneously. We also used an archival *Chandra* observation to diagnose if the dust scattering halo (DSH) is present. We characterized the DSH emission in 2.11 – 5.86 keV energy band by spectral means and also by comparing the power spectra from *XMM-Newton* and RXTE. We also investigated the possible location of the  $HCO^+$  cloud relative to the source. Finally, we propose a correction method to obtain the “intrinsic” power spectra and rms amplitude of variability values for *XMM-Newton* and RXTE observations that are behind ample amount of interstellar medium.

# ÖZ

## TOZ SAÇILIM HARELERİNİN GALAKTİK TRANSİT KARA DELİKLERİN ZAMANSAL ÖZELLİKLERİNE ETKİLERİ

Ozan Toyran

Fizik, Yüksek Lisans Tezi, 2019

Danışman: Prof. Emrah Kalemci

Anahtar Kelimeler: Kara Delikler, X Işınları, Zamansal Analiz, Tayfsal  
Analiz

Yüksek miktarda kesit emilim yoğunluğu gösteren kaynakların aynı zamanda görüş hattında yüksek miktarda kesit toz yoğunluğuna sahip olduğu bilinmektedir. X-ışınları moleküler bulutlardaki tozlardan dar açı saçılımı olayıyla günler mertebesinde gecikmeler yaşayabilirler. Dahası, bu saçılım kesit-alanı, E X-ışını fotonunun enerjisi olmak üzere  $\sim E^{-2}$  şeklinde ölçeklediğinden, düşük enerjili fotonların yoğun biçimde saçılması beklenir. Bu saçılım olayı sebebiyle meydana gelen diferansiyel gecikmeler sinyalin eşvreselliğini azaltarak rms değişkenliği genliğinin de azalmasına sebep olabilir. Bu sebeple, rms değişkenliği genliği ve enerji ilintisini kullanan araştırmaların saçılım olayı dolayısıyla etkilenmiş olması beklenebilir. *XMM-Newton* ve RXTE X-ışını uydularını kullanarak Galaktik bir kara delik olan ve çok yüksek kesit hidrojen yoğunluğu gösteren ( $\sim 10^{23} \text{ cm}^{-2}$ ) 1E 1740.7–2742’yi  $\sim 20 \text{ ks}$  süresince eş zamanlı gözlemledik. Bu gözlemlere ek olarak, *Chandra* uydusunun arşivindeki bir gözlemi de kullandık. Toz saçılım haresini *XMM-Newton* ve RXTE verilerinin 2.11 – 5.86keV enerji aralığındaki tayfsal ve zamansal ürünlerini karşılaştırmak suretiyle nitelendirdik ve sonucunda nicelendirmeyi denedik. Bunlara ek olarak kaynağımızın civarındaki bir  $\text{HCO}^+$  bulutunun olası konumunu araştırdık. Son olarak, bol miktarda yıldızlararası toz arkasında kalan kaynakların *XMM-Newton* ve RXTE verilerinin incelenmesinde “esas” güç tayflarının ve rms değişkenlik genliklerinin hesaplanmasına yönelik deneysel bir düzeltme yöntemi öneriyoruz.

# Contents

<b>1</b>	<b>Introduction</b>	<b>1</b>
1.1	Black Hole X-ray Binaries . . . . .	1
1.1.1	Definition and General Properties of a Black Hole . . . . .	1
1.1.2	Finding Black holes . . . . .	3
1.2	Outburst and Transition Mechanisms . . . . .	5
1.3	Observational properties of black hole X-ray binaries . . . . .	6
1.3.1	X-ray Timing-Spectral States . . . . .	6
1.3.2	Multi-wavelength emission properties . . . . .	9
1.3.3	Accretion models and emission mechanisms . . . . .	12
1.4	Dust Scattering Theory . . . . .	22
1.5	1E 1740.7–2742 . . . . .	25
<b>2</b>	<b>X-ray Instruments and Data Analysis</b>	<b>26</b>
2.1	X-ray Instruments . . . . .	26
2.1.1	<i>XMM-Newton</i> Satellite . . . . .	26
2.1.2	The <i>Rossi X-ray Timing Explorer</i> Satellite . . . . .	28
2.1.3	<i>Chandra</i> X-ray Observatory . . . . .	30
2.2	Spectral Analysis and models . . . . .	32
2.2.1	Spectral Analysis . . . . .	32
2.2.2	Spectral models . . . . .	33
2.3	Timing Analysis . . . . .	35
2.3.1	The Discrete Fourier Transformation (DFT) . . . . .	35
2.3.2	The power spectral density (PSD) . . . . .	35
<b>3</b>	<b>X-ray observations of 1E 1740.7–2742 and data analysis</b>	<b>40</b>
3.1	Introduction . . . . .	40
3.2	Observations and data analysis . . . . .	42
3.2.1	<i>XMM-Newton</i> point source analysis . . . . .	42
3.2.2	RXTE point source analysis . . . . .	45
3.2.3	<i>Chandra</i> point source analysis . . . . .	46
3.2.4	Timing Analysis . . . . .	46
<b>4</b>	<b>Results</b>	<b>48</b>
4.1	1E 1740.7–2742 light curves and the source history . . . . .	48
4.2	The Energy spectra . . . . .	51

4.3	Determination of the dead-time level for PSDs . . . . .	53
4.4	Evidence of DSH effects on timing properties? . . . . .	54
4.5	Connection to the molecular clouds . . . . .	57
4.6	The surface brightness profile of <i>XMM-Newton</i> EPIC-PN . . . . .	59
<b>5</b>	<b>Discussions and Conclusion</b>	<b>61</b>
5.1	Quantifying the DSH contribution and improving the background correction . . . . .	61
5.2	Conclusion and Future Work . . . . .	64



# List of Figures

1.1	Top: Compact remnant masses measured in X-ray binaries. Neutron stars and black holes are indicated in black and red colors, respectively. 4U 1700-37 is plotted in dotted-style line because the nature of the compact star is uncertain. The horizontal dotted line divides LXMBs/IMXBs from HMXBs. Bottom: Observed distribution of neutron stars and black hole masses.(Adopted from Casares et al. (2017)) . . . . .	3
1.2	Energy and power spectra of Cyg X-1 in it's hard and soft states(adopted from Gilfanov (2009)) . . . . .	7
1.3	Left: A sketch of general spectral and temporal behavior of GBHTs in the HID and HRD. Right: HRD and HRD of black hole GX 339-4 in the energy range 3.8 – 21.2 keV (adopted from Belloni (2009)). . . . .	8
1.4	VLA radio map at 20 cm wavelength of 1E 1740.7–2742 (0.079 <i>mKy per beam</i> ). Thin and wider contours show the <i>HCO</i> <sup>+</sup> map of the molecular cloud in the Galactic center (adopted from Mirabel et al. (1992)) . . . . .	10
1.5	Radio, soft and hard X-ray lightcurves of the HS,SS and the quiescent states of GX 339-4 (adopted from Fender (1999)) . . . . .	10
1.6	Radio and X-ray (1-10 keV) luminosities of GBHTs (adopted from Corbel et al. (2013)) . . . . .	11
1.7	H-band (top) and <i>RXTE</i> lightcurves. Green open squares show where the data was not simultaneous and are not categorized. Black solid squares correspond to the hard state and red solid triangles correspond to the soft state. Blue data correspond to PCA counts lower than 1.0 <i>count s</i> <sup>-1</sup> (adopted from Buxton et al. (2012)) . . . . .	12
1.8	The figure is a 2D representation of the cross section (The Roche potential contours calculated for two point mass M1 and M2) of $\phi(\mathbf{r})$ . . . . .	13
1.9	The angular momentum contour lines. A vertical cross section of the accretion disk (tilted in the figure) that was observed during the simulation of magneto-rotational instabilities. (adopted from Hawley and Balbus (1991)) . . . . .	16
1.10	The main emission components from an accreting black hole (left) and a schematic of the geometry of the accretion and the corona in the hard state (right).(adopted from Gilfanov (2009)) . . . . .	16
1.11	Compton scattering of a photon from an electron at rest. . . . .	17

1.12	Monte Carlo simulation of spectra of Comptonized seed photons with energy $E \sim 50 \text{ keV}$ from a point source at the center of the sphere (with a Thomson optical depth of $\tau \sim 5$ ). The total spectrum (top) and emerging spectra of scattering orders 1-5 can be seen (adopted from Wilms (1998)) . . . . .	20
1.13	A cartoon diagram of ADAF in different spectral states.(adopted from Chakrabarti (2000)) . . . . .	21
1.14	Reflection spectra obtained by NKK simulation of incident photons for 6 different spectral indices $\Gamma = 1.5, 1.7, \dots, 2.5$ . As the spectra gets harder, higher gas temperatures and ticker optical depths develop. (adopted from Done and Nayakshin (2001)) . . . . .	22
1.15	Geometry of dust scattering mechanism from dust cloud. The source distance is given by D, and the distance to the dust cloud from the observer is given by xD. $\theta$ is the observed scattering angle, $\theta_{sc}$ is the physical scattering angle and CT is the cloud thickness. Dust ring represents the halos seen in modern instruments. . . . .	23
2.1	A schematic of the <i>XMM-Newton</i> spacecraft. . . . .	27
2.2	A schematic of the <i>Rossi X-ray Timing Explorer</i> spacecraft. . . . .	28
2.3	A schematic of RXTE PCA assembly . . . . .	30
2.4	A schematic of Chandra X-ray Observatory . . . . .	31
2.5	A schematic of ACIS arrays with their aimpoints marked with an 'X'. . . . .	31
2.6	Biggest problem during fitting is getting trapped in local minima (Arnaud 2019). . . . .	33
2.7	Several PSDs of XTE J1650–500 during it's outburst decay are fitted with Lorentzians (adopted from Kalemci et al. (2003)). . . . .	39
3.1	(a) The correlation between rms amplitude and the spectral index in 2-6 keV. (b) The correlation between rms amplitude and the spectral index in 6-15 keV. (adopted from Kalemci (2002)) . . . . .	41
3.2	<i>XMM-Newton</i> EPIC-PN image of 1E 1740.7–2742. Green circles are at 5" and 30. . . . .	42
3.3	Lightcurve with 16s resolution. Flare in the middle that comes from background is discarded . . . . .	43
3.4	Modeled Energy Spectrums; <i>Black:</i> PN 0" – 30", <i>Red:</i> PN 5" – 30", <i>Green:</i> PN 7" – 30", <i>Blue:</i> MOS2 . . . . .	44
3.5	Images from the EPIC-MOS1 (left) and EPIC-MOS2 (right) detectors. . . . .	45
3.6	Image of 1E 1740.7–2742 from the Chandra instrument. . . . .	47
4.1	The rebinned light curve from the <i>XMM-Newton</i> 's EPIC-PN instrument . . . . .	49
4.2	The rebinned light curve from the RXTE instrument . . . . .	49
4.3	The rebinned light curve from the Chandra instrument . . . . .	50
4.4	RXTE flux evolution of 1E 1740.7–2742 during 2 months period. . . . .	50
4.5	<i>Chandra</i> flux evolution of 1E 1740.7–2742 during $\sim 2\text{months period}$ . <i>NotethattheModifiedJulia</i>	
4.6	The confidence contours for 0"-30" EPIC-PN spectrum $N_H$ and $\Gamma$ values for 72.58, 74.89 and 79.49 confidence levels. . . . .	52

4.7	EPIC-PN energy spectrum modelled with $\text{tbabs} \times \text{power-law}$ in 2.11 – 5.86 keV energy band. . . . .	52
4.8	<i>Chandra</i> ACIS-I3 energy spectrum modelled with $\text{tbabs} \times \text{power-law}$ in 2 – 10 keV energy band. . . . .	53
4.9	EPIC-PN power spectrum modelled with Lorentzians . . . . .	55
4.10	EPIC-MOS2 power spectrum modelled with Lorentzians. . . . .	56
4.11	RXTE power spectrum modelled with Lorentzians. . . . .	57
4.12	The position of molecular clouds in the Galactic Center and the relative position of 1E 1740.7–2742 (shown as a star in the graph) in the LOS. . . . .	58
4.13	The exposure map of EPIC-PN in the 2.11 – 5.86 keV energy band. . . . .	59
4.14	Unnormalized and normalized radial profiles of EPIC-PN in 2.11-5.86 keV energy band. Blue lines show the 1D PSF. . . . .	60

# List of Tables

3.1	Results for <i>epatplot</i> procedure . . . . .	43
3.2	Data 1: 0'' – 30'', Data 2: 5'' – 30'', Data 3: 7'' – 30'' , Data 4: 1 – 10 keV	43
4.1	Measured PN Poisson levels with different frequency bands . . . . .	54
4.2	Measured MOS2 Poisson levels with different frequency bands. . . . .	54
4.3	EPIC PN power spectra fit results with average count rates in 2.11-5.86 keV energy band . . . . .	55
4.4	EPIC-MOS2 power spectra and average count rates in 2.11-5.86 keV energy range. . . . .	55
4.5	Photon Counts between 0'' – 30'' arcseconds. . . . .	59

# List of Abbreviations

ADAF Advection Dominated Accretion Flow

AGN Active Galactic Nuclei

ARF Auxiliary Matrix Function

BH Black Hole

BHXB Black Hole X-ray Binary

DSH Dust Scattering Halo

EHT Event Horizon Telescope

EOS Equation of State

FRED Fast Rise Exponential Decay

GBHT Galactic Black Hole Transient

HID Hardness Intensity Diagram

HIMS Hard-Intermediate State

HMXB High Mass X-ray Binary

HRD Hardness RMS Diagram

HS Hard State

IMXB Intermediate Mass X-ray Binary

IR Infrared

ISM Interstellar Medium

LMXB Low Mass X-ray Binary

MJD Modified Julian Date

NIR Near Infrared

NS Neutron Star  
NSXB Neutron Star X-ray Binary  
OIR Optical/Infrared  
PSD Power Spectrum Density  
QPO Quasi-Periodic Oscillation  
RMF Response Matrix Function  
RXTE Rossi X-ray Timing Explorer  
SED Spectral Energy Distribution  
SIMS Soft-Intermediate State  
SS Soft State  
WD White Dwarf  
XRB X-ray Binary

# Chapter 1

## Introduction

### 1.1 Black Hole X-ray Binaries

Black holes (BHs) are one of the most mysterious and compelling types of objects in the Cosmos. Even though we were not able to observe them directly, in mid 2019 the Event Horizon Telescope team managed to resolve the photosphere of some Super-massive black holes. While this creates a new window for black hole studies, researchers mostly investigate the influence of BHs on the matter and the space-time in their vicinity. BH masses can range from a few to billion solar masses ( $M_{\odot}$ ). Since such high amounts of mass can squeeze into such a small volume, BHs provides the best sites to test the General Relativity (GR) theory. In this section, I will summarize the definition and general properties of BHs and review the physical processes that affect the X-ray spectral and temporal properties.

#### 1.1.1 Definition and General Properties of a Black Hole

It is useful to define the Compact Objects before defining BHs. Compact objects -Black Holes, Neutron Stars (NS) and White Dwarfs (WD)- are born when their progenitor stars consume all their nuclear fuel and collapse. Nuclear fusion in core of the star produces the thermal radiation (pressure) which resists against the gravitational collapse. When the nuclear fuel is depleted gravitational forces tip the balance in favor of a collapse under it's gravity. WDs and NSs are two special cases where total collapse can be prevented by different equation of state (Eos) configurations. White dwarfs have degenerate electron pressure and neutron stars have degenerate neutron pressure to counter the collapse. Contrarily, the black holes are collapsed into singularities.

Even though BHs are peculiar objects, they can be described by three simple parameters: Mass, spin and charge. Modern concept of a black hole comes from Karl Schwarzschild's

solutions (1916) to the Einstein's theory of general relativity for a non-rotating, neutral object. A non-rotating black hole is also called a "Schwarzschild hole" and a rotating black hole is called a "Kerr hole" by the generalization of Schwarzschild's solutions. According to GR, a massive body's gravity curves the fabric of space-time of it's vicinity and that curvature is called a "geodesic". When the body is sufficiently massive and dense enough, geodesics close in on themselves to a "singularity". Schwarzschild showed that the radius (aka. Event Horizon) of BHs is where the escape velocity is equal to the speed of light;

$$\frac{1}{2}mc^2 = G\frac{Mm}{R_s} \quad (1.1)$$

Then the Schwarzschild radius ( $R_s$ ) is found as,

$$R_s = \frac{2GM}{c^2} \quad (1.2)$$

This region informs us that no information about the processes taking place inside that radius can be transmitted outside. However, in 1975 Stephan Hawking breached this understanding. He found that BHs should emit particles like a black-body temperature (Hawking Radiation). Since the level of this radiation is so insignificant compared to the dominant radiation energies around BHs, the Hawking radiation has not been confirmed by observations yet.

The mass of the progenitor star determines the type of compact object. If the mass of the progenitor is less than  $4 M_\odot$  then resulting object is a white dwarf (Chandrasekhar mass  $\sim 1.4 M_\odot$ ). However, it is not easy to put a limit on mass to determine whether the end result would be a NS or a BH. This is mainly due to the ambiguity of what happens at the final stages of the collapse after the supernova. Maximum mass of a NS is also speculated by many scientists and thought to be between  $1.5-3 M_\odot$ . The environment and the processes that follow the formation of the compact object is also very crucial. Matter accretion onto NS can help exceeding the critical mass and kick-start another gravitational collapse that leads to a black hole.

Maximum mass of a black hole changes with every new discovery. But it is useful to classify black holes according to their masses since the definitions above may vary depending on the type of black hole. There are; stellar mass BHs with masses  $3-10 M_\odot$ , Intermediate mass BHs with masses  $10^2 - 10^3 M_\odot$ , and super-massive BHs with masses  $10^6 - 10^{10} M_\odot$ . Super-massive BHs are believed to be located at the center of nearly every galaxy. Those that are active in the X-rays are called an active galactic nuclei (AGN). Most of the BHs are found in binaries. If the "companion" star is a high mass star (O- or B-star) then the binary is named as high mass X-ray binary (HMXB). Likewise, if the companion star is a low mass



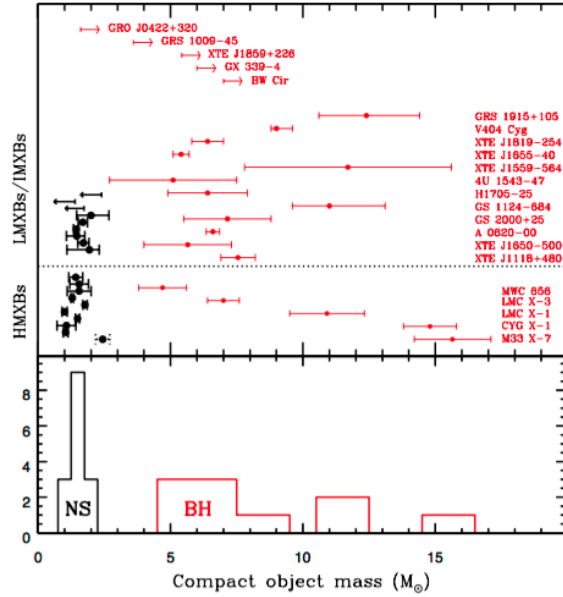


Figure 1.1 Top: Compact remnant masses measured in X-ray binaries. Neutron stars and black holes are indicated in black and red colors, respectively. 4U 1700-37 is plotted in dotted-style line because the nature of the compact star is uncertain. The horizontal dotted line divides LXMBs/IMXBs from HMXBs. Bottom: Observed distribution of neutron stars and black hole masses.(Adopted from Casares et al. (2017))

star then the binary is named as low mass X-ray binary (LMXB). Type of the companion star heavily affects the physical processes in the vicinity of a BH. The effects of companion stars on physical processes will be discussed in detail in section 1.3.3.

## 1.1.2 Finding Black holes

Until recently, the black holes were impossible to detect via direct imaging since they do not emit photons, except Hawking radiation, and are so small to be resolved with modern radio telescopes. With the introduction of the Event Horizon Telescope (EHT), it is now possible to even directly image the black holes. As mentioned earlier, their influence in their vicinity provides us the necessary means to find these objects. Matter, from the companion star, accreting onto a BH slowly loses some of its potential energy in the form of radiation (dominantly in X-rays). We can detect this radiation with our X-ray satellites if the mass accretion rate is high enough. Such systems are called X-ray binaries (XRBs) and evidently, best place to look for a BH is XRBs. However, this does not mean that the compact object is a BH necessarily. There are many obstacles for such a claim. One has to show that the object is smaller than its Schwarzschild radius. However, this is nearly impossible due to small sizes and large distances.

Calculating the mass of the compact object is the best indirect method so far. Assuming no exotic particles exist in a NS that would prevent the collapse, most physicists agree that  $3M_{\odot}$  is a safe upper limit for the maximum mass of a NS. If the mass of the compact object is greater than  $3M_{\odot}$ , it can be claimed as a BH.

To calculate the mass of a compact object one needs to use a dynamical method. XRBs with a bright companion sometimes show absorption line in the optical spectrum of the companion star. These lines are Doppler shifted due to the Keplerian motion of the companion star around the compact object. One can find the radial velocity of the companion star from the Doppler shift. Finally, using the calculated radial velocity and the orbital period of the system, the mass function of the binary can be found:

$$f(M_1, M_2, i) \equiv \frac{(M_2 \sin i)^3}{(M_1 + M_2)^2} = \frac{P_{orb} v_1^3}{2\pi G} \quad (1.3)$$

where  $i$  is the inclination angle of the binary with respect to observer's line of sight,  $v_1$  is the radial velocity of the companion star,  $M_2$  is the mass of the compact object and  $M_1$  is the mass of the companion star. It can be seen that the mass function does not yield the mass of the compact object rather allows for a lower limit for  $M_2$  by setting  $M_1 = 0$  and  $i=90^\circ$ . If this limit is greater than  $3M_{\odot}$ , we can safely claim the existence of a BH in the binary system. In Figure 1.1 a distribution of XRBs masses can be seen.

What if the companion star is not bright enough for a dynamical measurement? Then one has to compare the similarity of their observational properties to the properties of known black hole X-ray binaries such as;

- Characteristic X-ray spectrum (a hard or cut-off power-law and a soft blackbody component from the disk)
- Quasi-periodic oscillations in 0.1-450 Hz range
- Radio and near-infrared (NIR) properties (e.g. radio/X-ray luminosity correlation )
- Variability properties of different states

Moreover, one can also make use of the spectral and temporal differences of NSs and BHs. BHXBs are usually under-luminous in X-rays with respect to NSXBs (McClintock et al. 2004). Periodic pulsations and Type-I thermonuclear bursts are only observed in NSs since they have a hard surface unlike BHs. However, some NS may not show such characteristics. Then, lack of hard surface can help us again through the differences in variability of the signal. While power spectrum density (PSD) drops beyond frequencies  $>10$  Hz for BHs, NSs show aperiodic variability  $>100$  Hz (Sunyaev and Revnivtsev 2000). Sunyaev and Revnivtsev

claimed that the difference in power spectra (PSDs) arise from different dominant emission regions of BHs and NSs.

## 1.2 Outburst and Transition Mechanisms

Due to the nature of LMXBs, we observe sharp increases in luminosity by many orders of magnitude. This behavior is due to variable conditions in LMXBs. A dramatic increase of mass accretion onto the compact object via Roche lobe overflow triggers an outburst. Before going into physical and spectral details, it is useful to refer to "outburst" definition employed by Tanaka and Shibazaki (1996):

- The X-ray flux increases by more than two orders of magnitude within several days.

A more appropriate criterion would be an increase of X-ray intensity from below  $10^{33} \text{ erg s}^{-1}$  to well above  $10^{37} \text{ erg s}^{-1}$  in the range 1-10 keV, whenever a distance estimate is available.

- The flux declines on timescales of several tens of days to more than one hundred days, and it eventually returns to the pre-outburst level.

The light curves are various: Some show a rather monotonic decline, but in many cases the light curves are more complex than that. In some cases, the sources are "turned on" and remain persistently visible for a year or longer after an outburst.

- In recurrent transients, the duration of an outburst is shorter than the quiescent period. The duty ratio over a long time span is less than unity.
- There is no fixed periodicity of recurrence.

The increase of the X-ray illumination also brightens the disk in optical (radio outbursts) that has a characteristic spectrum as well. As it was mentioned above, the light curve of the outburst is usually different from source to source, but some may show similarities.

The mass accretion rate is a crucial parameter to determine whether a source is a transient or a persistent source. Tanaka and Shibazaki (1996) observed that it is not possible to maintain a stable mass accretion onto the compact object below  $\dot{M} \sim 10^{16} \text{ g s}^{-1}$ . It is thought that the mass accretion into the disk still continues even in the quiescent period. The accumulated matter during the quiescence state might be powering the next outburst. There are two competing models describing the outbursts: 1) The disk instability models (Lin and Taam 1984; Cannizzo et al. 1985; Mineshige and Wheeler 1989), 2) The mass transfer instability models (Osaki 1985; Hameury et al. 1990).

According to the first model; during the quiescence, the disk is cool and neutral. As matter accumulates, both the surface density and the temperature increases. When the surface density reaches a critical point, a thermal instability kicks in. This instability arises from a very steep temperature dependence of the opacity in a partially ionized accretion disk. The disk jumps to a hot state with much higher viscosity causing rapid in-fall of the matter onto the compact object, creating an X-ray outburst (Tanaka and Shibazaki 1996). When the density is low again the disk returns to the cool state. This mechanism can explain the fast rise, the exponential decay and the recurrence times of the X-ray outbursts.

The second model has a different approach on where and how the thermal instability occurs. They claim that the sub-photospheric layers of a companion star are heated by relatively hard ( $> 7 \text{ keV}$ ) X-rays from the compact object. The heated, therefore expanded layers bring the atmosphere to an unstable regime and leads to a sudden mass transfer. When the L1 region (Fig. 1.8) is "shielded" by the accretion disk, the swelling of the companion star stops, ending the mass transfer. The outburst ends when all the mass in the accretion disk is transferred onto the compact object. Even though this model can explain the FRED and recurrence times, it can not physically describe how the trigger happens. To trigger an outburst, the hard X-ray flux at L1 must exceed the intrinsic stellar flux. During the quiescence, the X-ray luminosity is too low to induce and instability.

## 1.3 Observational properties of black hole X-ray binaries

### 1.3.1 X-ray Timing-Spectral States

Decades of X-ray observations revealed that the GBHTs are found in several distinct spectral states (Tanaka and Lewin 1995; van der Klis 1995). These spectral states are defined in terms of relative strength of two sources of the X-ray emission: A soft black-body radiation, originating from an optically thick accretion disk (Shakura and Sunyaev 1973) and a hard, power-law like emission possibly originating as Compton Scattering emission from an optically thin, hot accretion corona or ADAF. "Soft state" (SS) is the state in which the soft disk component dominates the spectrum. Likewise, during the "Hard state" (HS) the hard power-law component dominates the observed spectrum. Energy and power spectra of the main states can be seen in Figure 1.2. Hard component is modelled by Comptonization of cold seed photons ( $kT \sim 1 \text{ keV}$ ), which are thought to be radiated from the accretion disk (Gilfanov 2009), in a hot corona ( $kT \sim 100 \text{ keV}$ ).

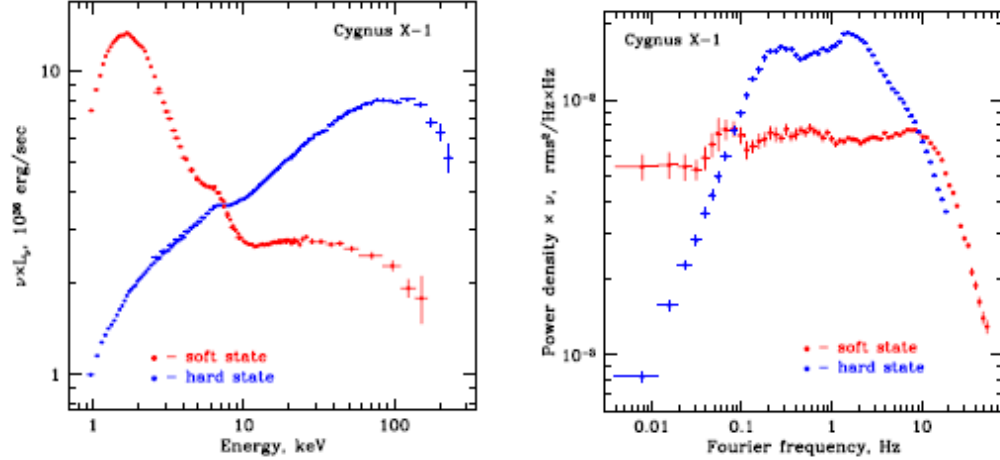


Figure 1.2 Energy and power spectra of Cyg X-1 in it's hard and soft states(adopted from Gilfanov (2009))

It is important to point out that the main states apply to both persistent and transient sources. For GBHTs, state transitions are deeply rooted into the evolution of the outbursts. During the rise and decay phase of the outburst hard component is the dominant emission while the soft component dominates the period in between. Belloni (2009) identified two more states in addition to the main states. They are the hard-intermediate state (HIMS) and the soft-intermediate state (SIMS) with their distinguishing timing properties. These states show properties of both of the main states however cannot be modelled with solely one of the main states. The distinguishing property of these intermediate states is that they exhibit different types of quasi-periodic oscillations in their power spectrum densities (PSD).

There are two fundamental tools used to characterize the behavior of the black hole transients; the hardness-intensity diagram (HID), where the total counts plotted as a function of hardness, and the hardness-rms diagram (HRD). Hardness is calculated as the ratio of total counts in the hard (6.3 – 10.5 keV) and soft (3.8 – 6.3 keV) energy bands. The four states and evolution of them can be seen in Figure 1.3. The GBHTs are usually at quiescence state before an outburst. During the rise period, spectra hardens with increasing flux. When the outburst achieve it's peak, it's spectra starts to soften. The source moves to left on the top branch in the HID, passes the HIMS and SIMS then reaches the soft state. After a while, flux decreases significantly and the source transits back to the hard state and eventually goes back to the quiescence state. Time scale of this cycle changes from months to years depending on the source and the outburst. But that might not always be the behavior. Sometimes sources return back to the quiescence without reaching the soft state. These outbursts are called "failed outbursts" (Capitanio et al. 2010; Del Santo et al. 2016)

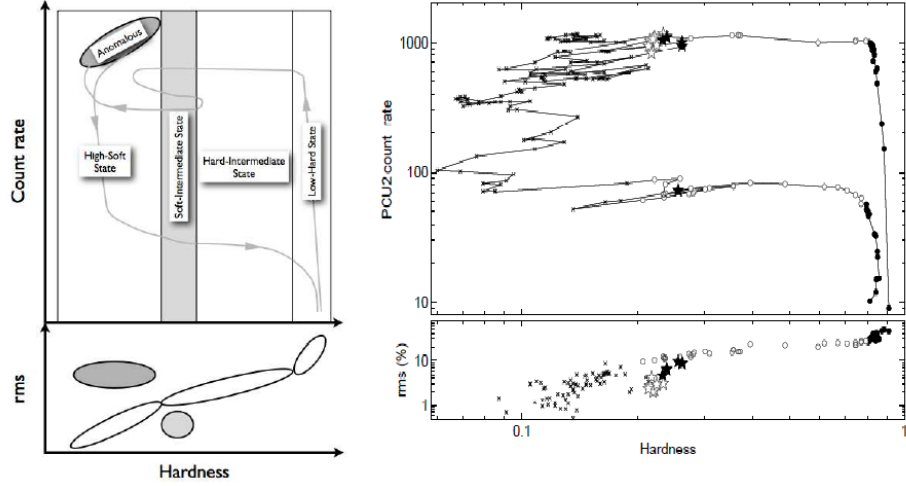


Figure 1.3 Left: A sketch of general spectral and temporal behavior of GBHTs in the HID and HRD. Right: HRD and HRD of black hole GX 339-4 in the energy range 3.8 – 21.2 keV (adopted from Belloni (2009)).

The observational framework of the state characteristics and transition properties are summarized below:

**Hard State:** This state describes the rise and decay part of an outburst and can be seen as the vertical branch in the HID. It’s energy spectrum is characterized by a power-law with a power-law index of 1.5 – 1.8 in the 3 – 25 keV energy band. Very high level of variability with typical values of  $\sim 30 - 40\%$  is associated with the hard state. It can be seen from the Fig. 1.3 that rms variability is anti-correlated with flux and positively correlated with the hardness. The hard state PSD can be modelled with a number of Lorentzian components (Pottschmidt et al. 2003; Belloni et al. 2002), one of which can take the form of a type-C QPO. Duration of this state can be quite variable.

**HS to HIMS:** To distinguish the transition from the HID or HRD is very difficult. Most obvious hint for the transition has been observed in the IR/X-ray correlation of GX 339-4 (Homan et al. 2005).

**HIMS:** Source moves along the top horizontal brunch in the HID while it’s energy spectrum softens with a steeper power-law that has a photon index up to  $\sim 2.5$ . Energy spectrum also shows a thermal disk component. It’s PSD exhibits band-limited noise and a strong type-C QPO. The fractional rms is halved ( $\sim 10 - 20$ ) compared to the HS. As the spectra softens, rms variability continues to decrease. The hard-intermediate state PSD can again be decomposed in Lorentzian components but the peak frequencies are higher than that of the hard state.

**HIMS to SIMS:** This transition can only be identified via temporal means. The noise and the rms continues to decrease as softening continues. A type-B QPO appears in the PSD.

**SIMS:** Energy spectrum is slightly softer than HIMS but the main difference is in the timing characteristics. The level of variability is as low as a few %. It's PSD is often has either a type-A or type-B QPO.

**From and to SIMS:** After the SIMS, the source can either return to HIMS or go to the soft state. But the behavior can be much more complex. Either way, it's PSD contains a type-B QPO.

**Soft State:** This state has the softest spectrum that is dominated by a thermal disk component with a very low contribution from the hard power-law component. The level of rms variability is in the form of a steep component ( $\sim 1\%$ ) or even absent. Sometimes weak QPOs can be observed in the 10-30 Hz range.

**Soft to Hard State:** This transition is associated with the lower horizontal branch in the HID. The timing properties change smoothly compared to the top branch due to low levels of flux. For a detailed description of decay phase of the outburst (Kalemci et al. 2005a).

**Quiescent State:** It can be seen from the HID that quiescent state seems like a mode of the HS with lower luminosities. It's spectrum can usually be fitted with a power-law. However, some observations can be softer than typical hard state values (Plotkin et al. 2013).

## 1.3.2 Multi-wavelength emission properties

### 1.3.2.1 Radio emission and the Radio/X-ray correlation

The GBHTs generally exhibit discrete radio ejections during the outburst. Radio emission is thought to originate from the scynchrotron emission in the jets. Ejected radio blobs and their evolution have been observed directly with radio telescopes. An image of VLA radio map can be seen in Fig. 1.4.

During the quiescence state, GBHTs are very radio quiet (Corbel et al. 2000). In the hard state, radio emission is weak but steady with a flat/inverted radio spectrum. Observations during the HS confirm the relation with jet ejections (Mirabel et al. 1992; Stirling et al. 1997; Russell et al. 2010). Radio flux in the soft state drops even more by a factor of  $> 25$  (Fender 1999). Low levels of radio emission at SS is attributed to the synchrotron emission as well. Figure 1.5 shows the strong correlation of radio and X-ray emission. It is not very clear if the jet is suppressed/cooled via the inverse Comptonization of the seed photons coming from the disk. Nevertheless, the radio emission is thought to be the tail emission from the flare event at the ignition of the outburst.

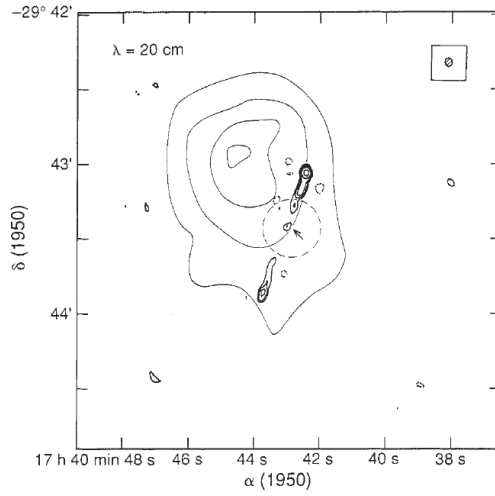


Figure 1.4 VLA radio map at 20 cm wavelength of 1E 1740.7–2742 ( $0.079 \text{ mKJy per beam}$ ). Thin and wider contours show the  $\text{HCO}^+$  map of the molecular cloud in the Galactic center (adopted from Mirabel et al. (1992))

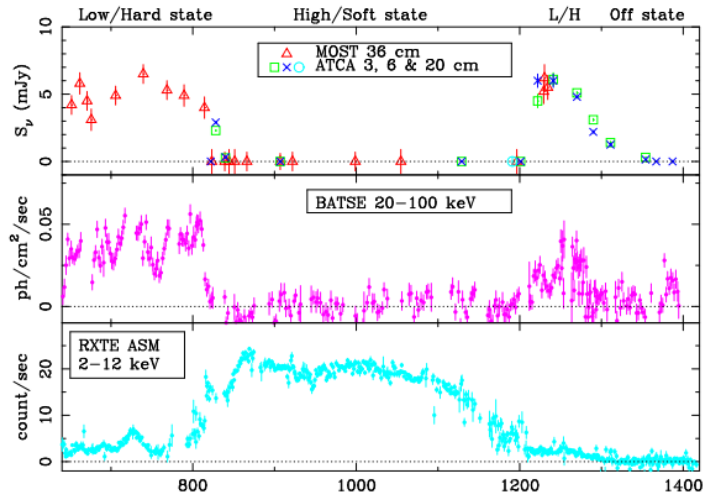


Figure 1.5 Radio, soft and hard X-ray lightcurves of the HS,SS and the quiescent states of GX 339-4 (adopted from Fender (1999))

).



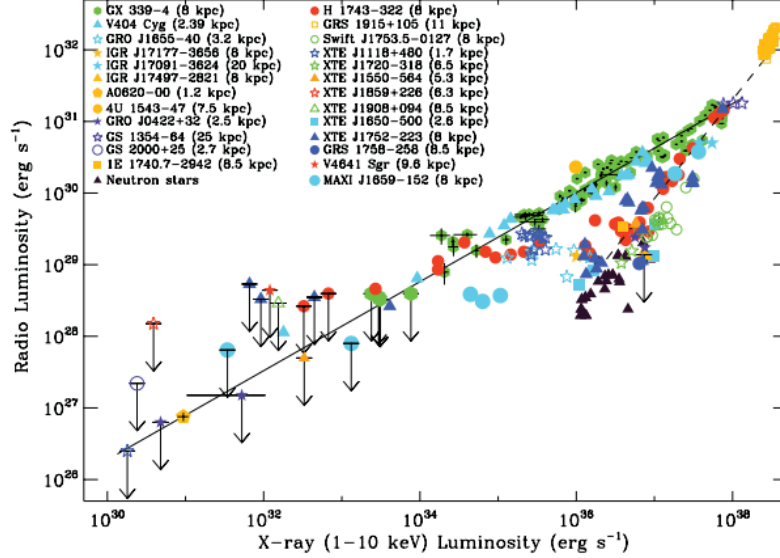


Figure 1.6 Radio and X-ray (1-10 keV) luminosities of GBHTs (adopted from Corbel et al. (2013))

**Radio/X-ray intensity correlation:** The relation between the radio and X-ray intensity correlation is in the form of a non-linear power-law,  $L_{Rad} \propto L_X^b$ , where the correlation index  $b \approx 0.7 \pm 0.1$ ,  $L_{Rad}$  is the radio luminosity and  $L_X$  is the X-ray luminosity. This has become a "canonical" correlation applied to both GBHTs and AGNs (Corbel et al. 2000, 2003, 2004; Gallo et al. 2003; Merloni 2002). However, further researches on GBHTs showed that there is another correlation track (Outliers) with a  $b \sim 0.6$  (Corbel et al. 2003, 2004; Rodriguez et al. 2007; Gallo et al. 2012). These two correlation tracks can be seen in Figure 1.6. And more recent observations showed transitions from the outliers track back to the standard track below a critical X-ray luminosity ( $L_X \sim 10^{36} \text{ erg.s}^{-1}$ ) (Coriat et al. 2009, 2010; Ratti et al. 2012). In summary; while it is evident that the radio/X-ray correlation harbors information about the disk-jet coupling in GBHTs, current understanding of accretion flows stand challenged in the picture we see with the different tracks.

### 1.3.2.2 Optical and Infrared Radiation (OIR)

The optical and infrared radiation from GBHTs come from many different components, therefore allows us to calculate various essential parameters that are used in dynamical mass measurements, identification of companion star etc. Optical and IR emission from GBHTs is radiated from the outer part wings of the disk, the jet and from the companion star.

The OIR emission during the soft state is dominated by a thermal blackbody component, indicating an accretion disk origin. When the source transits from the HS to SS, the optical

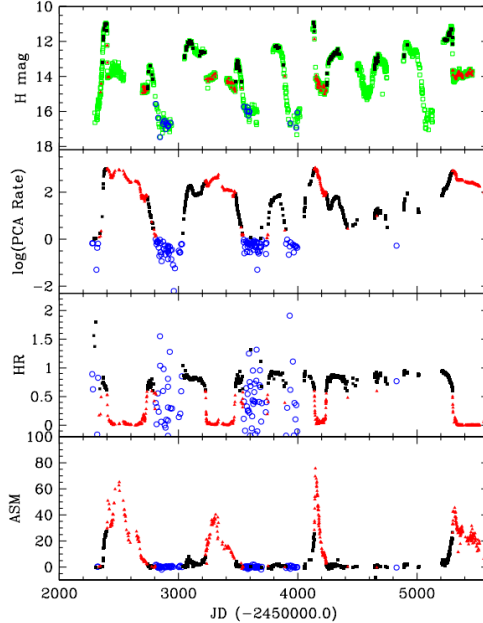


Figure 1.7 H-band (top) and *RXTE* lightcurves. Green open squares show where the data was not simultaneous and are not categorized. Black solid squares correspond to the hard state and red solid triangles correspond to the soft state. Blue data correspond to PCA counts lower than  $1.0 \text{ count s}^{-1}$  (adopted from Buxton et al. (2012)).

and infrared emission intensity drops significantly (Homan et al. 2005; Buxton et al. 2012). OIR brightens again when the source goes back to the HS (Kalemci et al. 2005b). NIR spectrum is now very different from the optical spectrum and usually follows the radio spectrum (Homan et al. 2005; Russell et al. 2006; Coriat et al. 2009). The OIR SEDs with a negative slope of  $\sim -0.6$  and NIR/Radio correlation suggest a non-thermal component originating from the jet ejections (Fender 2001; Fender et al. 2004, 2005; Kalemci et al. 2005b; Russell et al. 2010; Dinger et al. 2012). The hard state SEDs are shown to be fitted with a doubly broken power-law that breaks in the IR and occurs when the X-ray flux changes (Nowak 2005). The OIR/X-ray relation of GX 339-4 can be seen in the Figure 1.6.

### 1.3.3 Accretion models and emission mechanisms

#### 1.3.3.1 Mass transfer mechanisms and mass function

The extreme gravitational potential of BHs provide a natural laboratory to study General Relativity (GR) and understand the physical processes it generates in its vicinity. The accreting matter onto the compact object emits X-ray photons which then can be detected by X-ray satellites in the orbit. Majority of the accreting compact objects show no evidence

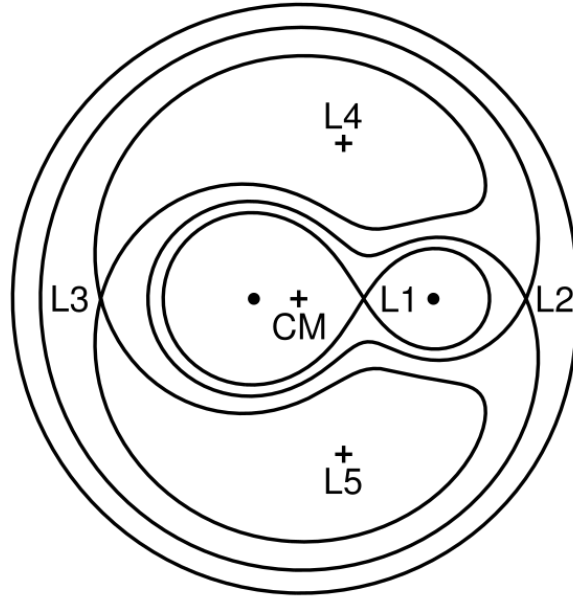


Figure 1.8 The figure is a 2D representation of the cross section (The Roche potential contours calculated for two point mass  $M_1$  and  $M_2$ ) of  $\phi(\mathbf{r})$

for periodic pulsations in their persistent emission. In the case of accreting BHs, this is a consequence of the presence of the event horizon. In the following sections, I will summarize some of the physical processes that affect the X-ray spectral and timing properties of BHs.

It is useful to discuss the basic matter transfer mechanisms to understand the X-ray production mechanisms. Black hole binaries (BHBs) contain an accreting black hole and a non-degenerate secondary (companion/donor) star. Gravitational potential that characterizes a binary system was derived by a French mathematician and astronomer who worked on celestial mechanics, Edouard Roche. For two point masses  $M_1$  and  $M_2$  in Keplerian Orbits around the center of their masses, the equipotential lines of the Roche potential has the form of (Frank et al. 1992):

$$\phi(\mathbf{r}) = -\frac{GM_1}{|\mathbf{r} - \mathbf{r}_1|} - \frac{GM_2}{|\mathbf{r} - \mathbf{r}_2|} - \frac{(\boldsymbol{\omega} \times \mathbf{r})^2}{2} \quad (1.4)$$

Figure 1.8 displays the Roche potential contours of an X-ray binary. The innermost solid line shows that each point mass has its own "Roche Lobe". The Roche lobe of each object defines a volume within which a particle is bound to one of the two objects. The equilibrium points (Lagrange points L1, ..., L5) shows where no force acts on a particle at those locations. L1 is a special point (a saddle point) where an outward momentum carrying matter can easily enter the Roche lobe of the compact object. There are three known different mass transfer mechanisms:

- Wind accretion: If the companion star is of an early type, it usually generates powerful stellar winds that can transfer matter into the Roche lobe of the compact object through Lagrange points L1 and L2. Typical mass transfer rates are  $10^{-11} - 10^{-8} M_{\odot}/yr$  (Frank et al. 1992).
- Roche Lobe overflow accretion: If the companion star is a LMXB, it may expand in size until it's Roche lobe is filled under the influence of gravitation of the compact object. And then, mass transfer starts to occur through L1. Typical mass rate for Roche lobe overflow accretion is  $10^{-11} - 10^8 M_{\odot}/yr$ .
- Be-stars: Be stars eject material at their equator, probably due to high spin of these stars. The ejected material can pass into the Roche lobe of the compact object, usually a NS for all known Be- companions.

No matter how the matter finds it's way into the compact object's Roche lobe, once it is in, the accreting matter will follow an orbit around the compact object since it carries angular momentum and will form an “*accretion disk*”. Before discussing the accretion disk models, it is useful to have a look at some very important disk parameters. The accreting material will slowly lose it's potential energy and angular momentum. Most of the lost energy is transferred into heat, resulting in a thermal emission from the heated disk. Disk luminosity generated by accretion disk can be estimated by (Shapiro and Teukolsky 1983):

$$L_{acc} = 2\eta \frac{GM\dot{M}}{R_S} = \eta \dot{M}c^2 \quad (1.5)$$

where  $\eta$  depends on the angular momentum of the compact object. Typical luminosity obtained for an accreting BH system is  $\sim 10^{37} erg s^{-1}$ . There is also a limit to the produced X-ray luminosity from the accretion disk. The gravitational pull of the BH limits the radiation pressure generated by X-ray emission from the disk. Sir Arthur Stanley Eddington assumed a spherical accretion and derived the “Eddington Luminosity” by:

$$\frac{GMm_p}{r^2} = L_{Edd} \frac{\sigma_T}{4\pi cr^2} \quad (1.6)$$

where  $m_p$  is the proton mass and  $\sigma_T$  is the cross section for Thompson scattering. Solving for  $L_{Edd}$  for a BH mass  $M/M_{\odot}$ ,

$$L_{Edd} = 4\pi \frac{cGMm_p}{\sigma_T} = 1.3 \times 10^{38} \left( \frac{M}{M_{\odot}} \right) erg/s \quad (1.7)$$

Then using the luminosity vs. mass accretion rate relation,  $L = \epsilon \dot{M}c^2$ , the corresponding mass accretion rate limit can be found as:

$$\dot{M}_{Edd} = L_{Edd}/c^2 = 1.7 \times 10^{17} \left( \frac{M}{M_{\odot}} \right) g s^{-1} \quad (1.8)$$

### 1.3.3.2 The standard “ $\alpha$ ” Accretion Disk

The famous paper by Shakura and Sunyaev (1973) formulated the theory of standard accretion disk or the  $\alpha$  disk model. This model proposes a geometrically thin and optically thick gaseous disk that orbits around the black hole. The disk is supported by the pressure,  $p$ , of the disk against the gravitational forces. The viscous stress torques descend the material inwards to lower orbits. The lost angular momentum energy is converted into heat. The model formulates the viscous stress tensor by the disk pressure:  $t_r\Phi = \alpha p$  ( $\alpha < 1$ ), assuming the matter is turbulent. Here,  $\alpha$  is a free parameter however, the value it assumes is not well established. Shapiro and Teukolsky (1983) tried to compute the  $\alpha$  parameter via comparative observations and found a value between 0.1 – 1. The radiation from the  $\alpha$  disk is in the form of multi-color blackbody (Mitsuda 1984; Merloni et al. 2000). The radial temperature distribution of the spectrum is  $T(r) \sim r^{-3/4}$ . However, this theory fails to take into account the general relativistic effects and the magneto-rotational instabilities. There have been many studies focusing on understanding the angular momentum transfer in the disk, some of which proposed improved models (Figure 1.9) (Gierliński et al. 2001; Balbus and Hawley 1991; Hawley and Balbus 1991).

### 1.3.3.3 The Accretion Disk Corona

The  $\alpha$  disk model can somewhat estimate the SS spectrum but fails to describe the hard X-ray emission in the form of a power-law. Scientists proposed the presence of a hot, low density plasma (Corona) where the soft seed photons coming from the cold accretion disk is Compton-scattered to higher energies (Liang and Price 1977; Bisnovatyi-Kogan and Blinnikov 1977; Sunyaev and Trümper 1979; Sunyaev and Titarchuk 1980). The standard model of ADC has quickly become the one proposed by Sunyaev and Trümper (1979). This model explains the observed luminosities and the hard spectra of GBHTs. Since the corona is optically thin, some seed photons from the disk may not scatter, therefore can explain both the hard and the soft components in the spectrum. Commonly accepted sombrero geometry and emission components of the disk and the corona can be seen in Figure 1.10. Comptonization corona, coupled with the disk, is a very complex structure and has been studied extensively (Hua and Titarchuk 1995; Wilms et al. 1997; Wilms 1998; Zdziarski 1998; Malzac 2003; Meyer et al. 2000; Psaltis 2001). Since the Comptonization is very important explaining the hard X-ray spectra of GBHTs, I will now explain it’s theory.

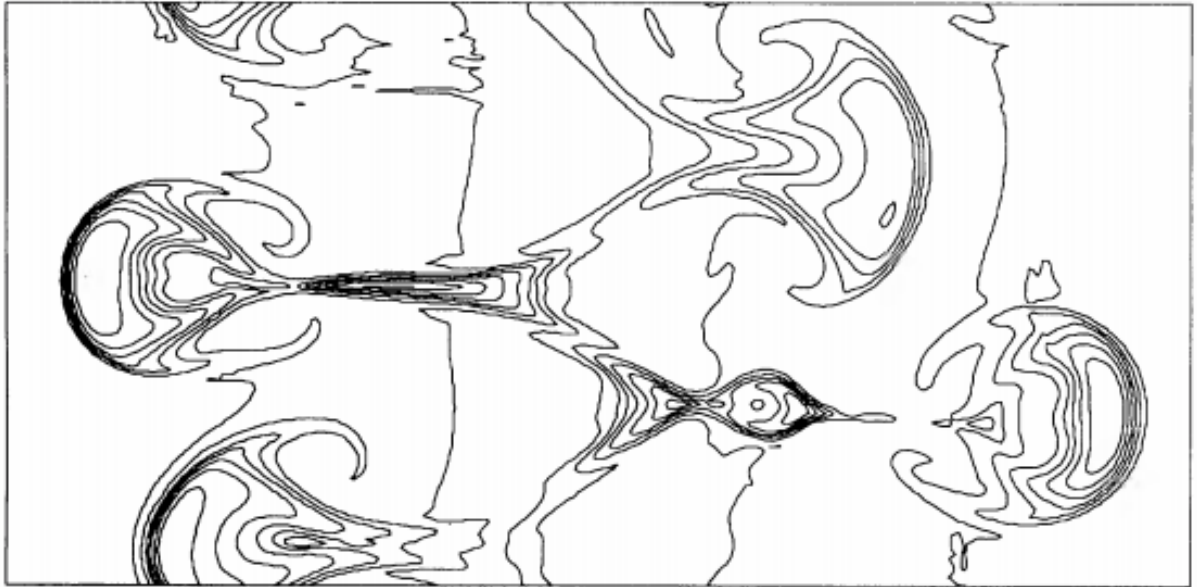


Figure 1.9 The angular momentum contour lines. A vertical cross section of the accretion disk (tilted in the figure) that was observed during the simulation of magneto-rotational instabilities. (adopted from Hawley and Balbus (1991))

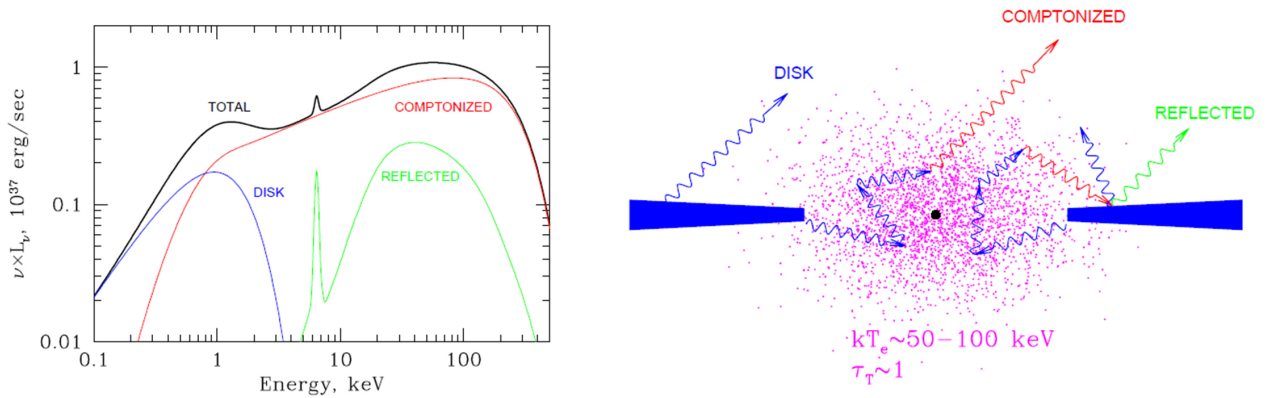


Figure 1.10 The main emission components from an accreting black hole (left) and a schematic of the geometry of the accretion and the corona in the hard state (right).(adopted from Gilfanov (2009))

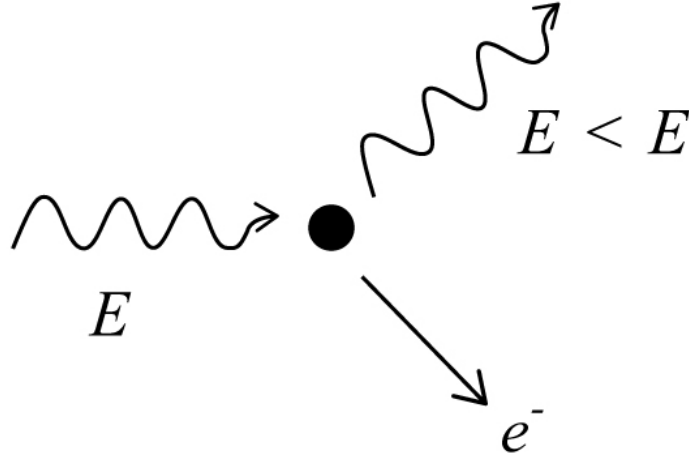


Figure 1.11 Compton scattering of a photon from an electron at rest.

### Comptonization

The classical elastic scattering of the incident photons is known as the Thomson scattering. In this theory, the photons are treated as continuous electromagnetic waves which then induce dipole radiation from an oscillating electron. The energy of the incident photon is much less than the mass energy of the electrons ( $h\nu \ll m_e c^2$ ). The differential Thomson cross-section for unpolarized incident EM radiation scattering at angle  $\Theta$  is given by the formula:

$$\frac{\partial \sigma_T}{\partial \Omega} = \frac{1}{2} r_0^2 (1 + \cos^2 \Theta) \quad (1.9)$$

where  $r_0 = \frac{e^2}{m_e c^2} = 2.82 \times 10^{-13} \text{ cm}$  is the electron radius. The integration of the equation 1.9 over all scattering angles yields the total Thomson cross-section:

$$\sigma_T = \frac{8}{3} \pi r_0^2 = 6.652 \times 10^{-25} \text{ cm}^2 \quad (1.10)$$

An important result of this is that it shows the inverse relation between the scattering cross section and the mass of the particle ( $\sigma_T \propto \frac{1}{m^2}$ ). This implies, if the particles are protons, the scattering cross-section would be suppressed by a factor of  $(\frac{m_e}{m_p})^2 \sim 10^{-7}$ . Particles other than electrons will in turn have no significant cross-sections.

The Compton scattering treats the photons as particles, therefore allowing the exchange of the energy and momentum with the colliding electron. In the simple Compton scattering process a photon of energy  $E$  collides with an electron at rest and transfers kinetic energy to the electron (Figure 1.11). The reduced energy of the photon is given by:

$$E' = \frac{E}{1 + \frac{E}{m_e c^2} (1 - \cos\theta)} \quad (1.11)$$

The differential cross-section and the angular momentum distribution of electrons after the collision is given by the Klein-Nishina formula which takes into account the Quantum Electrodynamics (QED) effects:

$$\frac{\partial \sigma_{es}}{\partial \Omega} = \frac{3}{16\pi} \left(\frac{E'^2}{E}\right) \left(\frac{E}{E'} + \frac{E'}{E} - \sin^2\theta\right) \quad (1.12)$$

It can be seen that, when  $E=E'$ , this equation reduces to the classical expression given in Eq. 1.9. The total cross-section can be obtained by integrating the Eq. 1.12 over all scattering angles (Rybicki and Lightman 1979). For high energies ( $> 30keV$ ), quantum effects reduce the Klein-Nishina cross-section by more than 10%. Since the scattering would be concentrated in the forward direction due to the relativistic beaming, the Compton cross-section would become less efficient.

However, in astrophysical sources, the electrons are not at rest but have considerable thermal motion. It is assumed that they have a relativistic Maxwellian velocity distribution with a characteristic temperature,  $T_e$ :

$$N(\gamma) \sim \gamma^2 \beta e^{-\frac{\gamma m_e c^2}{kT_e}} \quad (1.13)$$

where  $\beta = \frac{v_e}{c}$  is the electron velocity and  $\gamma = (1 - \beta^2)^{-\frac{1}{2}}$  is the Lorentz factor. If the incident photon energy is much lower than the electrons, on average, they gain energy from the Compton collisions. This process is called the thermal Comptonization due to the Maxwellian velocities of electrons.

In the case of GBHTs, the corona with  $T_e \sim 100$  keV ( $10^9 K^\circ$ ) is the hot electron plasma that Compton up-scatters the seed photons coming from the disk with  $E \sim 100$  eV ( $10^6 K^\circ$ ). The average energy change of the scattered photon when the electrons are at rest is:

$$\left\langle \frac{\Delta E}{E} \right\rangle = -\frac{E}{m_e c^2}, \text{ (per collision)} \quad (1.14)$$

which is obtained by averaging Eq. 1.11 over all scattering angles. On the other hand, electrons with  $kT_e < m_e c^2$  lead to an average photon energy change of (Rybicki and Lightman 1979):

$$\left\langle \frac{\Delta E}{E} \right\rangle = \frac{4kT_e - E}{m_e c^2} \quad (1.15)$$



This implies that the photons gain energy as long as  $E < kT_e$ . This establishes the conditions for the cooling of the electrons unless the energy is deposited into the plasma by other physical processes. The approximate total energy change for a photon crossing a Comptonizing plasma of optical depth  $\tau_c$  can also be calculated. Assuming the photon energy is much smaller than the electron temperature, the average fractional energy change per scattering is  $\frac{4kT_e}{m_e c^2}$ . If we multiply this value by the average number of scatterings, we can obtain the total energy change. According to the "random walk theory", the average number of scatterings is  $\max(\tau_c, \tau_c^2)$ . As a result, the total fractional energy change is:

$$y = \frac{4kT_e}{m_e c^2} \max(\tau_c, \tau_c^2) \quad (1.16)$$

where  $y$  is the "Compton  $y$ -parameter".

The repeated scatterings yield a Compton spectrum which can be solved via Kompaneets equation (Rybicki and Lightman 1979). This equation describes the photon distribution function due to repeated scatterings in the limit of large optical depths  $\tau_c > 1$  and for  $kT_e \ll m_e c^2$ . General solutions to the Kompaneets equation are analytically complex and usually calculated numerically (Sunyaev and Titarchuk 1980).

For  $y \ll 1$ , only Thomson scattering is important and the initial soft photon spectrum will stay intact. For  $y \gg 1$ , a "saturated" spectrum is obtained due to the conservation of photon number. The Compton scattering of higher energy photons and the inverse-Compton scattering of lower energy photons, create a competing event which "thermalizes" the spectrum to the temperature  $T_e$ . At higher energies the spectrum becomes a Wien law with a mean photon energy of  $3kT_e$ .

For  $y \gtrsim 1$ , inverse-Compton process does not saturate to the Wien spectrum. Only the high energy part of the spectrum saturates. Kompaneets equation yields an "unsaturated" solution for the very low energy photons, in which the spectrum evolves to the Wien shape by multiple scattering of soft photons. For escaped photons at intermediate energies, a power-law solution describes the Comptonized spectrum:

$$I_\nu \propto E^{3+m}, m = -\frac{3}{2} \pm \left(\frac{9}{4} + \frac{4}{y}\right)^{-\frac{1}{2}} \quad (1.17)$$

This unsaturated solution identifies the power-law component commonly used in the GBHT spectrum fitting. Figure 1.12 shows the Monte Carlo simulations of photon spectrum from a hot Comptonizing plasma.

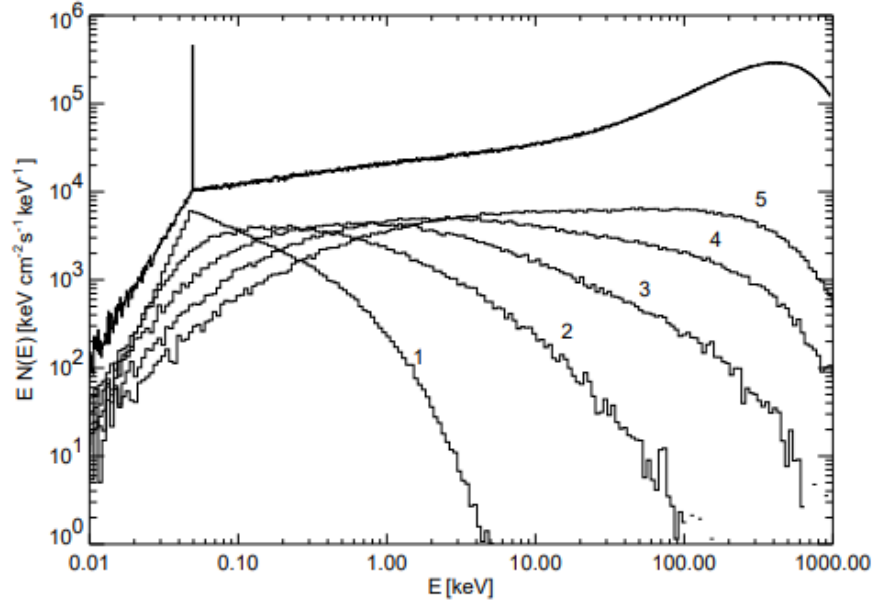


Figure 1.12 Monte Carlo simulation of spectra of Comptonized seed photons with energy  $E \sim 50 \text{ keV}$  from a point source at the center of the sphere (with a Thomson optical depth of  $\tau \sim 5$ ). The total spectrum (top) and emerging spectra of scattering orders 1-5 can be seen (adopted from Wilms (1998))

#### 1.3.3.4 Advection Dominated Accretion Flows (ADAFs)

The hard X-rays observed in the low rate accretion sources cannot be explained by the standard model. Hints of why we observe these "faint" hard X-rays were studied extensively. It is considered that, a disk of such low density that the protons are unable to pass their energy to the electrons on the time scales of the accretion. Instead, the protons either advect into the BH or transport the energy outwards via outflows (Ichimaru 1977; Blandford and Begelman 1999; Narayan and Yi 1995; Narayan et al. 1998).

Since ADAF requires a low density plasma and very little proton-electron collisions, there is a maximum accretion rate that ADAF can sustain (Beloborodov 1999):

$$\max\left(\frac{\dot{M}}{M_{\text{Edd}}}\right) \sim 10\alpha^2 \quad (1.18)$$

where  $\alpha < 0.1$  is a free parameter.

The accretion disk becomes hot and geometrically thick (optically thin), therefore radiation is under-luminous. The hard state of low luminosity sources can be explained by ADAF (Esin et al. 1997, 2001). Another important feature of ADAF is, there is a transition at a critical radius  $r_1 r$  where the cold accretion disk becomes a hot two-temperature flow which emits hard X-rays by Comptonization of soft photons. The seed soft photons may be arising

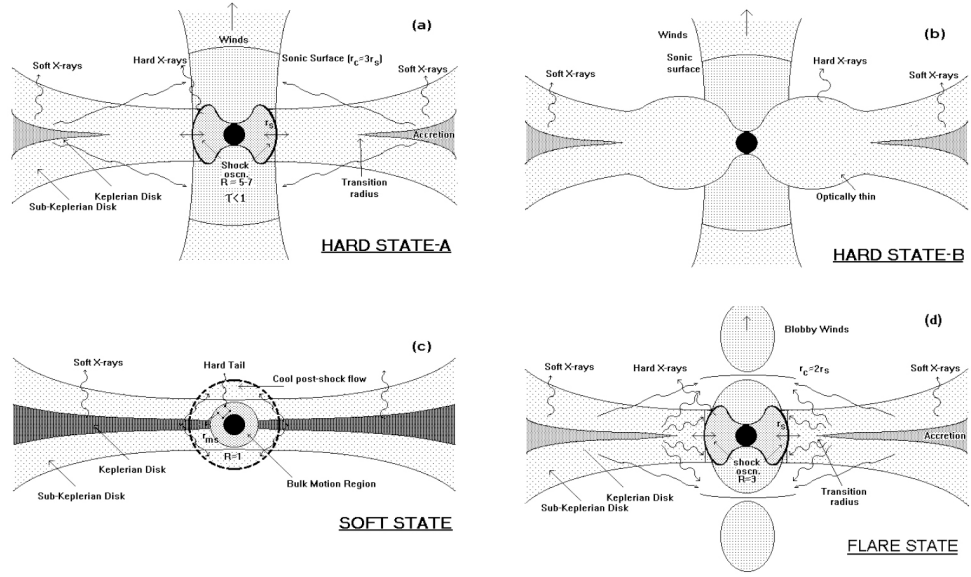


Figure 1.13 A cartoon diagram of ADAF in different spectral states.(adopted from Chakrabarti (2000))

from the outer parts of the accretion disk and/or synchrotron or bremsstrahlung radiation from the ADAF itself. A schematic that shows the ADAF in different states can be seen in Figure 1.13. Note that ADAF do not consider timing properties. There have been many additions to the ADAFs but they are out of the scope of this thesis and will not be discussed. For a detailed description, see Chakrabarti (2000).

## Reflection

A very important component that is seen in the GBHT spectra is the reflection component. The broad and shallow absorption and iron emission lines seen in the continuum X-ray spectra of GBHTs are explained as the result of reprocessing of hard X-rays that are reflected from the accretion disk. Notably, a fluorescent iron line at  $\sim 6.4keV$ , a broad absorption feature between  $\sim 7 - 20keV$ , a reflection hump at  $\sim 30keV$  due to reduced Klein-Nishina cross-section and Compton down-scatterings at high energies. These features can be seen in Figure 1.14.

The shape and the amplitude of these reflection features strongly depend on the geometry of the source and the composition of the material in the cold accretion disk. For a detailed description, see Fabian and Ross (2010). Further investigations of the reflection components also revealed an important correlation between the disk solid angle and the spectral index.

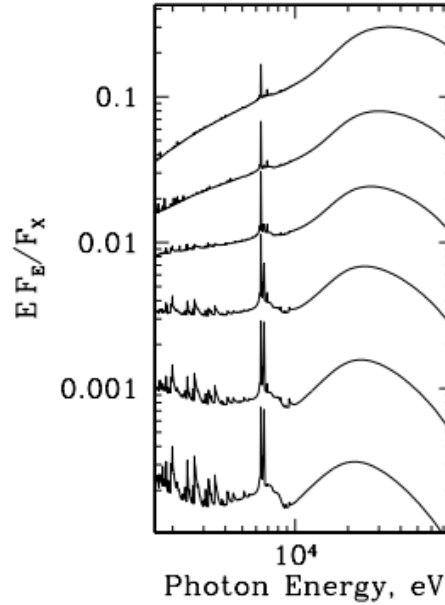


Figure 1.14 Reflection spectra obtained by NKK simulation of incident photons for 6 different spectral indices  $\Gamma = 1.5, 1.7, \dots, 2.5$ . As the spectra gets harder, higher gas temperatures and ticker optical depths develop. (adopted from Done and Nayakshin (2001))

## 1.4 Dust Scattering Theory

The interstellar medium (ISM) both absorbs and scatters the photons. Both processes are highly energy dependent. At X-ray energies, small-angle scattering is dominant and creates an arc-minute scale dust scattering halo (DSH) around sources with significant ISM along the line of sight. A cartoon depiction of the dust scattering geometry for a single scattering can be seen in Figure 1.15.

The scattering of X-rays by the ISM was first predicted by Overbeck (1965) and first observed but not recognized by Toor et al. (1976) using a rocket-borne detector during a lunar occultation of the Crab Nebula. Later, first conscious detection of a DSH around the galactic source GX 339-4 was achieved by Rolf (1983) using the Einstein/IPC. DSH of 28 sources were then found and studied by Predehl and Schmitt (1995). Theoretical calculations of the observed halo intensity and time delays of the scattering photons have been established by extensive studies (Molnar and Mauche 1986; Mathis et al. 1991; Trümper and Schönfelder 1973). Analysis in all cases were accomplished by showing that the measured radial extent of the source was larger than the expected point-spread function (PSF) of the specific telescope mirrors.

Predehl and Schmitt (1995) found that the amount of scattering by the ISM was correlated with the measured absorption of the soft X-rays by the ISM. Typically, the ISM is in the

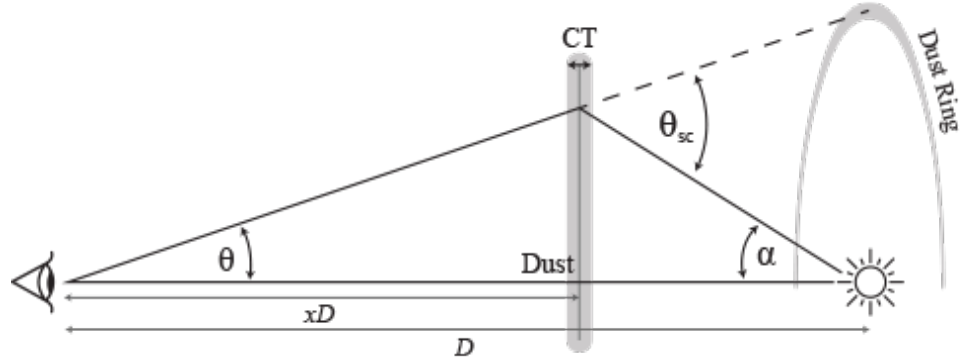


Figure 1.15 Geometry of dust scattering mechanism from dust cloud. The source distance is given by  $D$ , and the distance to the dust cloud from the observer is given by  $xD$ .  $\theta$  is the observed scattering angle,  $\theta_{sc}$  is the physical scattering angle and  $CT$  is the cloud thickness. Dust ring represents the halos seen in modern instruments.

form of different layers of molecular clouds. If the source exhibits timing variability, the halo emission also reflects the variability of the source. And if the source exhibits flares, the DSH take the form of discrete rings, each corresponding to different layers of molecular clouds in the line of sight. The study of DSHs have been proven useful in understanding the physical properties of dust grains (Corrales and Paerels 2015; Xiang et al. 2011; Ling et al. 2009), the variations during eclipses (Audley et al. 2006; Jin et al. 2018) and references therein, optical and X-ray absorption (Predehl and Schmitt 1995; Costantini et al. 2005; Corrales et al. 2016), the dust-to-gas relations in the ISM (Güver and Özel 2009; Zhu et al. 2017), and the distance estimations (Xiang et al. 2007; Tiengo et al. 2010; Kalemci et al. 2018).

Predehl and Schmitt (1995) found a strong correlation between the dust ( $\tau_{sca}$ ) and hydrogen column densities ( $N_H$ ):

$$\tau_{sca} = 0.49 x(N_H/10^{22} cm^{-2})x(E/keV)^{-2} \quad (1.19)$$

Accordingly, all sources with high  $N_H$  are behind ample amount of dust in our *line-of-sight* (LOS). The scattering cross-section ( $\tau_{sca}$ ) scales as  $\sim E^{-2}$  where  $E$  is the energy of the X-ray photon. The X-ray photons, scattered back into the observer LOS, travel a longer path than the un-scattered photons (Figure 1.15). Longer paths cause delays (lags) from the observer's perspective. Consequently, if the entire DSH is in the field of view (FOV) of the instrument (i.e RXTE ), loss of coherence and a decrease in the rms amplitude of variability is expected. The dust scattering can also change the observed spectrum since it depends on the energy and the location of the dust cloud relative to the source. The delay can be on the order of days (Molnar and Mauche 1986). Usually, the shape of the PSD would stay intact but it's rms variability would be reduced since the dominant variability timescales are between ms

to a few tens of seconds in GBHs.

Typically, the interaction of photons with spherical grains can be explained with the Mie solution. For sufficiently small grains, photon wavelengths and scattering angles, a simple analytic solution can be obtained, namely "Rayleigh-Gans" (RG) approximation (Mathis et al. 1991).

Using the geometry shown in Figure 1.15, we can derive many important parameters of the process. The time delay ( $\Delta t$ ) of the scattered photons from a source at a distance D and a cloud at xD is:

$$\Delta t = \frac{x D \theta^2}{2c(1-x)} \quad (1.20)$$

where c is the speed of light and  $\theta$  is the observed angle ( $\theta = \theta_{sca} - \alpha$ ).

The observed intensity of a DSH ring with outburst timescale shorter than or comparable to  $\Delta t$  is:

$$I_v = N_H \frac{d\sigma_{sca,E}}{d\Omega} \frac{F_v(t = t_{obs} - \Delta t)}{(1-x)^2} \exp(-\sigma_{ph,E} \sum_{i=1}^r N_{H,r}) \quad (1.21)$$

where  $\frac{d\sigma_{sca,E}}{d\Omega}$  is the differential dust scattering cross-section per hydrogen atom,  $F_v(t)$  is the flux of the flare at time t,  $\sigma_{ph,E}$  is the total photo-electric cross-section at energy E,  $N_H$  is the hydrogen column density corresponding to the source. The flux density  $F_v$  can be calculated by integrating the Eq. 1.20 over  $\theta$  and keeping  $\frac{\partial \sigma_{sca,E}}{\partial \Omega}$  constant:

$$F_{Halo,E} = \frac{2\pi c N_H}{x(1-x)D} \frac{d\sigma_{sca,E}}{d\Omega} F_v \quad (1.22)$$

The scattering cross-section depends strongly on the scattering angle and energy and also the dust distribution along the LOS, with:

$$\frac{d\sigma_{sca,E}}{d\Omega} = \int_{a_{min}}^{a_{max}} da \frac{dN}{da} \frac{d\sigma(\theta_{sc}, E, a)}{d\Omega} \sim C \left(\frac{\theta_{sc}}{1000''}\right)^{-\alpha} \left(\frac{E}{1 \text{ keV}}\right)^{-\beta} \quad (1.23)$$

where C is the normalization constant at 1000" and 1 keV,  $\alpha \sim 3 - 4$  and  $\beta \sim 3 - 4$  (Draine 2003).

The physical scattering angle can simply be found using Figure 1.15 again:

$$\theta_{sc} = \frac{\theta}{(1-x)} \quad (1.24)$$

So the intensity and the flux of the halo decreases as the time delays increase:

$$F_{Halo} \propto \Delta t^{-\frac{\alpha}{2}} \quad (1.25)$$

## 1.5 1E 1740.7–2742

1E 1740.7–2742 is a known microquasar which is located 50" of the Galactic Center (GC). It is one of the brightest at the same time hardest persistent X-ray source (together with GRS 1758-258) (Sunyaev et al. 1991a) in the vicinity of the Galactic center. 1E 1740.7–2742 was discovered by Hertz and Grindlay (1985) using the *Einstein/IPC* instrument and it was first suggested that it might contain a BH by Sunyaev et al. (1991b).

1E 1740.7–2742's HS spectral shape and X-ray luminosity is significantly similar to the black hole candidate Cyg-X1 in terms of spectral and timing properties (Sunyaev et al. 1991b). Kuznetsov et al. (1997) found a correlation between the spectral hardness and the hard X-ray luminosity for  $L_x \lesssim 10^{37} \text{ erg s}^{-1}$ , supporting the BH claims. 1E 1740.7–2742 also shows strong aperiodic and *quasi*-periodic X-ray variabilities along with relativistic radio jets, again similar to BHCs (Smith et al. 1997; Lin et al. 2000).

Due to high amount of  $N_H$  ( $\sim 10^{23}$ ) along the GC, it's optical/IR counterpart has been subject to speculation (Leahy et al. 1992; Martí et al. 2010). The spectrum of 1E 1740.7–2742 in the HS can usually be fitted by an absorbed power-law or a Comptonization model (Hua and Titarchuk 1995; Bouchet et al. 2009).

# Chapter 2

## X-ray Instruments and Data Analysis

### 2.1 X-ray Instruments

#### 2.1.1 *XMM-Newton* Satellite

With 4 tonnes of weight and 10 meters height, *XMM-Newton* is the largest scientific satellite launched by the European Space Agency (ESA). It was launched on December 10, 1999 and started scientific operations on July 1st, 2000. *XMM-Newton* spacecraft carries a set of three CCD cameras (Figure 2.1), namely European Photon Imaging Camera (EPIC). Two of these cameras are MOS (Metal-Oxide Semiconductor) CCD arrays. They are equipped with the gratings of the Reflection Grating Spectrometers (RGS). This setting diverts nearly the half of the incident X-ray flux to RGS detectors so that 44% of the flux goes into the MOS CCDs. The third camera is unobstructed and has a PN camera at the focus. There is another scientific instrument named Optical Monitor (OM) for multiwavelength observations between 170-650 nm of the central 17 arc minute square region of the X-ray FOV.

EPIC cameras provide highly sensitive imaging observations with a FOV of 30 arc minutes in the energy range 0.15-15 keV. They have a moderate spectral ( $E/\Delta E \sim 20 - 50$ ) and angular resolution (PSF  $\sim 6$  arcsec FWHM). These cameras provide different operating modes with different experiment properties:

- **Full Frame and Extended Full Frame** (PN only): This mode makes use of the all pixels therefore provide a full FOV coverage.
- **Partial Windows**

**EPIC-MOS:** There are 2 types of partial windows which uses only the central CCD of the both MOS cameras. In “small window mode” an area of 100x100 pixels is read out. In “large window mode” an area of 300x300 pixels is read out.



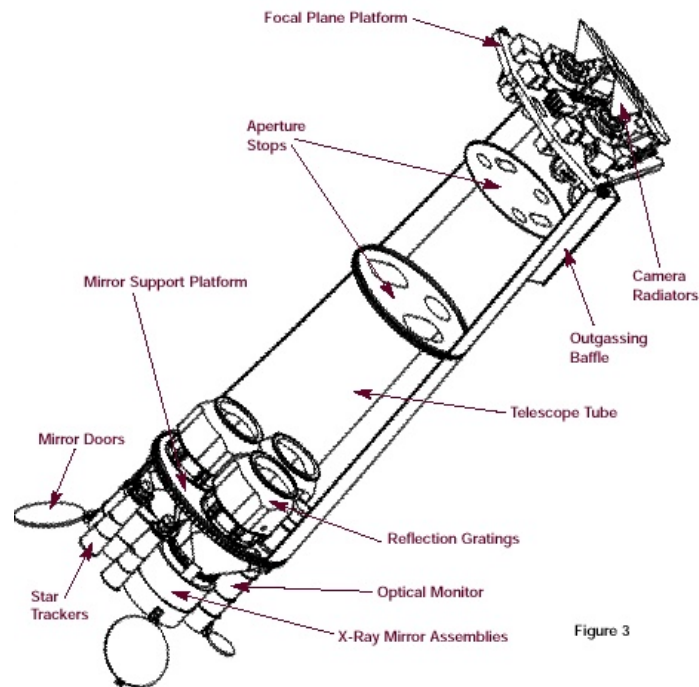


Figure 2.1 A schematic of the *XMM-Newton* spacecraft.

**EPIC-PN:** In “large window mode” only half of the area of all 12 CCD are used, whereas in “small window mode” only the central CCD is used.

- **Timing**

**MOS & PN:** Imaging is made only in one dimension. Along the row direction, the data from a predefined area of one CCD is collapsed into a one-dimensional row to be read out at high speed.

**Burst Mode (PN only):** This mode provides very high time resolution at the expense of low duty cycle (3%).

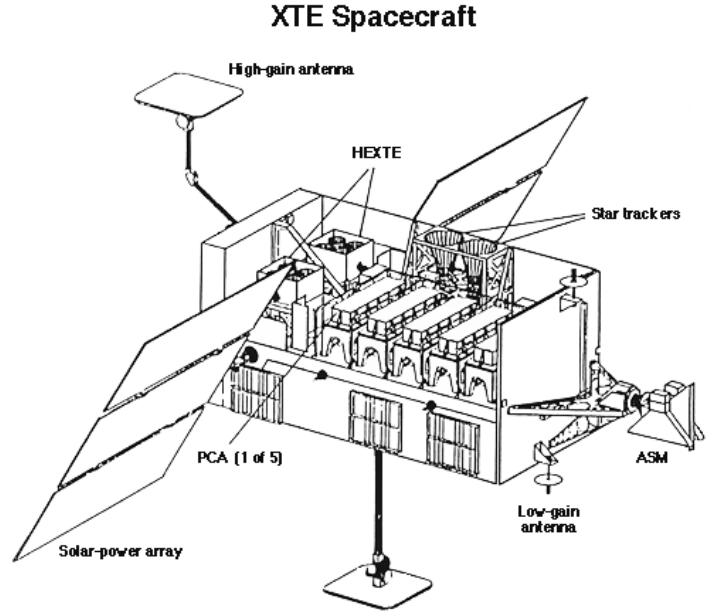


Figure 2.2 A schematic of the *Rossi X-ray Timing Explorer* spacecraft.

### 2.1.2 The *Rossi X-ray Timing Explorer* Satellite

The *Rossi X-ray Timing Explorer* (RXTE) was launched on December 30, 1995 from Kennedy Space Center in Florida, US. It was put into a low-earth orbit at an altitude of 580 km with an inclination angle of  $23^\circ$  that corresponds to a 90 minute orbital period with a Delta II rocket. It was originally designed for a lifetime of 2 years but it served for 16 years until it was decommissioned on January 5th, 2012. The spacecraft can be pointed very easily only by providing the coordinates of the source and a slewing rate ( $\sim 6^\circ$  per minute) which allows it to be pointed to transient sources very quickly.

There are three different instruments on board of RXTE (Figure 2.2); 1) Proportional Counter Array (PCA), 2) High Energy X-ray Timing Experiment (HEXTE) and 3) All-Sky Monitor (ASM). PCA and HEXTE instruments are co-aligned but they cover different energy ranges. This allows high effective area coverage for a wide energy range. That way RXTE covers an energy range of  $2 - 250$  keV while PCA covers lower energy range ( $2 - 60$  keV) and HEXTE covers the high energy part ( $15 - 250$  keV) with an overlap between  $15 - 60$  keV. Both instruments are equipped with collimators that yield a  $1^\circ$  of Full Width Half Maximum (FWHM). These capabilities makes RXTE an ideal tool to investigate BH systems since it can detect photons from different emission regions.

Main objective of the RXTE is temporal studies of X-rays from strong sources. PCA has a time resolution of  $1\mu s$ . It's large area with high throughput allows the instrument to achieve satisfactory signal to noise ratios in each time bin. This thesis focuses on spectral and temporal analyses using the PCA instrument, therefore other instruments are not discussed

in this section. A detailed technical description of the other instruments along with PCA can be found in RXTE Technical Appendix F ([https://heasarc.gsfc.nasa.gov/docs/xte/RXTE\\_tech\\_append.pdf](https://heasarc.gsfc.nasa.gov/docs/xte/RXTE_tech_append.pdf)).

### 2.1.2.1 The Proportional Counter Array (PCA)

The Proportional Counter Array was built by NASA's Goddard Space Flight Center. It consists of nearly identical 5 proportional counter units (PCUs) those are sensitive in the 2 – 60 keV energy range. For convenience they will be referred as PCUs 0-4.

Working principle of PCUs rely on the principle of multiplication of gases to measure the energy of the incident X-ray photon (Knoll 1979). The incident X-ray photon interacts with the gas upon entering the instrument via photoelectric absorption then emits a photoelectron. These photo-electrons create a cloud of electron-ion pairs. Due to the voltage applied to the gas, electrons and ions migrate to their corresponding electrodes. Migration process allows for collisions of electrons and ions with the neutral gas. Ions gain very little energy via the collisions due to their low speeds while free electrons are easily accelerated by the applied electric field and can reach critical kinetic energies that allow for further production of electron-ion pairs through collisions. Secondary electrons created by this process are also subject to the same mechanics, meaning they cause further ionizations in the gas and so on. This phenomena is called a *Townsend avalanche*. By adjusting the voltage (via using different materials) applied to the gas, size of this avalanche and consequently the amount of charge collected can be set such that the energy of the incident photon is linearly proportional to the charge created at the electrodes.

The effective area of the 5 PCUs can be seen in Figure 2.3. Two complications at energies  $\sim 5$  keV and  $\sim 35$  keV can be seen from the figure. These complications are caused by the atomic physics of the gasses used in the detector. The photoelectric cross section of the Xenon gas drops below each of the L-edges. Photons having energies just above the edge will be absorbed near the surface layer and eject a L-shell electron. The mean free path of the incident photon is much smaller than the M to L shell transition, therefore there is a possibility of photons escaping from the front of the detector. Likewise, the photoelectric cross section of the Xenon gas increases sharply at the K-edge ( $\sim 35$  keV) with increasing energy. Total collecting area of 5 PCUs is  $\sim 6500$  cm<sup>2</sup> with a nominal energy resolution of %18 at 6 keV.

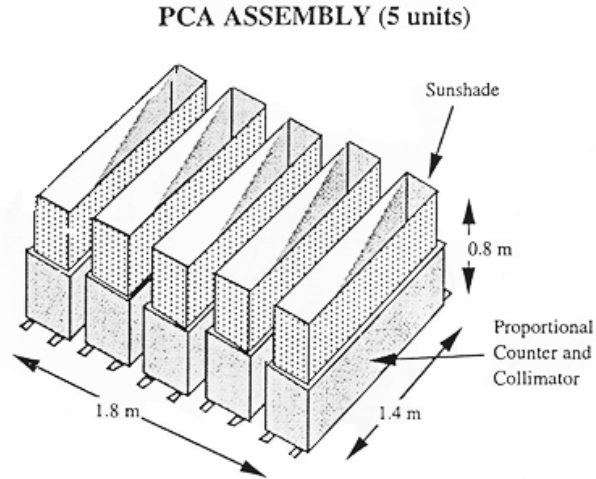


Figure 2.3 A schematic of RXTE PCA assembly

### 2.1.3 *Chandra* X-ray Observatory

NASA's *Chandra* X-ray Observatory was deployed by Space Shuttle Columbia on July 23, 1999. It consists of 4 science instruments (Figure 2.4): the focal plane instruments Advanced CCD Imaging Spectrometer (ACIS) and High Resolution Camera (HRC) and two grating arrays that diffract the X-rays according to their energies, High and Low Energy Transmission Grating Spectrometers (HETGS and LETGS). The energy range is 0.1-10 keV with a high spatial resolution of 0.5 arc minute FWHM.

The Advanced CCD Imaging Spectrometer (ACIS) is one of the two focal plane instruments. It consists of two different array setups (Figure 2.5) of 1024x1024 pixel CCDs (ACIS-I and ACIS-S) with an energy resolution of  $\sim 100$  eV. ACIS-I is a front illuminated 16'x16' FOV array. ACIS-S is a grating readout array which can also perform imaging. S1 and S3 CCDs are back illuminated. It has a good low energy quantum efficiency with a higher throughput.

The High Resolution Camera (HRC) is the other focal plane instrument. It produces very high quality images thanks to matching of its imaging capability to the focusing power of its mirrors. HRC-I is a microchannel plate imager with a 30'x30' FOV. Its energy resolving power  $R(\Delta E/E)$  is  $\sim 1$ . HRC-S is a low energy grating readout array with a time resolution of 16  $\mu$ s. When the HRC-S is paired with LETG it can provide an energy resolving power  $R > 1000$ .

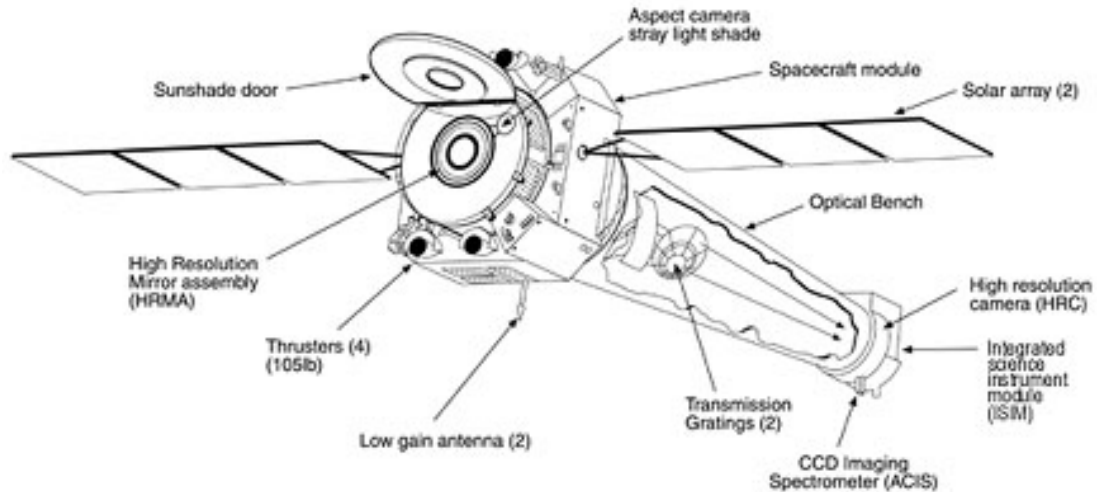


Figure 2.4 A schematic of Chandra X-ray Observatory

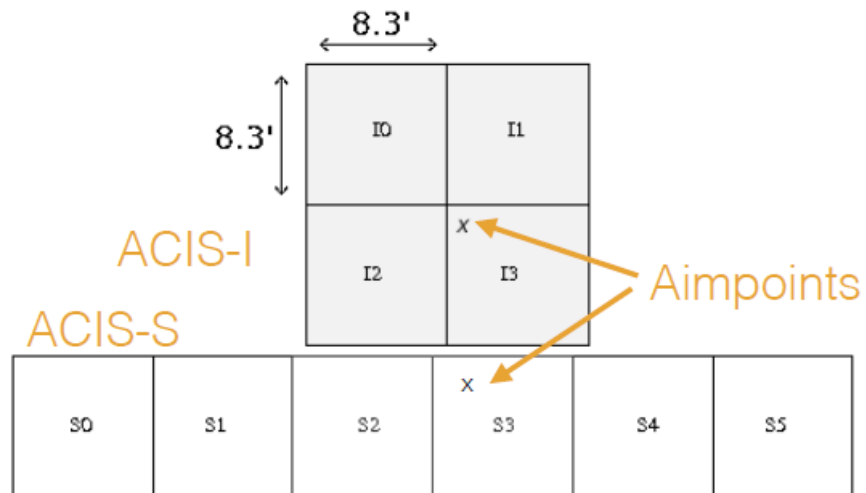


Figure 2.5 A schematic of ACIS arrays with their aimpoints marked with an 'X'.

Gratings are commonly used for specific observations:

- **LETG/HRC-S** is usually used for soft sources ( $E < 1$  keV) such as stellar coronae, white dwarf atmospheres and cataclysmic variables.
- **LETG/ACIS-S** is usually used for harder sources such as AGNs and XRBs.
- **HETG/ACIS-S** is used for hard sources ( $E > 1$  keV).

## 2.2 Spectral Analysis and models

### 2.2.1 Spectral Analysis

One of the primary methods we use to extract information from the observations is obtaining the photon/source spectrum. However, this cannot be measured directly with the detectors. The measured spectrum is affected by the instrumental responses. To obtain the “intrinsic” source spectrum we must take into account the effective area, the energy resolution of the detectors and the photon counting statistics. The photon spectrum  $C(I)$  is represented by (Arnaud 1996; Jahoda et al. 1996):

$$C(I) = T \int \text{RMF}(I, E) \text{ARF}(I, E) S(E) dE + N(I) \quad (2.1)$$

where  $T$  is the exposure time,  $\text{RMF}(I, E)$  is the detector response matrix,  $\text{ARF}(I, E)$  is the effective area of the detector,  $N(I)$  is the additive noise,  $S(E)$  is the incident photon spectrum. The  $\text{RMF}$  and the  $\text{ARF}$  are mathematical functions that relate the observed counts to the “incident” source photon spectrum. Note that, the  $\text{RMF}$  and the  $\text{ARF}$  are combined to a single response function in *RXTE* while *XMM-Newton* and *Chandra* uses separate functions. Assuming the noise component  $N(I)$  is determined, the  $\text{RMF}$  and  $\text{ARF}$  produce the majority of the systematic uncertainties in the source spectrum. The observations of the “standard” X-ray source the Crab Pulsar is used to calibrate the  $\text{RMF}$  and  $\text{ARF}$ . Further complications arise from the inversion of Eq 2.1. The response matrices are often non-linear and have off-diagonal elements leading to a non-unique solution. A way to overcome this is to choosing any model spectrum  $S(E)$  and folding it with the  $\text{RMF}$  and  $\text{ARF}$  finally obtaining the predicted counts  $C_p(I)$ . Comparison of  $C_p(I)$  with  $C(I)$  is then evaluated by a fit statistic to see if the model describes the data. “Reduced chi-squared”  $\chi_{red}^2$  is the most used fit statistic in the field:

$$\chi_{red}^2 = \frac{\chi^2}{d.o.f.} = \frac{\sum(C(I) - C_p(I))^2 / (\sigma(I)^2)}{d.o.f} \quad (2.2)$$

where  $\sigma(I)$  is the error of the energy channel  $I$  and is found by  $\sigma(I) = \sqrt{C(I)}$  and d.o.f. is the number of degrees of freedom. By doing some iteration of the model parameters a value close to 1 which means a good fit can be achieved. However, it is important to watch out for the local minima that could trick you during the iterations (Figure 2.6). In this case, one should check the model parameters and see if they are consistent with the current state of the source.

If values of  $\chi_{red}^2 \gg 1$  is obtained then the fit is a poor one while  $\chi_{red}^2 \ll 1$  means the errors of the data have been overestimated. But, one should always keep in mind that a good fit

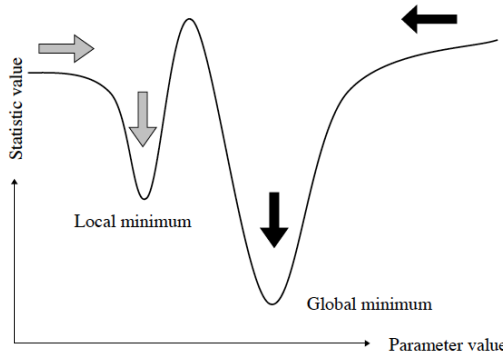


Figure 2.6 Biggest problem during fitting is getting trapped in local minima (Arnaud 2019).

does not necessarily mean the model is correct.

I mainly used XSPEC software (Arnaud 1996) and CIAO’s *Sherpa* for spectral fitting. Some of the XSPEC models can also be used in *Sherpa* which allows comparative analyses.

## 2.2.2 Spectral models

In this section, I will summarize the XSPEC models I used in my spectra fits. But first, how the models are used to form mathematical formulations? The X-ray spectrum of a source can be explained by more than one component:

$$Model = M_1 \times M_2 \times (A_1 + A_2 + M_3 \times A_3) + A_4 \quad (2.3)$$

where  $M_i(E)$  and  $A_i(E)$  are multiplicative and additive components. While the additive models produce energetically local modifications, the multiplicative models modify the overall model by a certain value.

### tbabs

The Tübingen-Boulder ISM absorption model is a multiplicative model that calculates the cross-section for X-ray absorption by the ISM as the sum of the cross-sections for different types of X-ray absorptions (i.e Gas, molecular, grains). This model makes use of different photo-electric absorption cross-sections via `xsect` command in the XSPEC. Eventough `phabs` is a popular model for absorption, the advantage of `tbabs` is the ability to use different ISM abundances. The shortcut `"abun [abundance name]"` allows for an easy ISM abundance update of your choosing. The ISM photo-electric absorption cross-section  $\sigma_{ISM}$  is calculated by:

$$\sigma_{ISM} = \sigma_{Grains} + \sigma_{Gas} + \sigma_{Molecules} \quad (2.4)$$

Then it is normalized to the hydrogen column density ( $N_H$ ). Finally observed spectrum takes the form:

$$I_{abs}(E) = e^{-\sigma_{ISM}(E)N_H} I_{Source}(E) \quad (2.5)$$

where  $N_H$  is in the units of  $10^{22} \text{ atoms cm}^{-2}$ . The  $N_H$  value is usually very high ( $N_H \sim 10^{22} - 10^{23}$ ) for the galactic sources. Another important thing to keep in mind is that the  $N_H$  values may change for some sources due to the dynamical environment they might have.

### **power-law**

This additive model is rather simple compared to other models. Power-law is a photon power-law defined as:

$$A(E) = K \left( \frac{E}{1 \text{keV}} \right)^{-\alpha} \quad (2.6)$$

where  $\alpha$  is the dimensionless photon index and K is the normalization (photons/keV/cm<sup>2</sup>/s) at 1 keV.

### **gaussian**

An excess emission around  $\sim 6.4$  keV is usually observed in X-rays binaries. This radiation arise from the ejection of K-shell electrons from the iron atoms in the corona. This Iron line emission is modelled with a simple Gaussian line profile:

$$A(E) = \frac{K}{\sqrt{2\pi\sigma^2}} e^{-0.5\left(\frac{E-E_L}{\sigma}\right)^2} \quad (2.7)$$

where  $E_L$  is the line energy in keV,  $\sigma$  is the line width in keV and K is the normalization (photons/cm<sup>2</sup>/s). A Gaussian profile can also represent a delta function if  $\sigma \leq 0$ . In my fits, I used 6.4 keV as  $E_L$  and started fitting with a  $\sigma \sim 0.5$  during my fits.  $\sigma$  can change due to different geometrical structure of the source environment and it's interpretation is beyond the scope of this thesis.



## 2.3 Timing Analysis

The main emphasis of this thesis is to find out how the DSHs affect the power spectral properties and the variability of the signals from GBHTs. In this section, I will summarize the mathematical representation of the Fourier techniques I used in my work. For a detailed description of Fourier techniques used in this thesis, please refer to van der Klis (1989).

### 2.3.1 The Discrete Fourier Transformation (DFT)

The X-ray variability of intensity of astronomical sources is usually characterized as a time series of  $N$  bins with count rates  $x_k$  ( $k=0, \dots, N-1$ ). Each bin correspond to an evenly spaced time bin with a length of  $\Delta t$ . The discrete Fourier transform  $X_j$  can be written in the frequency domain as:

$$X_j = \sum_{k=0}^{N-1} x_k e^{\frac{2\pi i j k}{N}} \quad (2.8)$$

where  $i = \sqrt{-1}$ . The independent frequencies are then obtained by:

$$f_j = \frac{j}{T} = \frac{j}{N\Delta t} \quad (2.9)$$

where  $T$  is the total duration of the light curve ( $T=N\Delta t$ ). The Fourier frequencies are defined in  $j \in [-\frac{N}{2}, +\frac{N}{2}]$  but the minimum frequency of a light curve or the maximum resolution you can obtain is  $j_{min} = 1$ , i.e  $f_{min} = \frac{1}{T}$ . The maximally accessible frequency, the ‘‘Nyquist Frequency’’, is given by the length of the time bins:  $j_{max} = \frac{N}{2}$  i.e  $f_{Nyq} = \frac{1}{2\Delta t}$ . At zero frequency Eq. 2.9 gives the total number of photons.

A complication is the existence of noise components (i.e Poisson noise, background) in the signal and has to be dealt with. Since it is possible to split the independent signal component  $S_k$  and the independent noise component  $n_k$ , this can also be applied to their discrete Fourier transforms:

$$X_j = S_j + N_j \quad (2.10)$$

where  $S_j$  and  $N_j$  are at frequency  $f_j$ .

### 2.3.2 The power spectral density (PSD)

The power spectral density is a fundamental tool used to interpret the complex properties of GBHTs. To find the PSD we start with a result known as Parseval’s theorem:

$$\sum_{k=0}^{N-1} |x_k|^2 = \frac{1}{N} \sum_{j=-N/2}^{N/2} |a_j|^2 \quad (2.11)$$

This implies that there is a relation between the summed squared modulus of the Fourier amplitudes and the total variance of the data:

$$\text{Var}(x_k) = \sum_k (x - \bar{x})^2 = \sum_k (x_k^2 - \frac{1}{N} (\sum_k x_k)^2) = \frac{1}{N} \sum_j |a_j|^2 - \frac{1}{N} a_0^2 \quad (2.12)$$

Finally we get:

$$\text{Var}(x_k) = \frac{1}{n} \sum_{-N/2}^{N/2-1} |a_j|^2 \quad (2.13)$$

Then the PSD is the squared magnitude of the complex Fourier transform:

$$P_j = X_j^* X_j = |X_j|^2 \quad (2.14)$$

The PSD is the manifestation of the variance of the light curve due to the variabilities characterized by the frequency  $f_j$ . If there exists a periodic variability in the source signal (e.g. a sinusoidal  $x_k = \sin(2\pi f + \star \Delta t)$ ), produce a  $\delta$ -peak at the corresponding frequency ( $f^*$ ) appears in the PSD.

The statistical uncertainty of a PSD is of the order of the PSD itself, and by averaging, it can be reduced by the square root of the averaged independent measurements. Another method is to rebinning the PSD and then averaging  $W$  consecutive frequency bins.

$$(\sigma) \langle P \rangle = \frac{\langle P \rangle}{\sqrt{M}} \quad (2.15)$$

where  $M$  is the number of equally split data segments,  $\langle P \rangle$  is the average over  $M$  number of independent measurements. Here  $M$  is the product of  $M_{seg}$  light curve segments and  $M_j$  Fourier frequencies used to obtain a given  $\langle P \rangle$  value:

$$M = M_{seg} \times M_j \quad (2.16)$$

## Normalization

There are several different normalizations of the PSD, each serving to different purposes. The normalized powers are found by multiplying the original PSD by a normalization factor:

$$\langle P_{norm} \rangle = A \langle P \rangle \quad (2.17)$$

Following this, here are some of the most commonly used normalizations,

$$A = \begin{cases} 1, & \text{unnormalized} \\ \frac{2}{TR}, & \text{for Leahy (1983) normalization} \\ \frac{2}{TR_{sig}R_{sig}}, & \text{for Miyamoto and Kitamoto (1989) normalization} \end{cases} \quad (2.18)$$

where  $T$  is the total duration of the observation,  $R = \langle x_k \rangle$  is the total time-averaged count rate and  $R_{sig}$  is the signal count rate.  $R_{sig}$  is obtained by subtraction of the background level of the light curve from the average count rate  $R$ .

$$R_{sig} = R - R_{bkg} \quad (2.19)$$

Notice that only the Miyamoto normalization takes the background into account. Leahy normalization delivers the light curve variance or the squared root mean square variability,  $rms^2$ , per frequency interval. Rewriting the Perseval's theorem in Eq. 2.12 we get:

$$rms^2 = \langle x_k^2 \rangle - \langle x_k \rangle^2 = \sum_k \frac{2}{T \langle x_k \rangle} \langle P \rangle \Delta f_j \quad (2.20)$$

This normalization yields a Poisson noise level of 2, independent of the source intensity. The advantage of ‘‘Miyamoto’’ normalization is that it provides better comparison of systematic brightness-independent similarities between different PSDs in terms of shape, fractional variance. While ‘‘Leahy’’ normalization is useful in understanding the effects of varying brightness when comparing different GBHs or different states of the same source.

It is important to point out that term ‘‘rms amplitude’’ or ‘‘rms variability’’ used in (Eq. 2.20) this work is often used in the sense of fractional variability, i.e. ( $rms/mean$ ).

### Statistical uncertainty of the PSD values

The noise powers  $P_{j,noise}$  follow the  $\chi^2$  distribution with 2 degrees of freedom. If the noise is Poisson distributed, the central limit theorem says that for ‘‘certain’’ conditions  $P_{j,noise}$  would approximately follow the Gaussian distribution therefore  $\chi^2$  property will still hold. The uncertainty of the noise-corrected PSD is van der Klis (1989):

$$\sigma\langle P \rangle = \frac{\langle P \rangle}{\sqrt{M}} = \frac{(\langle |S|^2 \rangle + \langle |N|^2 \rangle)}{\sqrt{M}} \quad (2.21)$$

The Leahy normalization of the Poisson noise is exactly given by the  $\chi^2$  distribution with 2 d.o.f. Then uncertainty of the Poisson noise is  $\sigma(|N_{poisson,j}|)^2 = \sqrt{\text{Var}(N_{poisson,j})} = \sqrt{4} = 2$ . So rebinning of the signal can help approximating a Gaussian distribution. It can be seen from the Eq. 2.21 this also applies to both the noise and the signal.

### Summary of Timing Analysis

In order to investigate the temporal properties of a signal, one has to obtain a light curve first. The time resolution, the energy selection and the binning of the light curve is up to the researcher and the purpose of the analysis. Then one can calculate the normalized power spectra via FFT. Most people use their own codes in their favourite coding language, though some instrument softwares offer timing tools in their packages. To decrease the errors the spectra has to be averaged. Finally, the power spectrum has to be modelled.

The PSDs of the GBHTs have historically been modelled by a broken power-law plus narrow Lorentzians to fit the QPOs (Nowak et al. 1999; Tomsick and Kaaret 2000). But, recent studies successfully modelled PSDs of the XBs only using broad and narrow Lorentzians (van Straaten et al. 2002; Pottschmidt et al. 2003; Belloni et al. 2002).

In this thesis, I used Lorentzians to model my PSDs so that it would allow me to compare the fits to the recent works.

The Lorentzians are of the form:

$$L_i(f) = \frac{R_i^2 \Delta_i}{2\pi[(f - f_i)^2 + (\frac{1}{2}\Delta_i)^2]} \quad (2.22)$$

where the subscript i corresponds to each Lorentzian used in the fit,  $R_i$  is the rms amplitude of the Lorentzian when integrated over infinity,  $\Delta_i$  is the FWHM and  $f_i$  is the resonance frequency. The frequency at which the total rms variability contribution is maximum is called the peak frequency:

$$v_i = f_i \left( \frac{\Delta_i^2}{4f_i^2} + 1 \right)^{\frac{1}{2}} \quad (2.23)$$

An example of PSDs fitted with Lorentzians can be seen in Figure 2.7. The broad Lorentzians have the lowest frequency in the fit  $L_i$  with  $i=1$ .

The rms amplitude of the Lorentzian in the frequency band  $(0, \infty)$  is given by:

$$rms_i = R_i \left( \frac{1}{2} - \frac{\tan^{-1}(-2Q_i)}{\pi} \right) \quad (2.24)$$

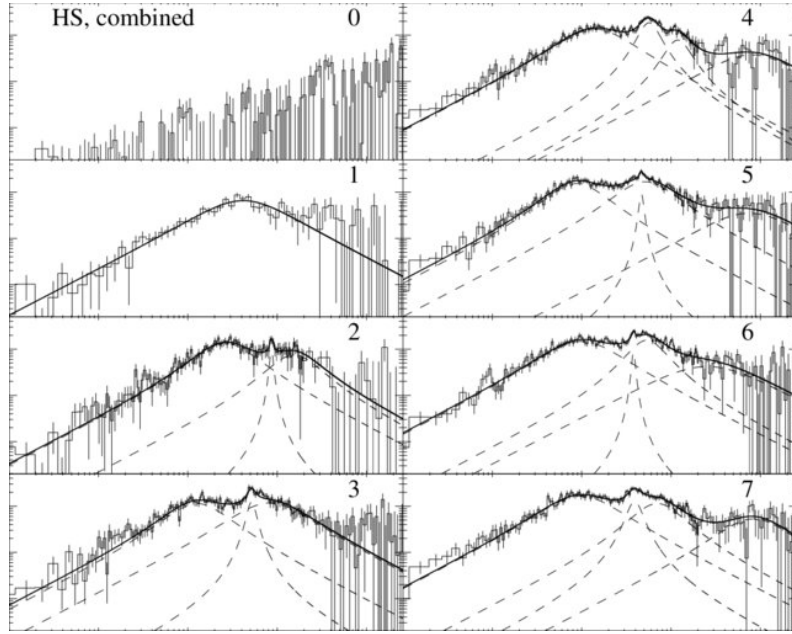


Figure 2.7 Several PSDs of XTE J1650–500 during it’s outburst decay are fitted with Lorentzians (adopted from Kalemci et al. (2003)).

In this work I used Leahy normalization to investigate the Poisson levels and the Miyamoto normalization is used to study the PSDs and rms variability. That’s why, in the following sections the rms amplitude will refer to the area of the Lorentzians (i.e. integrated power spectrum).

# Chapter 3

## X-ray observations of 1E 1740.7–2742 and data analysis

### 3.1 Introduction

In this chapter, I outline the spectral and temporal analysis of data accumulated from the observations of 1E 1740.7–2742. Other sections focus on data reduction, spectral and temporal methods used for the analyses and instrumental calibration issues. The emphasis of this thesis is on timing information but spectral information is crucial to realise the physical interpretations of the timing information.

There exists many global correlations between the spectral and temporal properties of GBHs. The rms amplitude and the photon index ( $\Gamma$ ) correlation is one of these (Figure 3.1). However, there are some outliers (4U 1630-47 and XTE J1748-488) those also have high hydrogen absorption column densities ( $N_H > 7 \times 10^{22} \text{ cm}^{-2}$ ). It is known that sources that have high absorption column density also have high dust column density in their LOS. The hydrogen column density and dust scattering are related to each other as:  $\tau_{sca} = 0.49 \times (N_H/10^{22} \text{ cm}^{-2}) \times (E/\text{keV})^{-2}$  (Predehl and Schmitt 1995). Then, sources that have high  $N_H$  are behind ample amount of dust which causes the X-rays to scatter in small angles. The scattering cross section is related to the X-ray photon energy  $E$  as  $\sim E^{-2}$ . This shows that the small angle scattering can be very intense at low energies. The reduced rms of the “outliers” at low energies may also be explained by the presence of a dust scattering halo. If the halo is completely in the field-of-view (FOV) of the instrument, the scattered X-rays would be lagged due to the scattering geometry and therefore may decrease the coherence. As a result of this the rms amplitude of variability would drop.

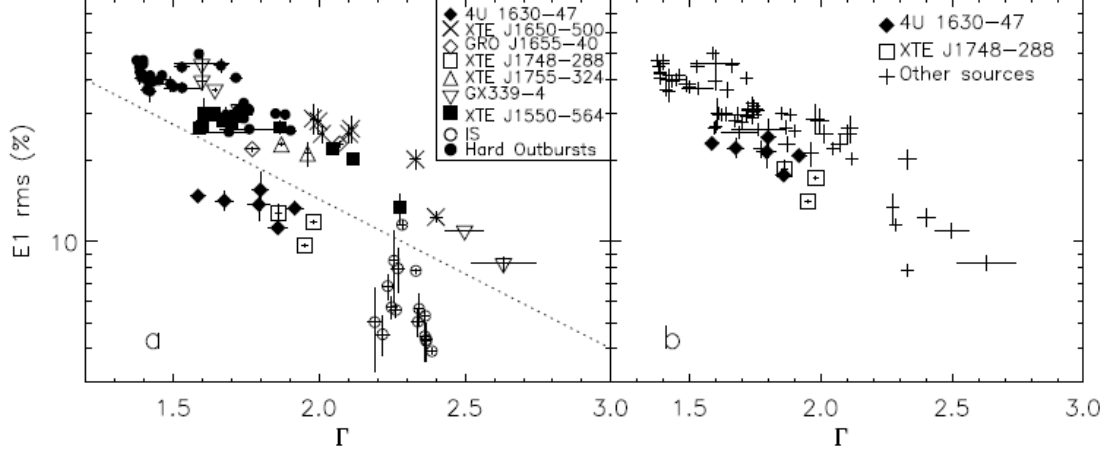


Figure 3.1 (a) The correlation between rms amplitude and the spectral index in 2-6 keV. (b) The correlation between rms amplitude and the spectral index in 6-15 keV. (adopted from Kalemci (2002))

In order to quantify the effects of DSH on timing properties of GBHTs, on MJD 53645 we have observed 1E 1740.7–2742 using *XMM-Newton* (ObsID: 0303210201) and *Rossi X-ray Timing Explorer* (ObsID:91112-09-01-00) simultaneously. For *EPIC-PN* we used "Small window mode", and "Timing mode" for *EPIC-MOS*. We used XMM-SAS and custom IDL codes for data reduction.

1E1740.7-2942 was chosen due to it's three main features: 1. It has very high  $N_H \approx 1.2 \times 10^{23} \text{ cm}^{-2}$  (Kalemci et al. 2006), 2. spends most of it's time in the hard state, 3. shows extended emission features (Cui et al. 2001). Having a high enough count rate enables us to avoid pile-up effects in EPIC PN and to perform timing analysis with EPIC MOS. The disadvantages of 1E 1740.7–2742 are; having a strong X-ray source nearby (SWIFT J174444.9-295042) which requires offset pointing and the Ridge emission from the Galactic center (GC) plane. *XMM-Newton* image of the source can be seen in Fig. 3.2

Finally, the pipeline and other codes used for this research are published in a Github repository. The following sections make use of the codes in this repository extensively and will be referred many times.

Link to the repository: [https://github.com/OzanToyran/dsh\\_xmm\\_lib](https://github.com/OzanToyran/dsh_xmm_lib)

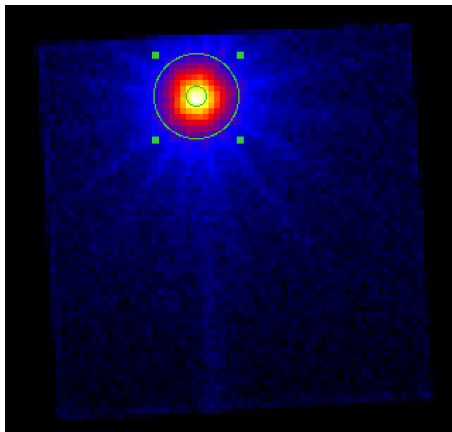


Figure 3.2 *XMM-Newton* EPIC-PN image of 1E 1740.7–2742. Green circles are at 5'' and 30''.

## 3.2 Observations and data analysis

### 3.2.1 *XMM-Newton* point source analysis

#### 3.2.1.1 *XMM-Newton EPIC-PN*

We analyzed the *XMM-Newton* observation using the XMM-SAS tools and custom IDL codes. We first created a 16s binned EPIC-PN light curve to check the state of the observation. This light curve revealed a flare ( $\sim 3$  ks) in the middle of the observation (Fig. 3.3) and had to be cropped. The remaining data is about  $\sim 20$  ks. We have used different extraction areas for the source light curves: 15'', 20'', 25'', 30'', 40'', 60'' and 100''. We extracted light curves from these areas with 1/32s and 1/128 s time resolutions to be used in timing analysis. The background was extracted from a source-free and DSH-free area. And then, the energy spectra were produced between 0.2 – 12 keV energy bands from the same areas. The spectra were then fitted with *absorption*  $\times$  *power-law* models using XSPEC. Ancillary response matrices and redistribution matrices are created using *arfgen* and *rmfgen* procedures of XMM-SAS.

We then checked if pile-up existed in *EPIC-PN* observation before implementing our theory. Details about pile-up and the analysis we followed will be discussed in the next section. The products gathered have been corrected for Out-of-time (Oot) events which is 1.1% of all events for *EPIC-PN* small window mode using FTOOLS.

#### **Pile-up**

The pile-up occurs when more than 1 photon arrive at the same pixel on the CCD during the same read-out cycle. This causes artificial energies in the spectrum. To check whether the pile-up exists in our observation, we used the *epatplot* procedure of XMM-SAS. According to the procedure guide, if singles (the ratio of singles to doubles) are less than 1.0 and doubles



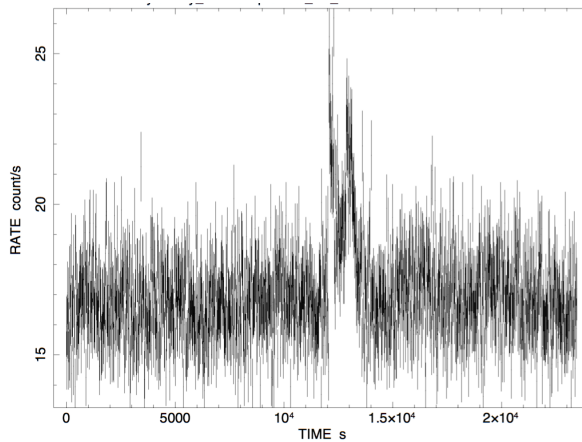


Figure 3.3 Lightcurve with 16s resolution. Flare in the middle that comes from background is discarded

Table 3.1 Results for *epatplot* procedure

	2-6 keV	0.2-2 keV
Single photons	$1.024 \pm 0.04$	$1.004 \pm 0.039$
Double photons	$0.967 \pm 0.05$	$0.992 \pm 0.052$

are greater than 1.0 then pile-up exists. With this remark, it can be seen from Table 3.1 that there is a possibility for pile-up. Even though results are not exactly outside these limits, the errors high enough to prove otherwise.

In order to clarify the doubt, we checked energy spectra extracted with and without the central pixels (Fig. 3.4). Removing first 5" and 7" radius areas (excluding the central 4 pixels) allowed us to see if the pile-up exists. Comparing different data sets showed that central removed spectra soften (Table 3.2). Data 1,2,3,4 are taken from PN 0"-30", PN 5"-30", PN 7"-30" and MOS2 data, respectively. Data 2 and Data 3 shows a slight change in photon index compared to Data 1 and consistent with Data 4. According to this there may be pile-up in high energies yet differences are not present within  $1 \sigma$  level. We decided not to exclude the central pixels since it would cost us many precious photons and it only seems effective at high energies.

Table 3.2 Data 1: 0" – 30", Data 2: 5" – 30", Data 3: 7" – 30" , Data 4: 1 – 10 keV

Spectrum	$N_H$	$\Gamma$ (Pho. Index)	Norm.	Rate
Data 1: PN	$1.95 \times 10^{23}$	$1.62 \pm 0.005$	$0.10 \pm 0.001$	16.46
Data 2: PN	$1.95 \times 10^{23}$	$1.69 \pm 0.007$	$0.11 \pm 0.001$	11.06
Data 3: PN	$1.95 \times 10^{23}$	$1.77 \pm 0.008$	$0.13 \pm 0.002$	7.96
Data 4: MOS2	$1.95 \times 10^{23}$	$1.76 \pm 0.013$	$0.11 \pm 0.001$	3.47

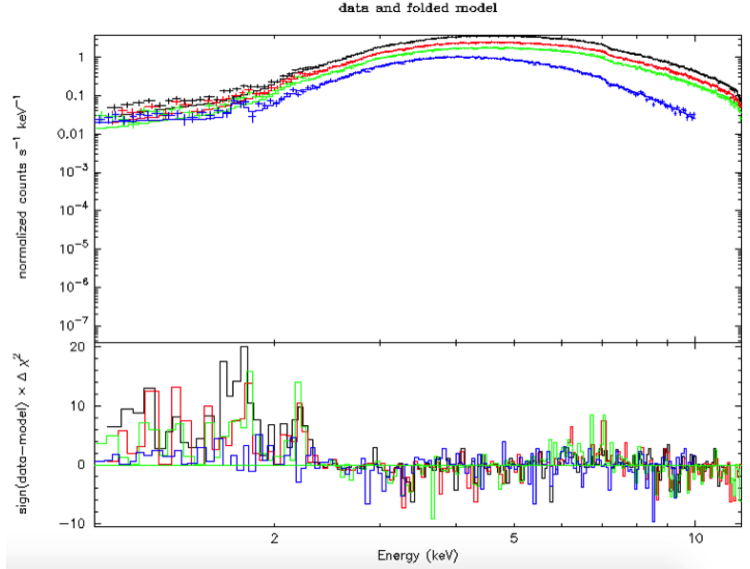


Figure 3.4 Modeled Energy Spectrums; *Black*: PN 0'' – 30'', *Red*: PN 5'' – 30'', *Green*: PN 7'' – 30'', *Blue*: MOS2

### 3.2.1.2 XMM-Newton EPIC-MOS

We used *EPIC-MOS* observation that was taken in “timing” mode as an additional way to calculate the variability in the signal. We created images of MOS1 and MOS2 observations (Figure 3.5). MOS 1 image indicated a systematic error which caused data losses. After consulting with XMM-Newton *Helpdesk* the problem was associated with the MOS 1 instrument going into counting mode. We discarded MOS 1 data but MOS 2 data seemed intact. Due to the nature of “Timing mode” light curves were extracted from  $\pm 3, \pm 4, \pm 5$  and  $\pm 10$  pixels wide rectangles from the central pixel. Light curves with 1/32 s and 1/128 s resolutions were extracted between 2.11-5.86 keV energy band. We extracted the energy spectra from the same regions only to compare with EPIC-PN spectra results. Note that the MOS spectrum results are not used in this work since the energy calibration of MOS detectors are not good enough for spectral analysis and it is better not used unless you know what you are doing.

### 3.2.1.3 Surface Brightness Profile

As mentioned in section 1.4.1, scientists show the presence of a DSH by showing the intensity that can extend up to arcmin scales. We implemented the following steps to create the surface brightness profile (SBP) using XMM-SAS procedures and custom IDL codes:

- Obtain the exposure map using XMM-SAS’s *exppmap* procedure.
- Check if any serendipitous sources are present. If so remove those circular areas.

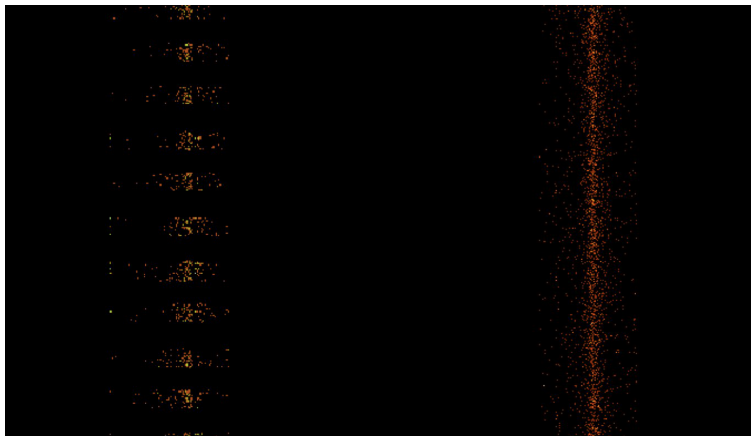


Figure 3.5 Images from the EPIC-MOS1 (left) and EPIC-MOS2 (right) detectors.

- Also exclude pile-up (if present) and Oot events.
- Calculate the areas of each annulus with equal radius steps (eg.  $0''$ - $10''$ ,  $10''$ - $20''$ ,...)
- Calculate the total counts in each annulus.
- Divide the counts by corresponding area to obtain  $count/arcsec^2$  values.
- Apply background correction if it is significant.
- Obtain the 1D PSF with a *King* profile using XMM-SAS's *eradial* procedure.
- Normalize the PSFs in a way that initial intervals of the obtained PSF by *eradial*, and the computed PSF by the counts per area, would have the same  $cts/area$  value.
- Normalize the PSF with the maxima of the computed PSF.

### 3.2.2 RXTE point source analysis

The *Rossi X-ray Timing Explorer* observation on MJD 52645 with ObsID 91112-09-01-00 was offset due to reasons mentioned in previous sections. We used the data from the PCA instrument to extract the light curve and the energy spectra. We created the light curve from the PCA instrument with a time resolution of 128s per bin. The energy spectrum was extracted in the 3-25 keV energy band. We created the response matrix and the background files using the standard FTOOLS programs. We have produced new response matrices for the offset source observation, using real coordinates of 1E 1740.7–2742 to determine the effect of the offsetting. For timing analysis, we followed the steps that will be mentioned in section 3.2.4.

Also, the "Galactic Ridge" emission that have soft spectra, makes a contribution to the collected photons in the PCA instrument that cannot be modeled by the standard background models. Thus, *Rossi X-ray Timing Explorer* observations towards the Galactic Bulge are heavily affected by this emission. This contribution is independent of source radiation and consequently reduces the observed RMS/Mean value. To determine the Galactic ridge contribution we used the archival *Rossi X-ray Timing Explorer* background observation for 1E 1740.7–2742 (ObsID 40097-07-02-00) that does not include the source (Ridge Data hereafter). We used *power-law+gaussian* to model the Ridge emission. The Gaussian iron line emission energy was fixed at 6.4 keV. We used this model as an additional component representing the Galactic Ridge contribution while modelling the source observation. We also added %1 systematic uncertainty to both *Rossi X-ray Timing Explorer* data before the analysis.

### 3.2.3 *Chandra* point source analysis

We analyzed the *Chandra* observation by Gallo & Fender 2002 with the ObsID 658 to compare our spectral results. This observation was taken on MJD 51786 and lasted about  $\sim 10$  ks. We used CIAO (version 4.11) for the data reduction and *XSPEC* and *Sherpa* along with custom IDL codes to analyze the data. The source was nearly on the aim-point of the telescope that is on ACIS-I3. The image of 1E 1740.7–2742 shows heavy pile-up effects in the central pixels (Figure 3.6). We excluded the piled-up central region that is a circle with a radius of 4 pixels for spectral analysis. We extracted an energy spectrum from a 4"–30" circle centered at the source in the 2–10 keV energy band. It was modelled with  $\text{tbabs} \times \text{power-law}$  and fit parameters are frozen at the values taken from EPIC-PN spectrum fit.

### 3.2.4 Timing Analysis

Tübingen timing tools' IDL codes were modified for XMM-Newton data to obtain the PSDs and compare the *XMM-Newton* spectra with the RXTE power spectrum. The codes were ordered for pipeline analysis. The pipeline procedure consists of;

1. Obtain the Leahy normalized power spectra.
2. The Poisson level measured above  $v_{Nyq}/2$  was subtracted from the Leahy normalized power spectrum. This also prevents the chances of introducing aliased powers in the average power spectrum.
3. Remaining powers are divided by photons per second. Thus, found the Miyamoto normalization.

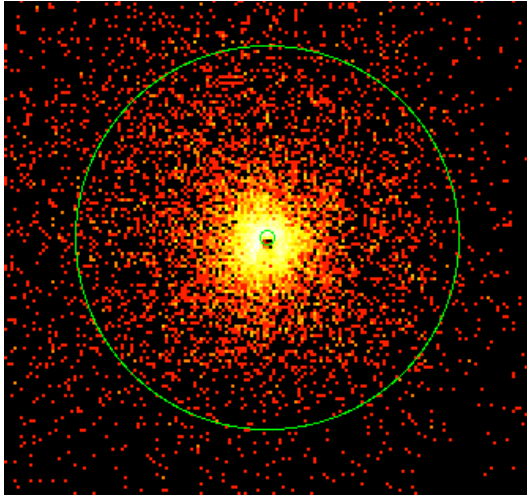


Figure 3.6 Image of 1E 1740.7–2742 from the Chandra instrument.

4. Miyamoto normalized spectra are fitted with Lorentzians and eventually Peak frequency and rms amplitude values are calculated.

For EPIC-PN (PN hereafter) we used 32s and 128s segments and for EPIC-MOS2 (MOS2 hereafter) again 32s and 128s segments were used to produce the light curves. Due to low photon counts in both PN and MOS2 the errors are usually exaggerated in PSDs.

#### 3.2.4.1 Dead-time

In order to find the effect of dead-time on power spectrum a wide frequency range power spectrum was created (0-128 Hz). Significant powers are unlikely above a few 10 Hz therefore, in a *Leahy* normalized spectrum high frequency range is expected to be a 2.0 continuum (Leahy 1983). To determine the dead-time, power spectra from each annuli with varying radii were extracted. Then, the high frequency parts were averaged using an IDL code to obtain the dead-time level.

# Chapter 4

## Results

### 4.1 1E 1740.7–2742 light curves and the source history

We obtained high resolution ( $2^{-5}$  s) light curves of *XMM-Newton* and RXTE to be used in investigating the effect of DSH to the variability properties of GBHTs. The extraction area for PN light curve is  $0''$ - $30''$ . The RXTE light curve has a time resolution of  $2^{-7}$ s. The *Chandra* light curve is extracted from an area of  $5''$ - $30''$  arc seconds with 100s time resolution. The light curves from these three instruments can be seen in Figures ( 4.1, 4.2, 4.3).

Using the archival *Rossi X-ray Timing Explorer* data we created a 2 month brightness history of the 1E 1740.7–2742 (Smith et al. 2002). *Rossi X-ray Timing Explorer* PCA observations are taken between 53617 - 53673 MJD. *XMM-Newton* observation lies in the middle since it was taken on 53645 MJD. We extracted the energy spectra of 14 PCA observations and fitted the with a model of *tbabs x (power-law + gaussian)* in the 3-25 keV energy band. The evolution of the unabsorbed source flux over 2 months can be seen in Figure 4.4. It can be seen from the figure that the source does not show dramatic changes and exhibits a persistent emission throughout the 2 months period.

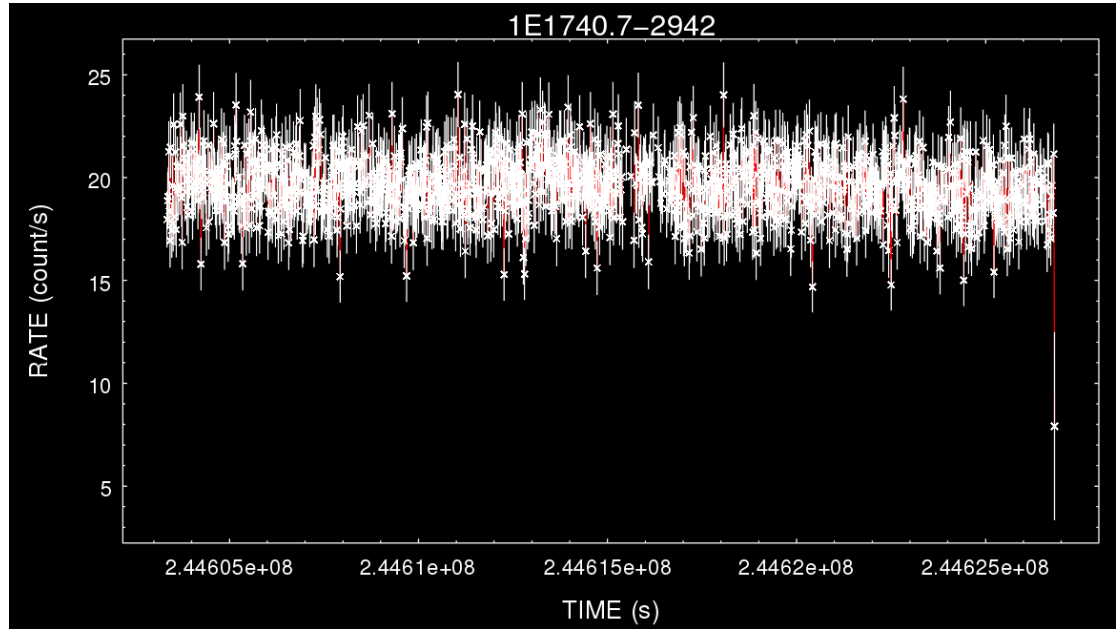


Figure 4.1 The rebinned light curve from the XMM-Newton's EPIC-PN instrument

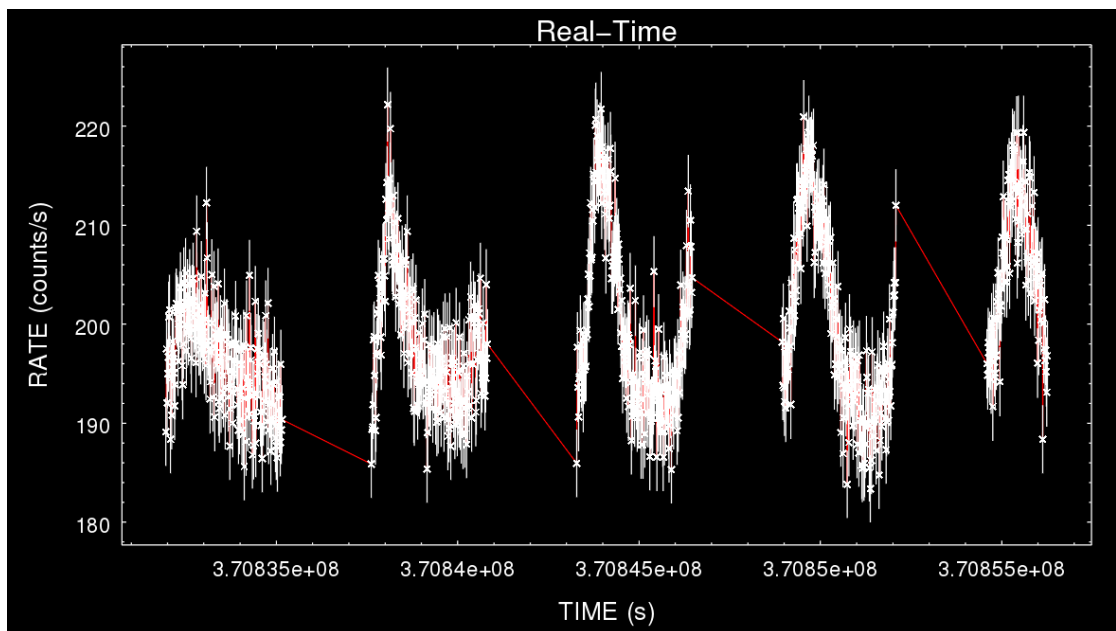


Figure 4.2 The rebinned light curve from the RXTE instrument

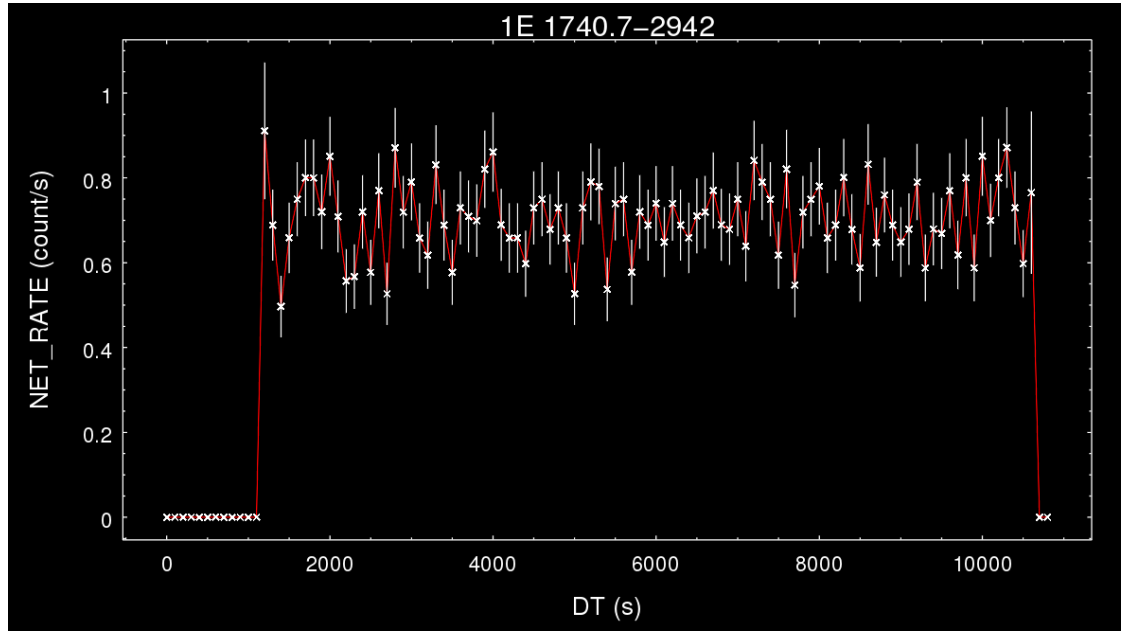


Figure 4.3 The rebinned light curve from the Chandra instrument

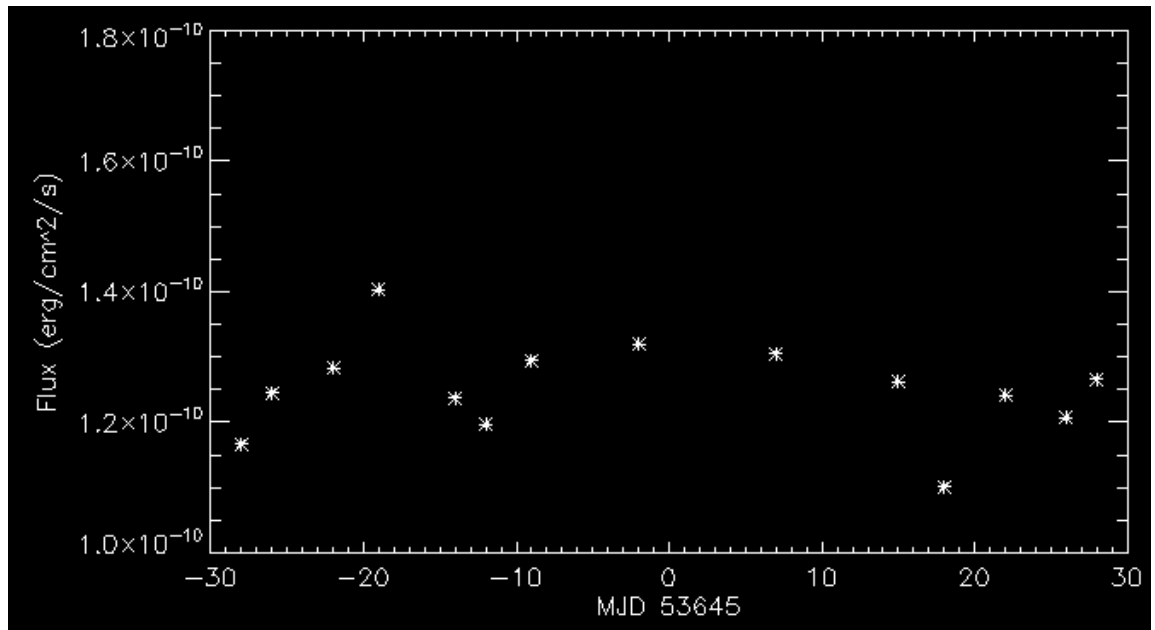


Figure 4.4 RXTE flux evolution of 1E 1740.7-2742 during 2 months period.



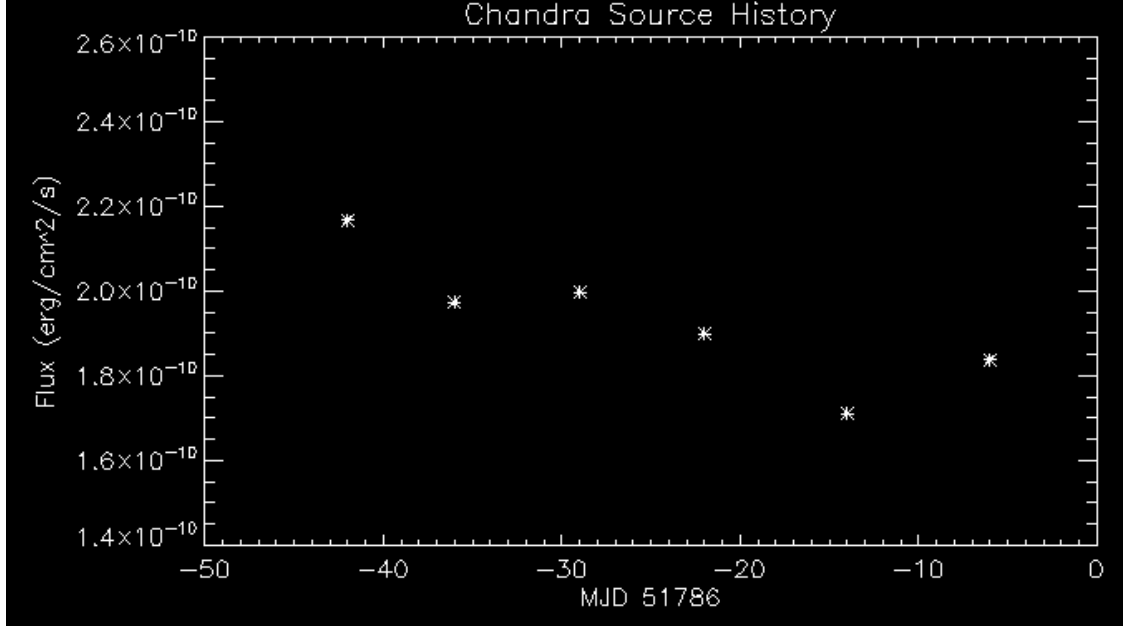


Figure 4.5 *Chandra* flux evolution of 1E 1740.7–2742 during  $\sim 2$  months period. Note that the Modified Julian Date is earlier than that of *XMM-Newton* and *RXTE* observations.

## 4.2 The Energy spectra

We first extracted the energy spectrum of 1E 1740.7–2742 from *XMM-Newton* to determine the state of our source. The spectrum was modelled with  $\text{tbabs} \times \text{power-law}$  with ISM abundances of Wilms, Allen & McCray (2000) and cross sections of Verner et al. 1996. In the initial runs, we let the  $N_H$  and  $\Gamma$  parameters to be free in the 2–10 keV energy band. The resulting values for  $N_H$  varied between  $18\text{--}20 \times 10^{22} \text{ cm}^{-2}$  and for the spectral index  $\Gamma = 1.5\text{--}1.65$ . Then created the confidence contours of  $N_H$  and  $\Gamma$  values (Figure 4.6). Finally, We obtained the best-fit values for  $N_H$  as  $19.14 \times 10^{22} \pm 0.12 \text{ cm}^{-2}$  and  $\Gamma$  as  $1.58 \pm 0.01$ . These values give a reduced  $\chi^2$  of 1.2. The unabsorbed flux in the 2–10 keV is  $2.3 \times 10^{-10} \text{ erg/cm}^{-2}/\text{s}$ .

For MOS2 we used a region of 20 pixels wide rectangle. Using the same model and leaving the parameters free yielded a  $N_H$  value of  $19.4 \pm 0.3$  and  $\Gamma = 1.72 \pm 0.03$  with a reduced  $\chi^2 = 1.08$ . While the MOS2 spectrum gives a similar  $N_H$  value, the spectral index is a little bit softer but still hard. MAIN et al. (1999) observed the 1E 1740.7–2742 for a long period of time (17 observations in 1000 days) and reported that its photon index varies between 1.4 and 1.8. Overall, the *XMM-Newton* observations shows that the source is in the hard state and behind ample amount of dust. However, it is important to note that MOS2 spectra should not be used as a spectral diagnostic tool due to its energy calibration issues.

The *Chandra* ACIS-I spectrum was also extracted to compare with the *XMM-Newton* results. The energy spectrum was extracted from a  $4''\text{--}30''$  annulus due to heavy piling-up

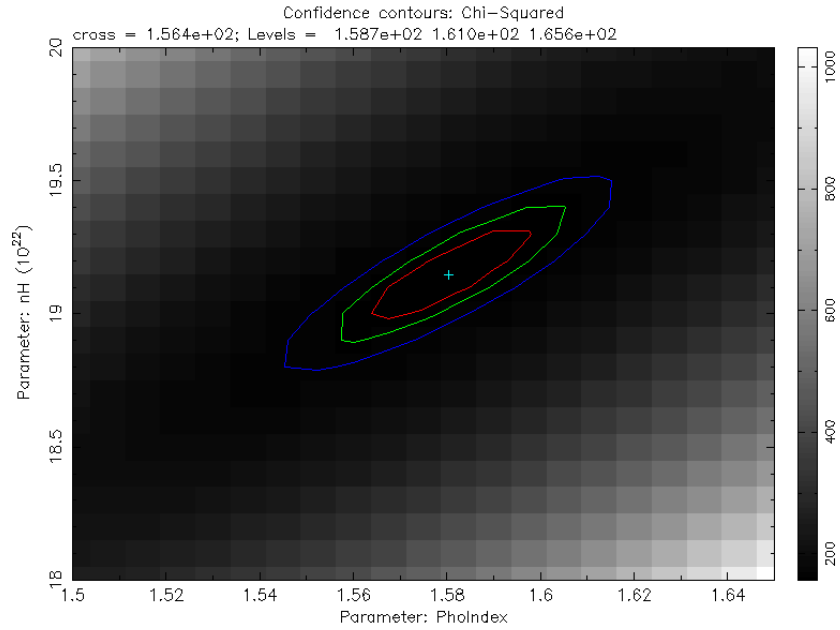


Figure 4.6 The confidence contours for 0''-30'' EPIC-PN spectrum  $N_H$  and  $\Gamma$  values for 72.58, 74.89 and 79.49 confidence levels.

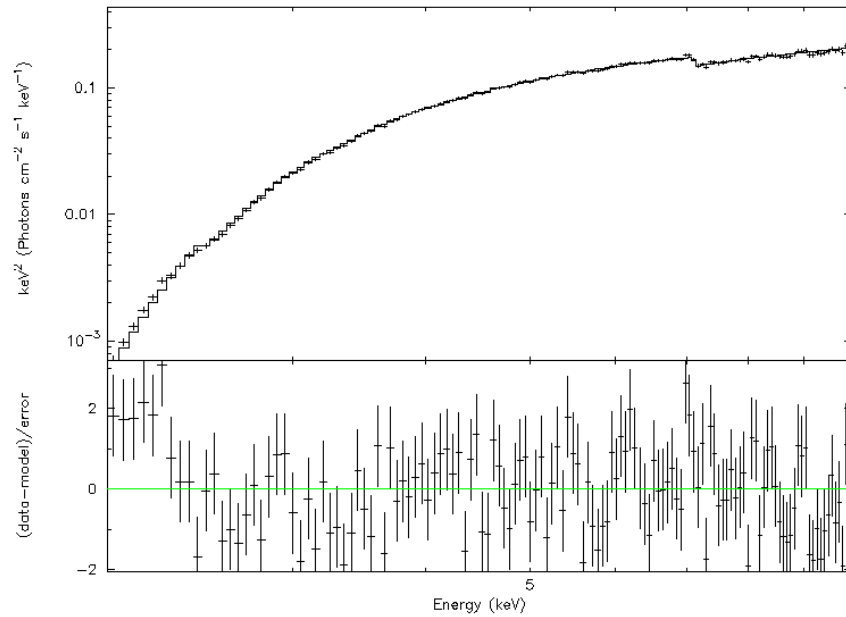


Figure 4.7 EPIC-PN energy spectrum modelled with  $\text{tbabs} \times \text{power-law}$  in 2.11 – 5.86 keV energy band.

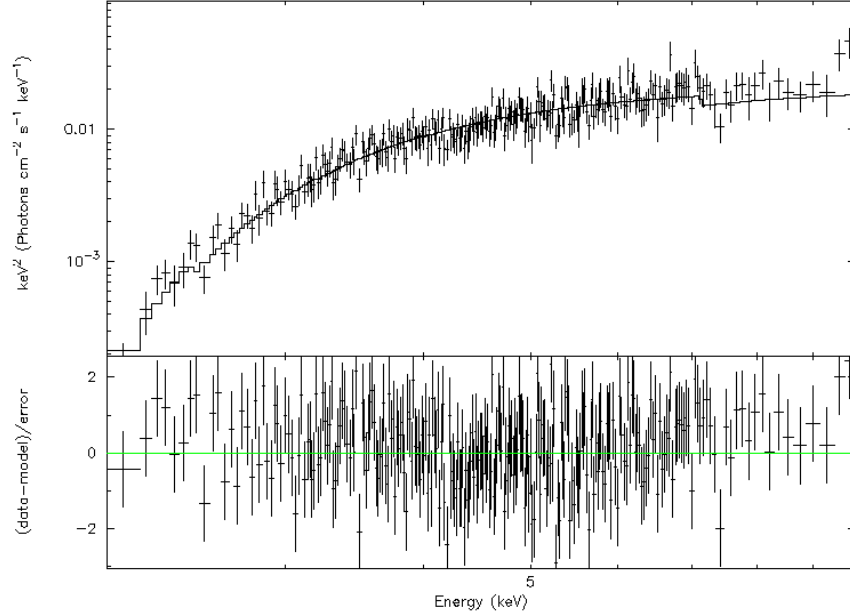


Figure 4.8 *Chandra* ACIS-I3 energy spectrum modelled with *tbabs*  $\times$  power-law in 2 – 10 keV energy band.

of the central pixels. The spectrum is fitted with a *tbabs*  $\times$  power-law model with again using the ISM abundances of Wilms et al. (2000) and cross sections of Verner et al. (1996). Fixing the  $N_H$  value to the value obtained from PN ( $19.14 \times 10^{22}$ ) yields a spectral index of  $\Gamma = 1.99 \pm 0.086$  with a reduced  $\chi^2 = 1.01$ . The unabsorbed flux between 2 -10 keV is  $2.5 \times 10^{-11} \text{ ergs/cm}^2/\text{s}$ . It's fitted spectrum can be seen in Figure 4.8.

### 4.3 Determination of the dead-time level for PSDs

In order to determine the rms amplitude of variability for simultaneous *XMM-Newton* and RXTE observations, we first calculated the dead-time levels for light curves extracted from different areas. After obtaining the high time resolution ( $2^{-5} \text{ s}$  &  $2^{-7} \text{ s}$ ) light curves, we investigated the dead-time effects. We obtained the Leahy normalized average PSD powers in 5-127 Hz and 20-127 Hz ranges. To determine the best extraction area we compared different areas of extraction for both EPIC-PN and EPIC-MOS2.

The high frequency part of the averaged Leahy normalized spectrum is expected to be a continuum at the value 2 (Leahy 1983). Consequently, the dead-time effect was calculated to be around for PN %1. Since MOS2 was in “Timing mode”, the dead-time effect should be less than PN’s. The Poisson levels found can be seen in Table 4.1 for PN and Table 4.2 for MOS2.

Table 4.1 Measured PN Poisson levels with different frequency bands

Area	Average Powers	
	5 – 127 Hz	20 – 127 Hz
15 arcsec	$1.985 \pm 0.002$	$1.985 \pm 0.002$
20 arcsec	$1.986 \pm 0.002$	$1.988 \pm 0.002$
25 arcsec	$1.987 \pm 0.002$	$1.989 \pm 0.002$
30 arcsec	$1.988 \pm 0.002$	$1.990 \pm 0.002$
40 arcsec	$1.990 \pm 0.002$	$1.991 \pm 0.002$
60 arcsec	$1.991 \pm 0.002$	$1.993 \pm 0.002$
100 arcsec	$1.992 \pm 0.002$	$1.993 \pm 0.002$

Table 4.2 Measured MOS2 Poisson levels with different frequency bands.

Area	Average Powers	
	5 – 127 Hz	20 – 127 Hz
$\pm 3$ pixels	$1.995 \pm 0.004$	$2.341 \pm 0.173$
$\pm 4$ pixels	$1.996 \pm 0.004$	$2.268 \pm 0.168$
$\pm 5$ pixels	$1.998 \pm 0.004$	$2.381 \pm 0.176$
$\pm 10$ pixels	$1.996 \pm 0.004$	$2.309 \pm 0.171$
$\pm 15$ pixels	$1.998 \pm 0.003$	$2.173 \pm 0.161$
$\pm 20$ pixels	$2.000 \pm 0.003$	$2.150 \pm 0.159$
$\pm 30$ pixels	$2.001 \pm 0.003$	$2.111 \pm 0.156$

## 4.4 Evidence of DSH effects on timing properties?

The main goal of this thesis is to investigate the effects of DSH on timing properties of GBHTs. First, we obtained the Miyamoto normalized power spectra of the *XMM-Newton* and *Rossi X-ray Timing Explorer* following the steps discussed in section 3.2.4 to determine the timing properties of our observations. For EPIC-PN, we again checked different areas (Figure 4.3). Using the  $2^{-5}s$  light curve of EPIC-PN in 2.115.86 keV energy band, we fitted the PSD with Lorentzians (Figure 4.9). The rms amplitude, the peak frequency and the count rate for EPIC-PN obtained from 0"-30" are  $15.98 \pm 2.76$ ,  $0.95 \pm 0.30$  Hz and  $9.7 \text{ cnt s}^{-1}$ , respectively.

The EPIC-MOS2 power spectra are fitted in a similar fashion (Figure 4.4) and the one extracted from  $\pm 30$  pixels from the central pixel decided to be used. The rms amplitude and the peak frequency of the the MOS2 power spectrum is  $19.35\% \pm 2.21$ ,  $1.12 \pm 0.36$  Hz, respectively. The fitted spectrum with Lorentzians can be seen in Figure 4.10. Due to low photon statistics the errors are exaggerated.

Finally, the power spectrum of the *Rossi X-ray Timing Explorer* observation was obtained. We used 131072 time bins per data segment while creating the RXTE PSD. Fitting of this spectrum yielded a rms amplitude of variability of  $9.9 \pm 2.5 \%$  with a peak frequency of

Area	RMS	Peak Frequency	Rate
15 arcsec	$14.60 \pm 2.30$	$0.97 \pm 0.28$	7.76
20 arcsec	$14.01 \pm 2.26$	$0.88 \pm 0.29$	8.65
25 arcsec	$15.22 \pm 2.24$	$0.83 \pm 0.38$	9.25
30 arcsec	$15.98 \pm 2.76$	$0.95 \pm 0.30$	9.70
40 arcsec	$15.88 \pm 2.05$	$0.96 \pm 0.29$	10.47
60 arcsec	$15.82 \pm 2.33$	$1.01 \pm 0.36$	10.99
100 arcsec	$15.95 \pm 2.70$	$1.03 \pm 0.39$	11.70

Table 4.3 EPIC PN power spectra fit results with average count rates in 2.11-5.86 keV energy band

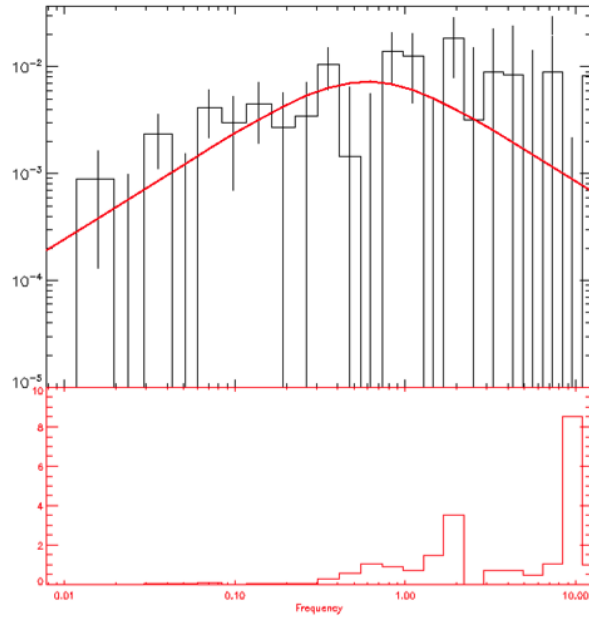


Figure 4.9 EPIC-PN power spectrum modelled with Lorentzians

Table 4.4 EPIC-MOS2 power spectra and average count rates in 2.11-5.86 keV energy range.

Area	RMS	Peak Frequency	Rate
$\pm 5$ pixels	$17.20 \pm 3.91$	$0.98 \pm 0.38$	2.66
$\pm 10$ pixels	$18.03 \pm 4.47$	$0.86 \pm 0.51$	3.43
$\pm 15$ pixels	$20.69 \pm 2.39$	$1.31 \pm 0.43$	3.66
$\pm 20$ pixels	$17.41 \pm 3.16$	$0.78 \pm 0.34$	3.71
$\pm 30$ pixels	$19.35 \pm 2.21$	$1.12 \pm 0.36$	3.64

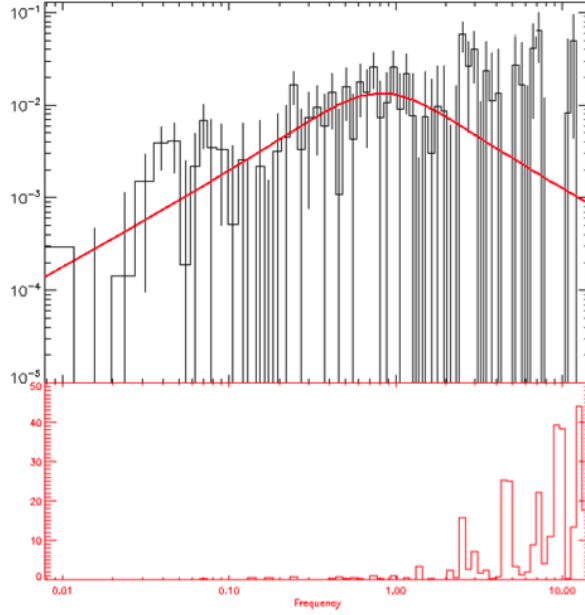


Figure 4.10 EPIC-MOS2 power spectrum modelled with Lorentzians.

$2.0 \pm 0.7$  Hz. Its power spectrum fitted with a Lorentzian can be seen in Figure 4.11.

These values of variability with  $\sim 16\%$  for PN,  $\sim 19\%$  for MOS2 and an even lower value of  $\sim 10\%$  for RXTE are well below the typical rms values of  $\sim 30 - 40\%$  of GBHTs in the hard state. For a uniform distribution of grains in the line of sight, the delay would be on the order of days (Molnar and Mauche 1986). Since the dominant variability of timescales are between ms to days, the scattered X-rays would not change the shape of the spectrum but would decrease the rms amplitude. Since the entire halo should be in the FOV of RXTE the effects of dust scattering may be the main reason for decreased rms amplitudes.

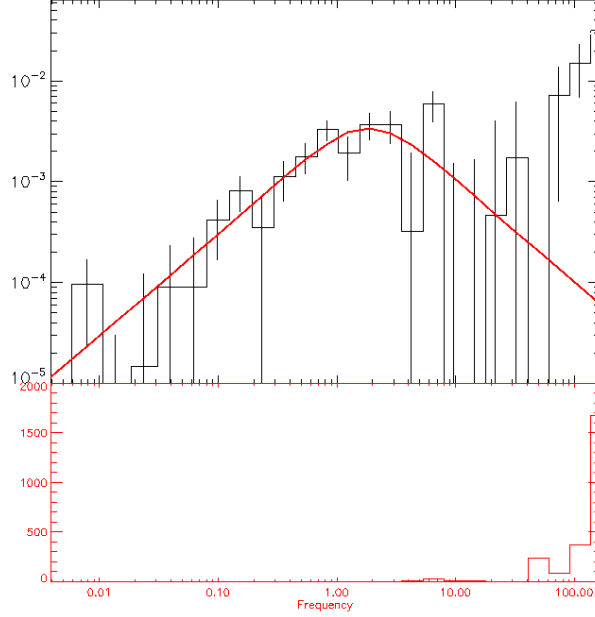


Figure 4.11 RXTE power spectrum modelled with Lorentzians.

## 4.5 Connection to the molecular clouds

1E 1740.7–2742 exhibits three main observational characteristics; 1) it is observed to form jets, 2) it shows persistent emission and 3) exhibits strong variability in its hard state. These phenomenological properties can be explained if the source is inside a dense molecular cloud Mirabel et al. (1992). A dense and cold molecular cloud can fuel the 1E 1740.7–2742 by Bondi-Hoyle accretion mechanism. Bally and Leventhal (1991) and Mirabel et al. (1991) found molecular clouds with  $V_{LSR} = -140 \text{ km s}^{-1}$  and  $V_{LSR} = -130 \text{ km s}^{-1}$  respectively, in the direction of 1E 1740.7–2742.

In order to investigate these phenomena observed from 1E 1740.7–2742 and its link to the molecular clouds in the Galactic Center (GC) we used the  $HCO^+$  molecular cloud catalog by M.A. Miville-Deschénes which can be found in the VizieR archives. This catalog contains about  $\sim 8000$  different molecular clouds in the GC and their parameters such as velocity and positions of them in our LOS.

We searched for the molecular clouds with  $140 \pm 20 \text{ km s}^{-1}$  in the direction of 1E 1740.7–2742. We found that the source lies on top of a molecular cloud with radial velocity  $V = -152.4 \text{ km.s}^{-1}$  in the LOS. The position of 1E 1740.7–2742 with the nearby molecular clouds in the LOS can be seen in Figure 4.12. The distance of this cloud is found to be 8.6 kpc by Miville-Deschénes while the distance of 1E 1740.7–2742 is thought to be  $\sim 8.5$  kpc. However, we should also mention that these distances are not calculated and are the typical values for the Galactic Center objects.

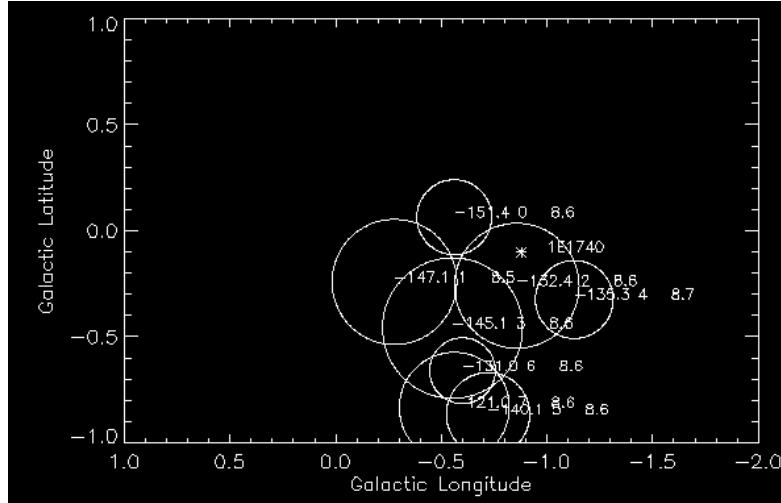


Figure 4.12 The position of molecular clouds in the Galactic Center and the relative position of 1E 1740.7–2742 (shown as a star in the graph) in the LOS.

Vilhu et al. (1997) calculated the expected hydrogen column density values depending on the relative position of the source to the cloud. They estimate that if the source is close to the center  $N_H$  should be around  $\sim 3.5 \times 10^{22} \text{cm}^{-2}$ . On the other hand, for high  $N_H$  values they conclude that the source is close to the edge of the cloud. Our results show that the  $N_H$  is about  $\sim 2 \times 10^{23} \text{cm}^{-2}$ . In the light of these constraints, we assume that the source is located in a dense molecular cloud and possibly positioned near the far end of the cloud in our LOS. Therefore, the contribution from the DSH should be intense.



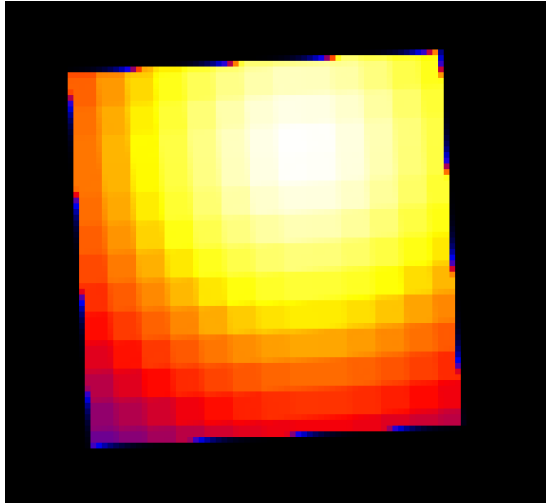


Figure 4.13 The exposure map of EPIC-PN in the 2.11 – 5.86 keV energy band.

## 4.6 The surface brightness profile of *XMM-Newton* EPIC-PN

The low rms amplitude of variability values obtained from RXTE and *XMM-Newton* gives the hints of the presence of a DSH. In order to confirm this we used the surface brightness profile method to see how much the emission extends radially. First, we created the exposure map (Figure 4.13) using the *exmap* procedure. Then, we have obtained the SBP (Fig. 4.14) following the steps described in section 3.2.1.2. The energy range we used is 2.11 – 5.86 keV.

Same figure shows the 1D point spread functions (PSF) with a *King* profile obtained through the XMM-SAS’s *eradial* procedure. It is normalized so that the counts in the central pixels match. Table 4.1 shows the how much of the photons come from the background and the DSH. If the source is in a molecular cloud, the PSF (blue line in Fig. 4.14) may be even lower. Since the scattering scales as  $\theta^{-2}$  PSF may be underestimated.

Total Photons	187.239
Total PSF	155.351
Background + DSH	31.888

Table 4.5 Photon Counts between 0” – 30” arcseconds.

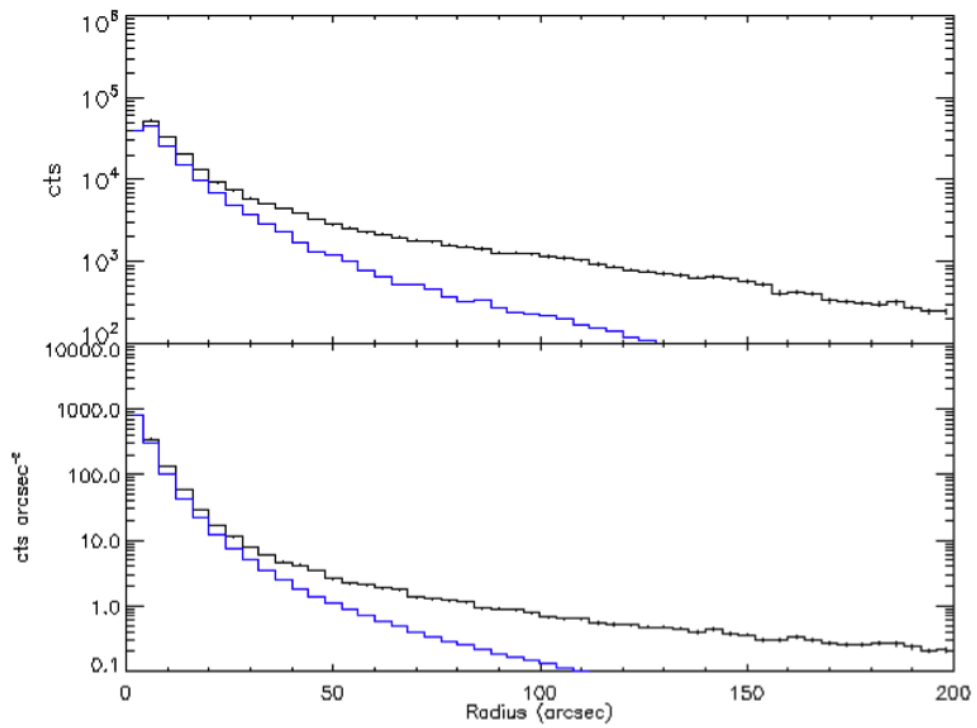


Figure 4.14 Unnormalized and normalized radial profiles of EPIC-PN in 2.11-5.86 keV energy band. Blue lines show the 1D PSF.

# Chapter 5

## Discussions and Conclusion

### 5.1 Quantifying the DSH contribution and improving the background correction

In order to explain the low rms amplitudes obtained from RXTE and *XMM-Newton* observations we decided to quantify background components. Since 1E 1740.7–2742 is very close to the GC, we identified the RXTE background components as the Galactic Ridge emission, DSH and background. This can be formulated as:

$$T_r = S_r + B + H_r + R \quad (5.1)$$

where  $T_r$  is the total RXTE spectral counts,  $S_r$  is the model predicted source counts, B is the modelled background from the *pcabackest*, R is the Ridge emission counts and  $H_r$  is the RXTE halo counts. For EPIC-PN spectrum:

$$T_x = S_x + B + H_x \quad (5.2)$$

where  $T_x$  is the total *XMM-Newton* EPIC-PN spectral counts,  $S_x$  is the modelled source counts, B is the background and  $H_x$  is the halo. We modelled the  $H_x$  as a fraction of the  $S_x$ ;  $H_x = C \times S_x$ , where C is a constant. If the components in the Eq 5.1 and 5.2 are quantified, then we can modify the correction method used in Berger and Van der Klis (1994) for the PSD powers and rms values and obtain the “intrinsic” values. They proposed a correction factor for the power spectrum powers that takes the background component into account. We improved this correction by including the Ridge and DSH components as:

$$f = \frac{T^2}{(T - (B + R + H))^2} \quad (5.3)$$

where  $T$  is the total photon rate,  $B$  is the background count rate,  $R$  is the Ridge Emission count rate and  $H$  is the DSH count rate. This correction factor is for  $(rms/mean)^2$  values. Then the correction for the rms amplitude of variability values is the square-root of this. According to this, we model the correction for RXTE rms amplitude of variability as:

$$f_r = \frac{T_r}{T_r - (B + R + H_r)} = \frac{T_r}{S_r} \quad (5.4)$$

and for the *XMM-Newton* as:

$$f_x = \frac{T_x}{T - (B + H_x)} \quad (5.5)$$

We mentioned that the observations towards the GC are heavily affected by Galactic diffuse Ridge emission (Ridge emission). The unresolved joint faint sources that have soft spectra make a contribution to the collected photons with the PCA instrument. This contribution cannot be modelled with standard background models. Ridge contribution is independent of the source therefore it reduces the observed  $(rms/mean)$  value. In order to determine the ridge contribution we used the archival *Rossi X-ray Timing Explorer* background observations (ObsID 40097-07-02-00) of 1E 1740.7–2742.

First, we fitted the Ridge spectrum with *power-law+gaussian* models and obtained the ridge counts from the 2-6 keV energy band. Ridge spectrum yields a Ridge count rate of  $19.72 \text{ cnt s}^{-1}$ . Then, using the offset source observation (91112-09-01-00), we obtained the total count rate of the source including all components while excluding the background in the 2-6 keV energy band. After that, we put the background back in and obtained the background rate. According to this the total count rate is found as  $55.73 \text{ cnt s}^{-1}$  and the background is  $10.43 \text{ cnt s}^{-1}$ .

Next step is to obtain the fit parameters from the PN observation in the energy band 2.11-5.86 keV. The best fit parameters are  $\Gamma = 1.53_{-0.05}^{+0.05}$ ,  $N_H = 18.88_{-0.38}^{+0.39}$  and a normalization of 0.08 with a reduced  $\chi^2$  of 1.1. Now, we need to carry these results to the offset RXTE spectrum to obtain the final counts for each component, namely  $S_r$  in the Eq 5.1 and Eq 5.4.

We model the offset RXTE observation using the PN model mentioned above and using the same parameters yields a model predicted rate of  $15.21 \text{ cnt s}^{-1}$ . This count rate corresponds to the  $S_r$  component.

Since the RXTE observation was offset we need a correction factor to cope for the offsetting effects as well as different effective areas of the instruments. To obtain this factor, we compared the predicted count rates using the model we used to fit the PN spectrum in 2.11 – 5.86 keV. According to this, a "conversion factor" of 1.56 (9.71 counts from PN and 15.21 counts from RXTE) is found. This means that each photon in the PN spectrum cor-

responds to 1.56 photons in the RXTE spectrum. We will call this value “ $f_c$ ” and will use it to compare the source counts of the PN observation to the RXTE spectrum.

Since the two observations are simultaneous, their intrinsic power spectra and rms amplitude of variabilities should match when corrected. The “corrected” rms amplitude of variabilities using the correction factors can be written as:

$$(RXTE\ RMS) \times \frac{T_r}{S_r} = (PN\ RMS) \times \frac{T_x}{T_x - H_x} \quad (5.6)$$

where RXTE rms amplitude of variability is  $\sim 10\%$ ,  $T_r$  is 55.73,  $S_r$  is 15.21, PN rms amplitude of variability is  $\sim 16\%$  and PN background is negligible. Assuming the carried PN spectrum does not contain DSH therefore  $S_r$  is pure source counts (15.21  $cnt\ s^{-1}$  as predicted by the model), the corrected rms values should match at 36.6%, which is an expected value from a GBH source in the hard state. However, this limit, in turn implies that the PN spectrum actually contains DSH. Further corrections of DSH in both sides of Eq. 5.6 increases the correction factor to higher rms amplitude percentages which is not within the observed limits. We conclude that 36.6% of rms amplitude puts a lower limit to the “intrinsic” rms amplitude of variability for our source.

Low quality of the PSDs introduced high errors, consequently it might lead us to overestimate the RXTE rms amplitude while underestimating the PN rms amplitude of variability as it can be seen from the results in section 4.4. There are other factors to be considered, such as: the mismatch of the RXTE and EPIC-PN spectral responses, cross calibration of RXTE and EPIC-PN, simplistic correction factor, etc.

## 5.2 Conclusion and Future Work

Our view towards sources that are in the Galactic plane is often limited due to the absorption and scattering of the electromagnetic radiation by the interstellar medium. The X-ray photons are rather scattered than absorbed, favorably in the forward direction. Accordingly, the X-ray sources that have high absorption column density (or hydrogen column density) often show dust scattering halos of diffuse X-ray emission. This thesis illuminates the effects of the small angle scattering of the X-ray photons by dust grains in molecular clouds on temporal properties of Galactic black hole sources. We investigated how the differential delays caused by the scattering process exhibit an influence on the observed Fourier powers and rms amplitude of variability (rms/mean).

We analyzed the simultaneous observations of 1E 1740.7–2742 with *XMM-Newton* and *RXTE* for  $\sim 20$  ks. We chose this source since it has very high hydrogen column density ( $\sim 10^{23} \text{ cm}^{-2}$ ) and has a persistent emission that is usually hard, spectrally. We obtained the energy spectra from both instruments and also used an earlier *Chandra* observation by Gallo & Fender (2002) for spectral analysis. *XMM-Newton* and *RXTE* energy spectra showed that the source is in the hard state. The *Chandra* spectrum was fixed to the same hydrogen column density obtained from the EPIC-PN detector of *XMM-Newton*. Its spectrum shows that, it has a rather softer spectral index than that of our observations. To shine a light on these results and our interpretation of them, we created a source history of brightness using the archival *RXTE* observations of the source. The brightness history of our observations showed that the source does not show any dramatic changes in its flux. *Chandra* history pictured a slightly higher brightness that is decreasing.

A connection to a molecular cloud could also explain the very high hydrogen column densities observed in the spectral modelling. Using the catalog of *HCO*<sup>+</sup> clouds in the Galactic Center, we showed that there is a molecular cloud in the line of sight of the source. We think that the source is in this molecular cloud, towards the far edge of it, considering the hydrogen column density values we obtained (Vilhu et al. 1997).

We evaluated the extended radial emission up to 200 arcseconds from the source. The surface brightness profile we created revealed the presence of excess emission extending up to 100 arcseconds. This proves that the source produces a dust scattering halo.

To understand how the dust scattering halo effects the intrinsic variability of the signal, we employed Fourier techniques (PSD, squared fractional rms variability). We interpreted our findings in the context of observational timing properties of galactic black hole transients in the hard state. We obtained the Miyamoto normalized power spectra from the *RXTE* and *XMM-Newton* light curves. We fitted these spectra with Lorentzians and calculated the

rms amplitude of variability and peak frequencies. The determined values display very low variability compared to the typical values for GBHTs in their hard state. We attribute this phenomena to the loss of coherence of the signal arising from the scattering process.

We tackled this problem by empirically correcting the observed variabilities. We modified the correction method used by Berger and Van der Klis (1994) that corrects the power spectra values for the background noise. We identified the possible sources of white noise in the signal and modelled them using spectral means. Then, we obtained the correction factors for rms amplitude of variability and powers as shown in the sections 5.1 and 5.2. While these corrections restored the observed rms amplitude of variability to the expected levels, the high errors of the initial variability results prevented a robust interpretation and comparison of the corrected results. We might have overestimated the RXTE variability while underestimated the *XMM-Newton* variabilities within  $2\sigma$ . Another reason for the low quality of the PSDs is the difference of effective areas of two instruments at low energy part of the energy band we used in our analysis. The RXTE effective area is very steep in the 2.11 – 5 keV band while EPIC-PN is flat in this band. We plan to improve our empirical correction method by taking into account the effects of effective areas and cross calibration methods for the two instrument.

Finally, the investigations on the problem of observed low rms amplitude of variabilities due to the scattering of X-rays and it's implications on the temporal properties by Kalemci (2002) and Kalemci et al. (2006) are reanalyzed and improved. Our results present the necessity of dealing with this type of white noise which can effect a wide range of studies in the GBHT field. Moreover, the next generation instruments those will be launched in the next decade, such as eXTP and STROBE-X, will be more affected by the dust scattering halos due to their increased temporal sensitivity and spectral resolution and wide FOVs. That is why, we need a solid understanding of the effects of DSHs both spectrally and temporally. We plan to propose new observations of similar sources with the ASTROSAT's LAXPC in addition to the instruments we used in this analysis to further investigate this phenomenon with better quality observations taking the cross calibration effects into account.

# Bibliography

- Arnaud, K. (1996). XSPEC: The First Ten Years. *Astronomical Data Analysis Software and Systems V, A.S.P. Conference Series*, 5:17.
- Arnaud, K. (2019). Cospar 2019 Capacity Building Workshop, IISER, Mohali, India.
- Audley, M. D., Nagase, F., Mitsuda, K., Angelini, L., and Kelley, R. L. (2006). ASCA observations of OAO 1657-415 and its dust-scattered X-ray halo. *Monthly Notices of the Royal Astronomical Society*, 367(3):1147–1154.
- Balbus, S. A. and Hawley, J. F. (1991). A powerful local shear instability in weakly magnetized disks. I - Linear analysis. II - Nonlinear evolution. *The Astrophysical Journal*, 376(Ii):214.
- Bally, J. and Leventhal, M. (1991). Is the Galactic Centre gamma-ray source 1E1740.7 – 2942 accreting from a molecular cloud? *Nature*, 353(6341):234–237.
- Belloni, T., Psaltis, D., and van der Klis, M. (2002). A Unified Description of the Timing Features of Accreting X-Ray Binaries. *The Astrophysical Journal*, 572(1):392–406.
- Belloni, T. M. (2009). States and transitions in black hole binaries. *Lecture Notes in Physics*, 794:53–84.
- Beloborodov, A. (1999). Accretion Disk Models. *High Energy Processes in Accreting Black Holes, ASP Conference Series 161, ed. Juri Poutanen & Roland Svensson*, 161.
- Berger, M. and Van der Klis, M. (1994). High time resolution observations of Cygnus X-3 with EXOSAT. *Astronomy & Astrophysics*, 292:175–182.
- Bisnovatyi-Kogan, G. and Blinnikov, S. (1977). Disk accretion onto a black hole at subcritical luminosity. *Astronomy and*, 59:111–125.
- Blandford, R. D. and Begelman, M. C. (1999). On the fate of gas accreting at a low rate on to a black hole. *Monthly Notices of the Royal Astronomical Society*, 303(1):1–5.



- Bouchet, L., Santo, M. D., Jourdain, E., Roques, J. P., Bazzano, A., and De Cesare, G. (2009). UNVEILING THE HIGH ENERGY TAIL OF 1E 1740.7-2942 WITH INTEGRAL. *The Astrophysical Journal*, 693(2):1871–1876.
- Buxton, M. M., Bailyn, C. D., Capelo, H. L., Chatterjee, R., Dinçer, T., Kalemci, E., and Tomsick, J. A. (2012). Optical and near-infrared monitoring of the black hole X-ray binary GX 339-4 during 2002-2010. *Astronomical Journal*, 143(6).
- Cannizzo, J. K., Wheeler, J. C., and Ghosh, P. (1985). Accretion Instability Models for Dwarf Novae and X-Ray Transients. pages 307–313.
- Capitanio, F., Belloni, T., Del Santo, M., and Ubertini, P. (2010). A failed outburst of H1743-322. *AIP Conference Proceedings*, 1248(October):149–150.
- Casares, J., Jonker, P. G., and Israelian, G. (2017). X-Ray Binaries. In *Handbook of Supernovae*, volume 1, pages 1499–1526. Springer International Publishing, Cham.
- Chakrabarti, S. K. (2000). Advective Accretion Flows: Ten Years Later. pages 1–18.
- Corbel, S., Coriat, M., Brocksopp, C., Tzioumis, A. K., Fender, R. P., Tomsick, J. A., Buxton, M. M., and Bailyn, C. D. (2013). The 'universal' radio/X-ray flux correlation: The case study of the black hole GX 339-4. *Monthly Notices of the Royal Astronomical Society*, 428(3):2500–2515.
- Corbel, S., Fender, R. P., Tomsick, J. A., Tzioumis, A. K., and Tingay, S. (2004). On the Origin of Radio Emission in the X-Ray States of XTE J1650500 during the 2001–2002 Outburst. *The Astrophysical Journal*, 617(2):1272–1283.
- Corbel, S., Fender, R. P., Tzioumis, A. K., Nowak, M., McIntyre, V., Durouchoux, P., and Sood, R. (2000). Coupling of the X-ray and radio emission in the black hole candidate and compact jet source GX 339-4. 268(2000):251–268.
- Corbel, S., Nowak, M. A., Fender, R. P., Tzioumis, A. K., and Markoff, S. (2003). Radio / X-ray correlation in the low/hard state of GX 339-4. 1012:1007–1012.
- Coriat, M., Corbel, S., Buxton, M. M., Bailyn, C. D., Tomsick, J. A., Körding, E., and Kalemci, E. (2009). The infrared/X-ray correlation of GX 339-4: Probing hard X-ray emission in accreting black holes. *Monthly Notices of the Royal Astronomical Society*, 400(1):123–133.

- Coriat, M., Corbel, S., Prat, L., Miller-Jones, J. C. A., Cseh, D., Tzioumis, A. K., Brocksopp, C., Rodriguez, J., Fender, R. P., and Sivakoff, G. R. (2010). Accretion-outflow connection in the outliers of the “universal” radio/X-ray correlation. *Proceedings of the International Astronomical Union*, 6(S275):255–259.
- Corrales, L. R., García, J., Wilms, J., and Baganoff, F. (2016). The dust-scattering component of X-ray extinction: Effects on continuum fitting and high-resolution absorption edge structure. *Monthly Notices of the Royal Astronomical Society*, 458(2):1345–1351.
- Corrales, L. R. and Paerels, F. (2015). The dust scattering halo of Cygnus X-3. *Monthly Notices of the Royal Astronomical Society*, 453(1):1121–1135.
- Costantini, E., Freyberg, M. J., and Predehl, P. (2005). Absorption and scattering by interstellar dust: an XMM-Newton observation of Cyg X-2. *Astronomy & Astrophysics*, 444(1):187–200.
- Cui, W., Schulz, N. S., Baganoff, F. K., Bautz, M. W., Doty, J. P., Garmire, G. P., Mirabel, I. F., Ricker, G. R., Rodríguez, L. F., and Taylor, S. C. (2001). Peculiar Extended X-Ray Emission around the “Radio-loud” Black Hole Candidate 1E 1740.72942. *The Astrophysical Journal*, 548(1):394–400.
- Del Santo, M., Belloni, T. M., Tomsick, J. A., Sbarufatti, B., Cadolle Bel, M., Casella, P., Castro-Tirado, A., Corbel, S., Grinberg, V., Homan, J., Kalemci, E., Motta, S., Muñoz-Darias, T., Pottschmidt, K., Rodriguez, J., and Wilms, J. (2016). Spectral and timing evolution of the bright failed outburst of the transient black hole Swift J174510.8-262411. *Monthly Notices of the Royal Astronomical Society*, 456(4):3585–3595.
- Dinger, T., Kalemci, E., Buxton, M. M., Bailyn, C. D., Tomsick, J. A., and Corbel, S. (2012). X-ray, optical, and infrared observations of GX 339-4 during its 2011 decay. *Astrophysical Journal*, 753(1).
- Done, C. and Nayakshin, S. (2001). Observational Signatures of X-Ray-irradiated Accretion Disks. *The Astrophysical Journal*, 546(1):419–428.
- Draine, B. T. (2003). Scattering by Interstellar Dust Grains. II. X-Rays. *The Astrophysical Journal*, 598(2):1026–1037.
- Esin, A. A., McClintock, J. E., Drake, J. J., Garcia, M. R., Haswell, C. A., Hynes, R. I., and Muno, M. P. (2001). Modeling the Low-State Spectrum of the X-Ray Nova XTE J1118+480. *The Astrophysical Journal*, 555(1):483–488.

- Esin, A. A., McClintock, J. E., and Narayan, R. (1997). Advection-Dominated Accretion and the Spectral States of Black Hole X-Ray Binaries: Application to Nova Muscae 1991. *10:865–889*.
- Fabian, A. C. and Ross, R. R. (2010). X-ray reflection. *Space Science Reviews*, 157(1-4):167–176.
- Fender, R., Belloni, T., and Gallo, E. (2005). A unified model for black hole X-ray binary jets? In *Astrophysics and Space Science*, pages 1–13. Springer Netherlands, Dordrecht.
- Fender, R. P. (1999). Black hole states and radio jet formation. (1973).
- Fender, R. P. (2001). Powerful jets from black hole X-ray binaries in low/hard X-ray states. *Monthly Notices of the Royal Astronomical Society*, 322(1):31–42.
- Fender, R. P., Belloni, T. M., and Gallo, E. (2004). Towards a unified model for black hole X-ray binary jets. *Monthly Notices of the Royal Astronomical Society*, 355(4):1105–1118.
- Frank, J., King, A. R., and Raine, D. (1992). *Frank, King, Raine - Accretion Power in Astrophysics.pdf*. Cambridge University Press.
- Gallo, E., Fender, R. P., and Pooley, G. G. (2003). A universal radio-X-ray correlation in low/hard state black hole binaries. *Monthly Notices of the Royal Astronomical Society*, 344(1):60–72.
- Gallo, E., Miller, B. P., and Fender, R. (2012). Assessing luminosity correlations via cluster analysis: Evidence for dual tracks in the radio/X-ray domain of black hole X-ray binaries. *Monthly Notices of the Royal Astronomical Society*, 423(1):590–599.
- Gierliński, M., Maciołek-Niedźwiecki, A., and Ebisawa, K. (2001). Application of a relativistic accretion disc model to X-ray spectra of LMC X-1 and GRO J1655-40. *Monthly Notices of the Royal Astronomical Society*, 325(3):1253–1265.
- Gilfanov, M. (2009). X-ray emission from black-hole binaries. *Lecture Notes in Physics*, 794:17–51.
- Güver, T. and Özel, F. (2009). The relation between optical extinction and hydrogen column density in the Galaxy. *Monthly Notices of the Royal Astronomical Society*, 400(4):2050–2053.
- Hameury, J.-M., King, A. R., and Lasota, J.-P. (1990). Black hole X-ray transients. *The Astrophysical Journal*, 353(1987):585.

- Hawley, J. F. and Balbus, S. A. (1991). A Powerful Local Shear Instability in Weakly Magnetized Disks. II. Nonlinear Evolution. *The Astrophysical Journal*, 376:223.
- Hertz, P. and Grindlay, J. E. (1985). The optical structure of X-ray globular clusters. *The Astrophysical Journal*, 298(September):95.
- Homan, J., Buxton, M., Markoff, S., Bailyn, C. D., Nespoli, E., and Belloni, T. (2005). Multi-wavelength observations of the 2002 outburst of GX 339-4: two patterns of X-ray-optical/near-infrared behavior. (1):295–306.
- Hua, X.-M. and Titarchuk, L. (1995). Comptonization Models and Spectroscopy of X-Ray and Gamma-Ray Sources: A Combined Study by Monte Carlo and Analytical Methods. *The Astrophysical Journal*, 449(September):188.
- Ichimaru, S. (1977). Bimodal behavior of accretion disks - Theory and application to Cygnus X-1 transitions. *The Astrophysical Journal*, 214:840.
- Jahoda, K., Swank, J. H., Giles, A. B., Stark, M. J., Strohmayer, T., Zhang, W. W., and Morgan, E. H. (1996). <title>In-orbit performance and calibration of the Rossi X-ray Timing Explorer (RXTE) Proportional Counter Array (PCA)</title>. volume 2808, pages 59–70.
- Jin, C., Ponti, G., Haberl, F., Smith, R., and Valencic, L. (2018). Effects of interstellar dust scattering on the X-ray eclipses of the LMXB AX J1745.6-2901 in the Galactic Centre. *Monthly Notices of the Royal Astronomical Society*, 477(3):3480–3506.
- Kalemci, E. (2002). *Temporal Studies of Black Hole X-ray Transients During Outburst Decay*. PhD thesis.
- Kalemci, E., Maccarone, T. J., and Tomsick, J. A. (2018). Dust scattering halo of 4U 1630-47 observed with Chandra and Swift: New constraints on the source distance. pages 1–13.
- Kalemci, E., Tomsick, J. A., Buxton, M. M., Rothschild, R. E., Pottschmidt, K., Corbel, S., Brocksopp, C., and Kaaret, P. (2005a). Multiwavelength Observations of the Galactic Black Hole Transient 4U 154347 during Outburst Decay: State Transitions and Jet Contribution. *The Astrophysical Journal*, 622(1):508–519.
- Kalemci, E., Tomsick, J. A., Buxton, M. M., Rothschild, R. E., Pottschmidt, K., Corbel, S., Brocksopp, C., and Kaaret, P. (2005b). Multiwavelength Observations of the Galactic Black Hole Transient 4U 154347 during Outburst Decay: State Transitions and Jet Contribution. *The Astrophysical Journal*, 622(1):508–519.

- Kalemci, E., Tomsick, J. A., Rothschild, R. E., Pottschmidt, K., Corbel, S., Wijnands, R., Miller, J. M., and Kaaret, P. (2003). X-Ray Temporal Properties of XTE J1650500 during Outburst Decay. *The Astrophysical Journal*, 586(1):419–426.
- Kalemci, E., Tomsick, J. A., Rothschild, R. E., and Smith, D. (2006). The effect of dust scattering on the timing properties of black holes. In *Proceedings of VI Microquasar Workshop: Microquasars and Beyond — PoS(MQW6)*, page 080, Trieste, Italy. Sissa Medialab.
- Knoll, G. (1979). *Radiation Detection and Measurement*.
- Kuznetsov, S., Gilfanov, M., Churazov, E., Sunyaev, R., Korel, I., Khavenson, N., Dyachkov, A., Chulkov, I., Ballet, J., Laurent, P., Vargas, M., Goldwurm, A., Roques, J. P., Jourdain, E., Bouchet, L., and Borrel, V. (1997). Properties Of The Hard X-ray Radiation From The Black Hole Candidates: Cygnus X-1 And 1E1740.7-2942. 6(March):1–6.
- Leahy, D. A., Langill, P., and Kwok, S. (1992). High resolution I-band imaging of the 1E 1740.7-2942 region. *Astronomy And Astrophysics*, 259:209–210.
- Leahy, D. A., D. W. E. R. F. W. M. C. S. P. G. K. S. (1983). On searches for pulsed emission with application to four globular cluster X-ray sources. *Astrophysical Journal*, pages 160–170.
- Liang, E. P. T. and Price, R. H. (1977). Accretion disk coronae and Cygnus X-1. *The Astrophysical Journal*, 218:247.
- Lin, D., Smith, I. A., Liang, E. P., and Böttcher, M. (2000). Complex Phase Lag Behaviors of the 0.5–10 H[CLC]z[/CLC] Quasi-periodic Oscillations in GRS 1915+105. *The Astrophysical Journal*, 543(2):L141–L144.
- Lin, D. N. C. and Taam, R. E. (1984). On the structure, stability and evolution of accretion disks in soft x-ray transient sources. In *AIP Conference Proceedings*, volume 115, pages 83–102. AIP.
- Ling, Z., Zhang, S. N., and Tang, S. (2009). Determining the distance of cyg x-3 with its x-ray dust scattering halo. *Astrophysical Journal*, 695(2):1111–1120.
- MAIN, D. S., Smith, M. D., Heindl, W. A., Swank, J., and Leventhal, M. (1999). Long-Term X-Ray Monitoring of 1E 1740.7-2942 and Grs 1758-258. *The Astronomical Journal*, 525:901.
- Malzac, J. (2003). Time dependent Comptonisation. 742:742–745.

- Martí, J., Luque-Escamilla, P. L., Sánchez-Sutil, J. R., Muñoz-Arjonilla, A. J., Sánchez-Ayaso, E., Combi, J. A., and García-Hernández, M. T. (2010). An apparently extended infrared counterpart to 1E 1740.7-2942. *Astrophysical Journal Letters*, 721(2 PART 2):126–128.
- Mathis, J. S., Lee, C., Observatory, W., and Street, N. C. (1991). No Title. (1981):490–499.
- McClintock, J. E., Narayan, R., and Rybicki, G. B. (2004). On the Lack of Thermal Emission from the Quiescent Black Hole XTE J1118+480: Evidence for the Event Horizon. *The Astrophysical Journal*, 615(1):402–415.
- Merloni, A. (2002). Microquasars in the low/hard state: strong coronae, compact jets, and the high frequency variability. pages 1–4.
- Merloni, A., Fabian, A. C., and Ross, R. R. (2000). On the interpretation of the multicolour disc model for black hole candidates. *Monthly Notices of the Royal Astronomical Society*, 313(1):193–197.
- Meyer, F., Liu, B. F., and Meyer-Hofmeister, E. (2000). Black hole X-ray binaries: A new view on soft-hard spectral transitions. 70:67–70.
- Mineshige, S. and Wheeler, J. C. (1989). Disk-instability model for soft-X-ray transients containing black holes. *The Astrophysical Journal*, 343:241.
- Mirabel, I. F., Morris, M., Wink, J., Paul, J., and Cordier, B. (1991). 1E 1740.7-2942 : a black hole in a molecular cloud? *Astronomy And Astrophysics*, 25(L):43.
- Mirabel, I. F., Rodríguez, L. F., Cordier, B., Paul, J., and Lebrun, F. (1992). A double-sided radio jet from the compact Galactic Centre annihilator 1E1740.7–2942. *Nature*, 358(6383):215–217.
- Mitsuda, K. (1984). Energy Spectra of Low-Mass Binary X-ray Sources Observed from Tenma. *Ph.D. thesis, Univ. Tokyo*.
- Miyamoto, S. and Kitamoto, S. (1989). X-ray time variations from Cygnus X-1 and implications for the accretion process. *Nature*, 342(6251):773–774.
- Molnar, L. A. and Mauche, C. W. (1986). Effects of the X-ray scattering halo on the observational properties of Cygnus X-3. *The Astrophysical Journal*, 310:343.
- Narayan, R., Mahadevan, R., and Quataert, E. (1998). Advection-Dominated Accretion around Black Holes. (1988):1–36.

- Narayan, R. and Yi, I. (1995). Advection-dominated Accretion: Underfed Black Holes and Neutron Stars. *The Astrophysical Journal*, 452:710.
- Nowak, M. (2005). X-RAY and Radio Monitoring of GX 339-4 and CYG X-1. *Astrophysics and Space Science*, 300(1-3):159–166.
- Nowak, M. A., Wilms, R. N., and Dove, J. B. (1999). THE ASTROPHYSICAL JOURNAL, 517 : 355–366, 1999 May 20 ( 1999. 20.
- Osaki, Y. (1985). Irradiation-induced mass-overflow instability as a possible cause of super-outbursts in SU UMa stars. *Astronomy & Astrophysics*, 144:369–380.
- Overbeck, J. W. (1965). Small-Angle Scattering of Celestial X-Rays by Interstellar Grains. *The Astrophysical Journal*, 141:864.
- Plotkin, R. M., Gallo, E., and Jonker, P. G. (2013). The X-ray spectral evolution of galactic black hole X-ray binaries toward quiescence. *Astrophysical Journal*, 773(1).
- Pottschmidt, K., Wilms, J., Nowak, M. A., Pooley, G. G., Gleissner, T., Heindl, W. A., Smith, D. M., Remillard, R., and Staubert, R. (2003). Long term variability of Cygnus X-1. *Astronomy & Astrophysics*, 407(3):1039–1058.
- Predehl, P. and Schmitt, J. (1995). X-raying the interstellar medium: ROSAT observations of dust scattering halos. *Astronomy And Astrophysics*, (293):889–905.
- Psaltis, D. (2001). Compton Scattering in Static and Moving Media. II. System-Frame Solutions for Spherically Symmetric Flows. *The Astrophysical Journal*, 555(2):786–800.
- Ratti, E. M., Jonker, P. G., Miller-Jones, J. C., Torres, M. A., Homan, J., Markoff, S., Tomsick, J. A., Kaaret, P., Wijnands, R., Gallo, E., Özel, F., Steeghs, D. T., and Fender, R. P. (2012). The black hole candidate XTE J1752-223 towards and in quiescence: Optical and simultaneous X-ray-radio observations. *Monthly Notices of the Royal Astronomical Society*, 423(3):2656–2667.
- Rodriguez, J., Bel, M. C., Tomsick, J. A., Corbel, S., Brocksopp, C., Paizis, A., Shaw, S. E., and Bodaghee, A. (2007). The Discovery Outburst of the X-Ray Transient IGR J17497-2821 Observed with RXTE and ATCA. *The Astrophysical Journal*, 655(2):L97–L100.
- Rolf, D. P. (1983). Evidence for the detection of X-ray scattering from interstellar dust grains. *Nature*, 302(5903):46–48.

- Russell, D. M., Fender, R. P., Hynes, R. I., Brocksopp, C., Homan, J., Jonker, P. G., and Buxton, M. M. (2006). Global optical/infrared-X-ray correlations in X-ray binaries: Quantifying disc and jet contributions. *Monthly Notices of the Royal Astronomical Society*, 371(3):1334–1350.
- Russell, D. M., Maitra, D., Dunn, R. J. H., and Markoff, S. (2010). Evidence for a compact jet dominating the broad-band spectrum of the black hole accretor XTE J1550-564. *Monthly Notices of the Royal Astronomical Society*, 405(3):no–no.
- Rybicki, A. and Lightman, P. (1979). *RADIATIVE PROCESSES IN ASTROPHYSICS*.
- Shakura, N. and Sunyaev, R. (1973). Black Holes in Binary Systems: Observational Appearances. *A&A*, 24:337.
- Shapiro, S. L. and Teukolsky, S. A. (1983). *Black Holes, White Dwarfs, and Neutron Stars*. Wiley.
- Smith, D., Heindl, W., and Swank, J. (2002). Two Different Long-Term Behaviors in Black Hole Candidates: Evidence for Two Accretion Flows? *The Astrophysical Journal*, 569(1):362–380.
- Smith, D. M., Heindl, W. A., Swank, J., Leventhal, M., Mirabel, I. F., and Rodriguez, L. F. (1997). X-Ray Timing in 1E 1740.72942 and GRS 1758258. *The Astrophysical Journal*, 489(1):L51–L54.
- Stirling, A. M., Spencer, R. E., and Garrett, M. A. (1997). Radio jets in Cygnus X-1?
- Sunyaev, R., Churazov, E., Gilfanov, M., Pavlinsky, M., Grebenev, S., Babalyan, G., and Dekhanov, I. (1991a). Two Hard X-ray sources near the Galactic center: The known source 1E1740.7-2942 and the newly discovered source GRS 1758-258. *SvAL*, 3(September).
- Sunyaev, R., Churazov, E., Gilfanov, M., Pavlinsky, M., Grebenev, S., Babalyan, G., Dekhanov, I., Khavenson, N., Bouchet, L., Mandrou, P., Roques, J. P., Vedrenne, G., Cordier, B., Goldwurm, A., Lebrun, F., and Paul, J. (1991b). Three spectral states of 1E 1740.7 - 2942 - From standard Cygnus X-1 type spectrum to the evidence of electron-positron annihilation feature. *The Astrophysical Journal*, 383:L49.
- Sunyaev, R. and Revnivtsev, M. (2000). Fourier power spectra at high frequencies: a way to distinguish a neutron star from a black hole. 623:617–623.
- Sunyaev, R. and Titarchuk, L. (1980). Comptonization of X-rays in plasma clouds. Typical radiation spectra. *Astronomy & Astrophysics*, 86:121–138.



- Sunyaev, R. and Trümper, J. (1979). Hard X-ray spectrum of Cyg X-1. *Nature*, 279(5713):506–508.
- Tanaka, Y. and Lewin, W. (1995). *X-ray Binaries*.
- Tanaka, Y. and Shibazaki, N. (1996). X-RAY NOVAE. *Annu. Rev. Astron. Astrophys*, 34(607):44.
- Tiengo, A., Vianello, G., Esposito, P., Mereghetti, S., Giuliani, A., Costantini, E., Israel, G. L., Stella, L., Turolla, R., Zane, S., Rea, N., Götz, D., Bernardini, F., Moretti, A., Romano, P., Ehle, M., and Gehrels, N. (2010). The dust-scattering X-ray rings of the anomalous X-ray pulsar 1e1547.0-5408. *Astrophysical Journal*, 710(1):227–235.
- Tomsick, J. A. and Kaaret, P. (2000). X-Ray Spectral and Timing Evolution during the Decay of the 1998 Outburst from the Recurrent X-Ray Transient 4U 163047. *The Astrophysical Journal*, 537(1):448–460.
- Toor, A., Palmieri, T. M., and Seward, F. D. (1976). Evidence for 'thermal' X-rays from the Crab Nebula. *The Astrophysical Journal*, 207(2):96.
- Trümper, J. and Schönfelder, V. (1973). Distance Determination of Variable X-ray Sources. *Astronomy & Astrophysics*, 23:445.
- van der Klis, M. (1989). Timing in X-ray astronomy. *Timing Neutron Stars: proceedings of the NATO Advanced Study Institute on Timing Neutron Stars held April 4-15, 1988, in Çeşme, Izmir, Turkey. Edited by H. Ögelman and E. P. J. van den Heuvel. ISBN: 0-7923-0101-3. Published by Kluwer Academic.*
- van der Klis, M. (1995). Rapid Variability in X-ray Binaries - Toward a Unified Description. *The Lives of the Neutron Stars. Proceedings of the NATO Advanced Study Institute on the Lives of the Neutron Stars*, page 301.
- van Straaten, S., van der Klis, M., di Salvo, T., and Belloni, T. (2002). A Multi-Lorentzian Timing Study of the Atoll Sources 4U 0614+09 and 4U 172834. *The Astrophysical Journal*, 568(2):912–930.
- Verner, D. A., Ferland, G. J., Korista, K. T., and Yakovlev, D. G. (1996). Atomic Data for Astrophysics. II. New Analytic FITS for Photoionization Cross Sections of Atoms and Ions. *The Astrophysical Journal*, 465:487.

- Vilhu, O., Nevalainen, J., Poutanen, J., Gilfanov, M., Durouchoux, P., Vargas, M., Narayan, R., and Esin, A. (1997). Two-phase spectral modelling of 1E1740.7-2942. In *AIP Conference Proceedings*, pages 887–891. AIP.
- Wilms, J. (1998). X-Rays From Galactic Black Holes.
- Wilms, J., Allen, A., and McCray, R. (2000). On the Absorption of X-Rays in the Interstellar Medium. *The Astrophysical Journal*, 542(2):914–924.
- Wilms, J., Dove, J. B., Staubert, R., and Begelman, M. C. (1997). Properties of Accretion Disk Coronae. *The Transparent Universe, Proceedings of the 2nd INTEGRAL Workshop held 16-20 September 1996, St. Malo, France. Edited by C. Winkler, T. J.-L. Courvoisier, and Ph. Durouchoux, European Space Agency*, page 233.
- Xiang, J., Lee, J. C., and Nowak, M. A. (2007). Using the X-Ray Dust Scattering Halo of 4U 1624490 to Determine Distance and Dust Distributions. *The Astrophysical Journal*, 660(2):1309–1318.
- Xiang, J., Lee, J. C., and Nowak, M. A. (2011). USING THE X-RAY DUST SCATTERING HALO OF CYGNUS X-1 TO DETERMINE Radius ( arcsec ). 78.
- Zdziarski, A. A. (1998). Hot accretion discs with thermal Comptonization and advection in luminous black hole sources. *Monthly Notices of the Royal Astronomical Society*, 296(4).
- Zhu, H., Tian, W., Li, A., and Zhang, M. (2017). The gas-to-extinction ratio and the gas distribution in the Galaxy. *Monthly Notices of the Royal Astronomical Society*, 471(3):3494–3528.